THE CLIMATOLOGICAL CHARACTERISTICS AND INLAND PENETRATION OF ATMOSPHERIC RIVERS OVER THE WESTERN UNITED STATES

by

Jonathan James Rutz

A dissertation submitted to the faculty of
The University of Utah
in partial fulfillment of the requirements for the degree of

Doctor of Philosophy

Department of Atmospheric Sciences

The University of Utah

May 2014

The University of Utah Graduate School

STATEMENT OF DISSERTATION APPROVAL

The dissertation of **Jonathan James Rutz**

has been approved by the following supervisory committee members:

W. James Steenburgh	, Chair	**01-27-2014** Date Approved
John D. Horel	, Member	**01-27-2014** Date Approved
Courtenay Strong	, Member	**01-27-2014** Date Approved
Jan Paegle	, Member	**01-27-2014** Date Approved
F. Martin Ralph	, Member	**01-27-2014** Date Approved

and by **Kevin D. Perry** , Chair/Dean of

the Department/College/School of **Atmospheric Sciences**

and by David B. Kieda, Dean of The Graduate School.

ABSTRACT

This dissertation quantifies the climatological characteristics of cool-season (November–April) atmospheric rivers (ARs) over the western U.S., and identifies favorable conditions for the inland penetration of ARs approaching the U.S. west coast.

To quantify the climatological characteristics of cool-season ARs, they are objectively identified in the ERA-Interim reanalysis dataset on the basis of vertically integrated water vapor transport from November 1988 to April 2011. The climatological characteristics of ARs are generally largest along the coasts of Oregon and Washington, decreasing gradually southward along the coast, and rapidly eastward across the Sierra-Cascades Ranges. Over the interior, these characteristics are largest over the southwest and northwest, whereas they are smallest over the central and southern Great Basin, which lies downstream of the southern or "high" Sierra Nevada. The climatological characteristics of ARs over the western U.S. are strongly influenced by the climatology of landfalling ARs along the west coast and by water vapor depletion, particularly over high topographic barriers.

Data from 72-h forward trajectories initiated from 950 hPa within ARs near the North American west coast are used to identify conditions that are favorable for AR penetration into the interior. These trajectories are classified as coastal-decaying, inland-penetrating, or interior-penetrating based on whether they remain within an AR upon reaching selected transects over the western U.S. Conditions associated with

interior-penetrating AR trajectories include a more amplified atmospheric pattern, stronger southwesterly flow, and larger amounts of water vapor transport. Interior-penetrating AR trajectories most frequently originate along the Oregon coast, but trajectories originating along the coast of the Baja Peninsula are most likely to eventually penetrate into the interior. Although coastal-decaying and interior-penetrating AR trajectories experience similar decreases in specific humidity, the latter experience offsetting increases in wind speed that allow them to maintain large water vapor fluxes. Interior-penetrating AR trajectories lose a smaller fraction of their initial water vapor because they have more to begin with. Hence, synoptic conditions favoring larger initial water vapor flux and allowing for increases in wind over the western U.S. appear to play an important role in the maintenance of ARs as they penetrate into this region.

TABLE OF CONTENTS

ACKNOWLEDGEMENTS

First and foremost, I thank my academic advisor, Jim Steenburgh, for excellent guidance throughout this phase of my career. I also thank Drs. John Horel, Court Strong, Jan Paegle, and Marty Ralph for their thoughts and contributions to this dissertation. I thank my fellow employees at NWS Western Region HQ who have abided by my irregular schedule, and the researchers at NOAA/ESRL that I've had the pleasure of corresponding with. I thank my parents, James and Susanne Rutz, whose love and support have shown no limits. I gratefully acknowledge the provision of datasets, software, and/or computer time and services provided by NOAA, ECMWF, and the University of Utah Center for High Performance Computing. This research is based on work supported by a series of grants provided by the NOAA/NWS CSTAR program. Any opinions, findings, conclusions, or recommendations expressed in this dissertation are those of the author and do not necessarily reflect the views of NOAA or the NWS.

CHAPTER 1

INTRODUCTION

Atmospheric rivers (ARs) are long and narrow corridors that contain large values of vertically integrated water vapor transport (IVT; Newell et al. 1992; Newell and Zhu 1994; Zhu and Newell 1998). Though precise definitions vary, these features are responsible for a large fraction of global water vapor transport, despite covering only a small fraction of the Earth's surface. Within the classical cyclone model, ARs are related to warm conveyor belts (WCBs), or regions of moist, ascending air located ahead of the cold frontal zone (Browning 1971; Carlson 1980; Eckhardt et al. 2004). Within WCBs, moisture and ascent are typically maximized near the frontal zone, and it is this region of strong vapor transport that often describes an AR. The length (~10^3 km) and time (~1–10 days) scales commonly associated with ARs, combined with their large values of IVT, ensure that these features play a major role in the global transfer of heat and moisture. Because of this, ARs serve as important linking mechanisms between weather and climate (Ralph et al. 2006).

Over the northeastern Pacific, ARs are typically located along and ahead of cold-frontal zones that are associated with extratropical cyclones as they progress eastward. Local convergence of water vapor near these frontal zones and/or entrainment and transport from the tropics are the two processes largely responsible for the high water vapor content characteristic of ARs (Bao et al. 2006; Ralph et al. 2004; Stohl et al. 2008).

Over the ocean, vapor transport within ARs is typically largest between ~0.5–2 km above the surface, at a level where relatively large values of specific humidity coincide with enhanced low-level winds along the frontal zone (Ralph et al. 2004). Large values of vapor transport can extend up to ~5 km, but increasing winds above this level are often offset by the exponential decrease in water vapor, leading to much lower values. The intense IVT associated with ARs combined with the low static stability prevalent within them often results in high precipitation rates, particularly where an AR intersects a high topographical barrier (Junker et al. 2008; Neiman et al. 2002; Ralph et al. 2004).

The west coast of North America is one region where ARs frequently interact with high topography, and the hydrometeorological extremes associated with ARs along and near this coast are well documented. Between October 1997 and February 2006, all seven flooding events on California's Russian River were associated with ARs (Ralph et al. 2006). In early November 2006, an intense AR impacted Washington and Oregon, producing widespread accumulations of 20–50 cm of rain over the Cascades, and causing ~$50 million in regional damages (Neiman et al. 2008a). A less intense AR affected western Washington in January 2009, producing widespread accumulations of only 8–20 cm of rain, but causing ~$125 million in damages, as melting snow contributed to flooding (NOAA/NWS 2013). This case emphasizes that even those ARs that do not produce extreme precipitation can still lead to rapid and widespread flooding, as snow level heights play a major role in determining the timing of the hydrologic response (Lundquist et al. 2008).

ARs sometimes extend east of the Cascades-Sierra Ranges and impact portions of the interior western U.S. In January 1997, an AR made landfall along the northern coast

of California and produced heavy rain over the northern Sierra Nevada, which combined with high-elevation snowmelt to produce flooding within Reno, NV and surrounding areas (U.S. Dept. Interior 1997; Rigby 1998). Incredibly, total storm-related damage during this event was as high as ~$1.6 billion (NOAA/NWS 2013). An inland-penetrating AR impacted portions of the southwestern U.S. during January 2010, resulting in numerous precipitation records across the region, and substantial (up to 234 mm) contributions to snowpack snow-water equivalent (SWE). Even regions located seemingly deep within the interior can be affected by ARs, as evidenced in November 2006 when the same AR described by Neiman et al. (2008a) also impacted northern Idaho and northwestern Montana. In and around Glacier National Park, widespread accumulations of 12+ cm (and a maximum of 30 cm) and rapid high-elevation snowmelt led to numerous road washouts, destroyed bridges, and lowland flooding (Bernhardt 2006).

The linkage between ARs and heavy precipitation is not limited to the western U.S. A corridor of persistently strong water vapor transport, characteristic of an AR, was found to play a crucial role in the May 2010 flooding of Nashville, TN (Moore et al. 2012). Recent work has also identified a connection between ARs and precipitation over Chile, Great Britain, and mainland Europe (Lavers et al. 2011; Lavers and Villarini 2013; Viale and Nuñez 2011). It is likely that any landmass residing in the extratropics is prone to feeling the effects of ARs along its western coast.

The interactions of landfalling ARs with complex topography can produce strong gradients in precipitation. Ralph et al. (2003) described one such case along the central California coast and highlighted the sensitivity of rain-shadowed areas to small changes

in wind direction. Similarly, recent work using streamflow data has shown that when ARs impact western Washington, subtle differences in wind direction play a role in determining which river basins are likely to see anomalously high flows (Neiman et al. 2011). These interactions pose unique forecasting challenges, particularly with regard to the heaviest precipitation. During the 2005–2006 cool season, ARs were found to be associated with nearly all of the most extreme precipitation events near the U.S. west coast, but ~90% of precipitation forecasts for these events were too low (Ralph et al. 2010). One method shown to improve forecast skill is the utilization of standardized anomalies of moisture flux, which are positively correlated with major precipitation events over the Sierra Nevada (Junker et al. 2008).

Most ARs making landfall along the U.S. west coast experience moisture depletion as a result of precipitation (and also possibly divergence), which is often orographically enhanced. One study by Smith et al. (2010) investigated the moisture budget of an AR making landfall along the northern California coast and found a drying ratio (defined as the ratio of water vapor lost to water vapor transport over a given location [Smith et al. 2003]) of 49% between the coast and the lee of the northern Sierra, with components of 28% over the Coastal Mountains and 25% over the northern Sierra Nevada. Further south, within the topographical gap east of San Francisco, a much smaller drying ratio was found between the coast and the Central Valley. This water vapor depletion due to precipitation plays a key role in the process of airmass transformation described by Smith et al. (2003, 2005), which reflects the ascent (descent) and cooling (warming) of parcels on the windward (leeward) side of a topographical barrier as they pass over it.

The relationship between ARs or AR-like features and moist parcel trajectories has been explored within a number of studies. Lackmann et al. (1998) analyzed a major cool-season precipitation event over the Mackenzie River Basin (MRB) and found moisture transport from the Pacific Ocean to play a major role. They demonstrated that water vapor flux between 800-700 hPa was critical to achieving substantial transport over the Canadian Rockies into the MRB, and that this flux was related to surface-based PV anomalies. Stohl et al. (2008) used backward trajectory analysis to show that the majority of moist parcels contributing to a heavy rain event along the Norwegian coast originated along the path of an Atlantic AR. The concept of tropical moisture exports (TMEs) has been used to identify moist parcel trajectories originating in the tropics (equatorward of 20°N/S) and reaching the mid-latitudes (poleward of 35°N/S), and have been found to contribute to regional precipitation (Knippertz and Wernli 2010; Knippertz et al. 2013). Furthermore, TME outbreaks were found to be associated with the ARs identified by Dettinger et al. (2011) at rates of 80% and 90% (December–May), respectively, along the North American west coast from 32.5°–41°N and 41°–52.5°N.

Quantifying the climatological characteristics of ARs (frequency, duration, and influence on precipitation) over the western U.S. has been the subject of recent studies. Ralph et al. (2004) identified ARs as contiguous regions $\geq$ 2000 km in length and $\leq$ 1000 km in width, with IWV $\geq$ 20 mm throughout. These criteria were used by Neiman et al. (2008b) to construct an 8-year climatology of cool-season (November–April) ARs making landfall along the west coast of North America between 32.5°–52.5°N, which was subsequently updated to an 11-year climatology by Dettinger et al. (2011). The most recent of these showed that the number of cool-season ARs making landfall along the

North coast (41°–52.5°N) and the California coast (32.5°–41°N) was relatively equal. Both coastal segments experienced a decline in AR landfalls as the cool season progressed, but this decline was sharper along the North coast, where very few ARs were observed from February–April. From February–April, more AR landfalls were observed along the California coast. This pattern of AR seasonality bears some resemblance to that of the storm track discussed by Lareau and Horel (2012).

Recent studies by Ralph et al. (2011, 2013a) have shown that extreme storm-total rainfall and runoff at a given site are strongly tied to the duration of AR conditions. Using a 6-year dataset of hourly observations at a coastal observing site operated by NOAA's Hydrometeorology Testbed (HMT; hmt.noaa.gov; Ralph et al. 2013b) it was found that on average, AR conditions lasted 20 h at that location, and that the longest lasting cases (roughly the top 10%) lasted 40 h and produced 7 times the streamflow found in average events (Ralph et al. 2013a).

In addition to examining AR frequency along the coast, Dettinger et al. (2001) also explored the fraction of cool-season precipitation over the western U.S. that could be attributed to ARs. They found that 20–50% of the precipitation at most sites in California, Oregon, and Washington fell on the day of or day following persistent AR conditions along the U.S. west coast. Similarly, Guan et al. (2010) found that 30–40% of the snowpack SWE accumulation in the Sierra Nevada during water years 2004–2010 occurred on the day before, of, or following persistent AR conditions along the California coast. Further inland, Dettinger et al. (2011) found much lower contributions from ARs, particularly over the southwestern U.S. However, neither of these studies attempt to identify ARs over the western U.S. landmass because they are dependent on observations

available only over open water. A more spatially rigorous assessment of AR contributions to cool-season precipitation may provide more revealing results.

Our understanding of the relationship between ARs and hydrometeorological extremes has increased greatly over the past decade. However, the fate of these ARs as they interact with complex topography and attempt to penetrate into the interior western U.S. is not well understood. There has been no effort to objectively quantify the frequency and duration of ARs over the interior western U.S. and in addition, the preferred pathways of AR penetration into the interior are not known.

Furthermore, the influence of ARs on the hydroclimate of the interior western U.S. is not well understood. During 2000–2009, three of the four fastest growing states (Arizona, Nevada, and Utah) were located within this region (Bureau of the Census 2013), and with water resources already strained, an understanding of hydrologic inputs (i.e., precipitation) will become increasingly important (Bales et al. 2006). Much of the western U.S. requires less than 15 days yr^{-1} to accumulate half of annual precipitation (Dettinger et al. 2011), and at snowpack telemetry (SNOTEL) stations across the western U.S., the largest 72-h snowfall event in a given year typically accounts for 10-23% of annual snow water equivalent (SWE) at that location (Serreze et al. 2001). It is possible that ARs are associated with many of these major precipitation events, and that they are substantial contributors to seasonal precipitation as has been shown for cyclones (Hawcroft et al. 2012; Pfahl and Wernli 2012) and frontal zones (Catto et al. 2012), but more work is required to quantify these contributions.

The remainder of this dissertation is comprised of three chapters representing scholarly articles that have appeared in or have been submitted to peer-reviewed

academic journals related to the atmospheric sciences. Chapter 2 examines the contribution of ARs making landfall along the Baja Peninsula of Mexico to total cool-season precipitation over the southwestern U.S. Chapter 3 quantifies the climatological characteristics of ARs over the western U.S., and highlights preferred pathways of AR penetration into the interior. Chapter 4 uses trajectories initiated within ARs near the west coast to identify conditions that are favorable for the inland penetration of ARs.

CHAPTER 2*

QUANTIFYING THE ROLE OF ATMOSPHERIC RIVERS IN THE INTERIOR WESTERN UNITED STATES

Abstract

Atmospheric rivers (ARs) have increasingly been recognized for their contribution to high-impact weather and climate variability. A recent investigation based on observations located primarily in lowland valleys and basins of the western United States suggests that 10–50% of the total cool-season (November–April) precipitation between water years 1998 and 2008 occurred on the day of and day following AR landfall (hereafter the AR fraction), as identified using Special Sensor Microwave Imager data. However, these results are based only on ARs crossing the North American west coast between 32.5°N and 52.5°N, which excludes those crossing the west coast of the Baja Peninsula. Here, we identify ARs in the ERA-Interim reanalysis and examine the AR fraction at high-elevation observational sites and in the NOAA/CPC Unified Daily Precipitation Analysis. At high-elevation snowpack telemetry sites, we find good agreement with the AR fraction obtained previously for valley and basin locations. We also show that including ARs crossing the west coast of the Baja Peninsula (as far south as 24°N) substantially increases the AR fraction over the

---

southwestern United States.

Introduction

Nearly two decades ago, Newell et al. (1992) used the term "tropospheric river" to describe the filamentary corridors of moisture transport responsible for the majority of midlatitude atmospheric moisture flux. Since then, research has revealed much about the mesoscale structure of these features, now commonly referred to as atmospheric rivers (ARs), as well as their weather and climate impacts. As detailed by Ralph et al. (2004), most of the moisture flux associated with ARs takes place in the lower troposphere, along and ahead of cold fronts associated with extratropical cyclones. As such, the movement of extratropical cyclones and their attendant cold fronts largely dictates the behavior of ARs (Bao et al., 2006). Further, dramatic precipitation events and life-threatening flooding often occur when these ARs impinge on the high topography of western North America (Ralph et al., 2006; Neiman et al., 2008a).

Recently, Dettinger et al. (2011) used daily precipitation observations from National Weather Service Cooperative Observer Program (COOP) sites across the western United States, which are located primarily in lower elevation valley and basin locations, to assess the percentage of cool season (November to April) precipitation associated with landfalling ARs during water years 1998–2008. Following the methodology of Neiman et al. (2008b), they employed Special Sensor Microwave Imager retrievals of integrated water vapor (IWV) from two polar orbiting satellites, each passing over the region twice per day, but somewhat irregularly in space and time, to identify days during which ARs crossed the west coast of North America between 32.5°N and 52.5°N. They then calculated the amount of cool season precipitation produced on the day of and day following all AR landfalls, hereafter referred to

as the AR fraction.

Their results indicate that ARs contribute a significant fraction of total cool season precipitation at many COOP sites across the western United States (Figure 2.1). This is especially true near the coast, particularly in north/central California, where the AR fraction approaches 0.50. Inland from the coast, a less uniform pattern is observed – relatively high AR fractions are noted across the interior northwest, while the AR fractions across the interior southwest are very small, if not negligible. However, the southern limit of their analysis does not allow for identification of ARs crossing the west coast of the Baja Peninsula that penetrates into the southwestern United States.

Therefore, the objectives of this study are twofold: first, to determine if the AR fraction at higher elevations is comparable to those found at primarily lower elevation COOP sites by Dettinger et al. (2011); second, to examine if the inclusion of ARs crossing the west coast of the Baja Peninsula increases the AR fraction over the southwestern United States, as synoptic experience suggests.

Data and Methods

In order to assess the occurrence of ARs at uniform time intervals, we use 6-h observations of IWV at 1.5° resolution from the ERA-Interim reanalysis (Dee et al., 2011). Ralph et al. (2004) show that IWV, which is not dependent on an observed wind profile, is a good proxy for integrated atmospheric water vapor transport. Following the criteria developed and described by Ralph et al. (2004), and used in the creation of an AR event catalog by Neiman et al. (2008b), an AR is identified as a contiguous region $\geq$2000 km in length and $\leq$1000 km in width containing IWV values $\geq$20 mm. This is done objectively by first locating gridded data points of IWV $\geq$20 mm, and then determining the spatial extent of

such contiguous regions following an iterative approach: for each point identified, all neighboring points are then checked and added to the contiguous region if the IWV ≥20 mm. Distances between points within this region are then calculated to determine if the dimensional criteria are met. When an AR is identified along the west coast of North America between 24°N and 52.5°N (compared with 32.5°N and 52.5°N as in Dettinger et al., 2011) at all four daily analysis times (00, 06, 12, and 18 UTC), that day is counted as an AR day. The extension to 24°N enables us to include ARs that cross the west coast of the Baja Peninsula and may contribute to precipitation over the southwestern United States.

To examine whether the findings of Dettinger et al. (2011) extend to higher elevations, we use the ARs identified in the ERA-Interim reanalysis to determine the AR fraction at snowpack telemetry (SNOTEL) stations, which, using a large storage precipitation gauge, provide automated daily precipitation observations primarily at upper elevations (Hart et al., 2005; USDA-NRCS, 2009; USDA-NRCS, 2010; Rasmussen et al., 2011). We also examine the AR fraction in the NOAA/CPC Unified Daily Precipitation Analysis (hereafter the CPC Analysis), which provides spatially continuous 24-h precipitation analyses at 0.25° grid spacing (Higgins et al., 2000).

Results

Qualitatively, the spatial structure of our analysis, based on ARs identified using the ERA-Interim reanalysis, yields results largely consistent with those of Dettinger et al. (2011) (cf. Figures 2.1 and 2.2). This holds true whether using precipitation data from SNOTEL stations or the CPC Analysis. However, the AR fraction at almost all SNOTEL stations appears somewhat lower than those at adjacent COOP stations (cf. Figures 2.1 and 2.2a). This may suggest a subtle dependence with elevation of the role of ARs in producing cool-

season precipitation, and/or bias arising from differences in SNOTEL and COOP gauges and reporting techniques. In the case of the latter, most COOP precipitation observations are manually collected from unshielded 20-cm diameter gauges (NOAA-NWS, 1989; Daly et al., 2007), whereas SNOTEL precipitation observations are automated and collected from 30.5-cm diameter gauges with an Alter shield to help reduce wind effects on catchment and an oil-antifreeze additive to prevent freezing and reduce evaporative losses (Serreze et al., 1999). This could result in differing biases during AR and non-AR precipitation events, which ultimately affects the AR fraction.

AR fractions obtained using the CPC Analysis exhibit a similar spatial pattern to those of the COOP and SNOTEL stations (cf. Figures 2.1 and 2.2). This is advantageous in attempting to understand the role of ARs across the western United States, as it suggests that we may be able to use the gridded data to understand the role of ARs in regions where observations are sparse.

Earlier, we expressed concern that the AR fractions obtained by Dettinger et al. (2011) over the interior southwestern United States may be underestimated due to a lack of inclusion of ARs crossing the west coast of the Baja Peninsula. Extending the analysis of landfalling ARs southward from the United States/Mexico border to the southern tip of the Baja Peninsula, we find a substantial increase in AR fraction over the southwestern United States (cf. Figures 2.2 and 2.3). Specifically, the AR fraction increases by more than 0.15 in portions of southern California, Nevada, and Arizona (Figure 2.4a), with the percent change in AR fraction largest in Arizona and extreme southwestern New Mexico (Figure 2.4b). The average increase in precipitation on the days of and following AR landfall over all areas where the AR fraction increased by at least 0.15 is approximately 23 mm year−1, which is

substantial in an arid region. These results support the hypothesis that the inclusion of ARs crossing the west coast of the Baja Peninsula leads to substantially higher AR fractions across the interior southwestern United States than indicated in Dettinger et al. (2011).

Increases in AR fraction in other areas, such as Montana, are not believed to be the direct result of ARs crossing the west coast of the Baja Peninsula. Because AR precipitation anywhere in the western United States is based solely on the presence of ARs at the coast, some precipitation not directly related to ARs is included in the AR fraction. Therefore, a more likely explanation for the relatively minor increases in some regions is that they are the result of separate, distinct storm systems to the north of landfalling ARs on the west coast of the Baja Peninsula. Differentiating between precipitation falling in the presence of an AR at a specific location and that falling during the occurrence of an AR elsewhere is the subject of ongoing work.

Conclusions

The spatial pattern of western United States precipitation derived from landfalling ARs using COOP stations (Dettinger et al., 2011) is in good agreement with that shown here using data from the SNOTEL network and the CPC Analysis. Because sites within the SNOTEL network are generally located at higher elevations than COOP stations, this increases our confidence in the overall spatial pattern of AR fraction, and suggests that it is not highly dependent on elevation. We do, however, note an apparent tendency for smaller AR fractions at SNOTEL stations. We have also shown that including ARs along the west coast of the Baja Peninsula increases the AR fraction by at least 0.15 over much of the southwestern United States compared to the analysis of Dettinger et al. (2011), which considered only ARs intersecting the coast between 32.5°N–52.5°N. This has important

implications for understanding the role ARs play in determining water availability across the southwestern United States.

An underlying issue in the analysis presented here and in Dettinger et al. (2011) is that all precipitation over the western United States contributes to the AR fraction whenever an AR intersects the west coast. Given the geographic scales involved, this likely results in some precipitation not being related to the AR being included in the AR fraction, a problem that is likely exacerbated in our analysis by the inclusion of the west coast of the Baja Peninsula. On the other hand, the use of a 2-day time window (the day of and immediately following an AR landfall) likely eliminates some precipitation that may be related to the remnant AR as it moves inland. Future work is needed to deal with these ambiguities and gain a better understanding of the role of ARs in the hydroclimate of the western United States.

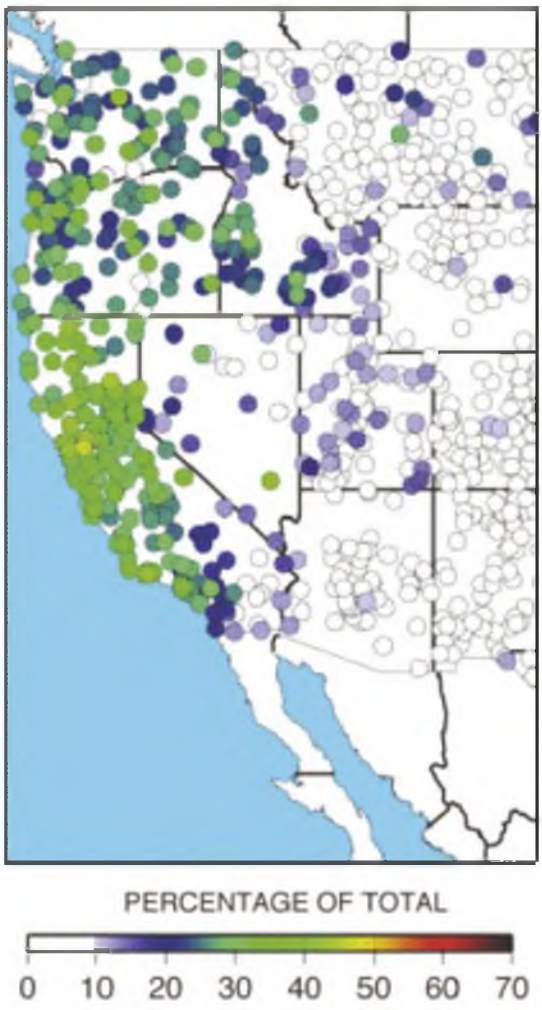

Fig. 2.1: Percentage of total cool-season (November to April) precipitation occurring at COOP weather stations the day of and the day following the occurrence of an AR crossing the west coast of North America (32.5°N–52.5°N) during water years 1998–2008 (Dettinger et al. 2011).

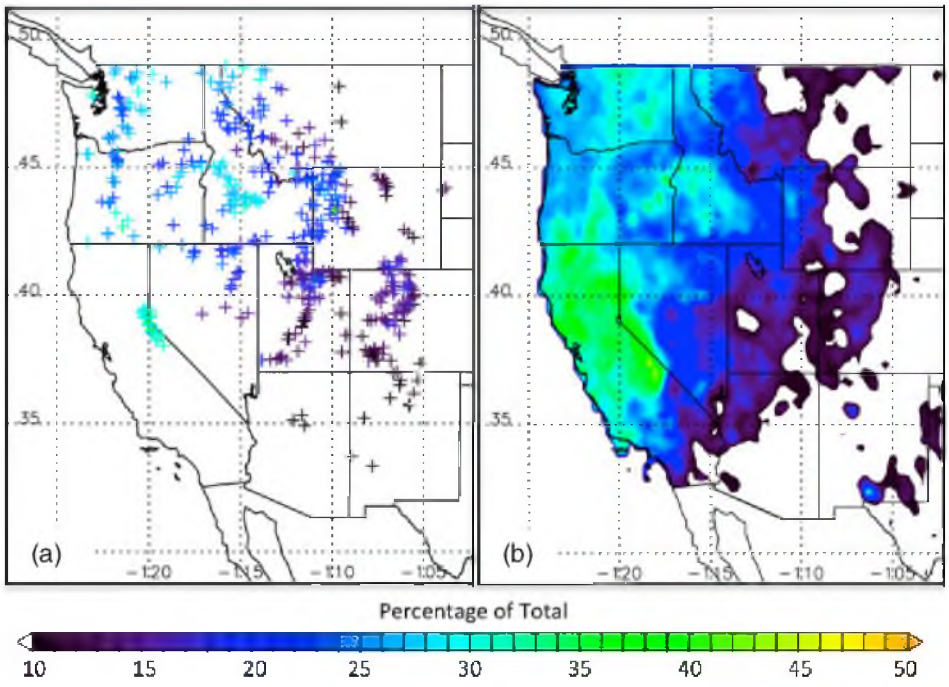

Fig. 2.2: Percentage of total cool-season (November to April) precipitation at (a) SNOTEL stations and (b) in the CPC analysis occurring on the day of and the day following the occurrence of an AR crossing the west coast of North America (32.5°N–52.5°N) during water years 1998–2008.

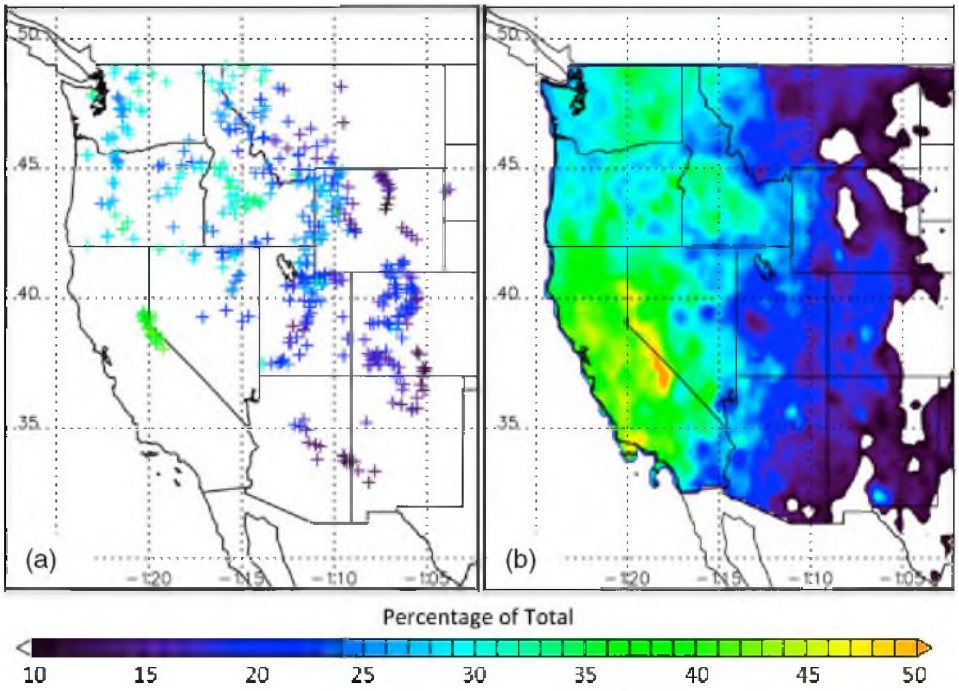

Fig. 2.3: Percentage of total cool-season (November to April) precipitation at (a) SNOTEL stations and (b) in the CPC analysis occurring on the day of and the day following the occurrence of an AR crossing the west coast of North America, including the west coast of the Baja Peninsula (24.0°N–52.5°N) during water years 1998–2008.

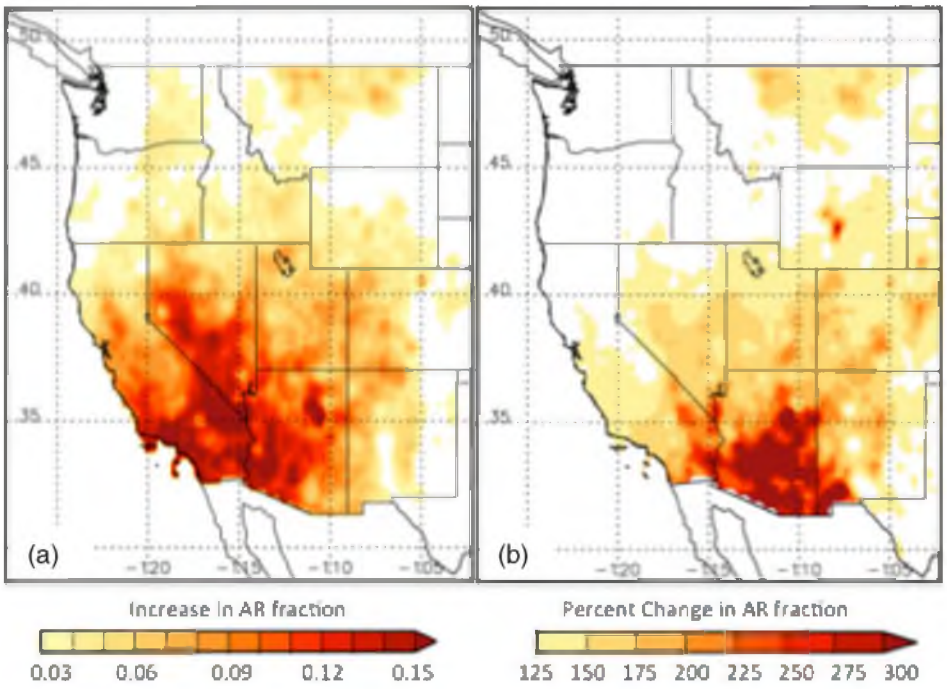

Fig. 2.4: Increase (a) and percent change (b) in AR fraction due to the addition of ARs crossing the west coast of the Baja Peninsula (24.0°N–32.5°N).

CHAPTER 3*

CLIMATOLOGICAL CHARACTERISTICS OF ATMOSPHERIC RIVERS AND THEIR INLAND PENETRATION OVER THE WESTERN UNITED STATES

Abstract

Narrow corridors of water vapor transport known as atmospheric rivers (ARs) contribute to extreme precipitation and flooding along the west coast of the U.S., but knowledge of their influence over the interior is limited. Here, we use ERA-Interim reanalysis data, CPC precipitation analyses, and SNOTEL observations to describe the characteristics of cool-season (November–April) ARs over the western U.S. We show that AR frequency and duration exhibit a maximum along the Oregon/Washington coast, a strong transition zone upwind (west) of and over the Cascade–Sierra Ranges, and a broad minimum that extends from the "high" Sierra south of Lake Tahoe eastward across the central Great Basin and into the deep interior. East of the Cascade–Sierra Ranges, AR frequency and duration are largest over the interior northwest, while AR duration is large compared to AR frequency over the interior southwest.

The fractions of cool-season precipitation and top-decile 24-h precipitation events

---

attributable to ARs are largest over and west of the Cascade–Sierra Ranges. Further east, these fractions are largest over the northwest and southwest interior, with distinctly different large-scale patterns and AR orientations enabling AR penetration into each of these regions. In contrast, AR-related precipitation over the Great Basin east of the high Sierra is rare. These results indicate that water vapor depletion over major topographic barriers is a key contributor to AR decay, with ARs playing a more prominent role in the inland precipitation climatology where lower or less continuous topography facilitates the inland penetration of ARs.

Introduction

Atmospheric rivers (ARs) are narrow corridors of strong vertically integrated water vapor transport (IVT) that are responsible for nearly 90% of the extratropical poleward water vapor transport despite covering only 10% of the available longitude (Newell et al. 1992; Newell and Zhu 1994; Zhu and Newell 1998). ARs are often aligned along and ahead of cold fronts associated with extratropical cyclones, and achieve their high water vapor content through transport from the tropics and/or local moisture convergence (Ralph et al. 2004; Bao et al. 2006; Stohl et al. 2008). Thus, many ARs are related to warm conveyor belts—moist, ascending air streams located within the warm sector of extratropical cyclones (Browning 1971; Carlson 1980; Eckhardt et al. 2004; Sodemann and Stohl 2013). Due to strong water vapor transport and low static stability, ARs can produce heavy precipitation, particularly when directed towards topographical barriers (e.g., Neiman et al. 2002; Ralph et al. 2004; Junker et al. 2008). This orographic precipitation acts to decrease the water vapor transport as an AR penetrates inland.

The hydrometeorological extremes associated with ARs are well documented,

especially along the west coast of North America. Ralph et al. (2006) showed that all seven major flood events on northern California's Russian River between October 1997 and February 2006 were associated with landfalling ARs. An intense AR produced destructive flooding during November 2006 over parts of Oregon and Washington (Neiman et al. 2008a), and the same region experienced a prolonged period of heavy rainfall during March 2005 owing to interactions between an AR and a mesoscale frontal wave (Ralph et al. 2011). Warner et al. (2012) showed that most of the heavy precipitation events over the coastal northwestern U.S. during the past 60 years were associated with AR conditions. Neiman et al. (2011) showed that ARs were associated not only with heavy rain, but with extreme streamflow on four watersheds in Washington based on satellite observations of ARs and stream gauge data. Beyond the west coast of North America, high-impact weather associated with ARs has been documented over eastern North America, Great Britain, and Chile (e.g., Lavers et al. 2011; Viale and Nuñez 2011; Moore et al. 2012).

Recent studies by Ralph et al. (2011, 2013a) document the importance of persistent AR conditions in generating the most extreme storm-total rainfall and flooding. Using unique, long-term (6 years) hourly observations of AR conditions at a coastal observing site operated by NOAA's Hydrometeorology Testbed (HMT; hmt.noaa.gov; Ralph et al. 2013b), they found that AR conditions lasted an average of 20 h, but the most persistent events (roughly the top 10%) lasted an average of 40 h and produced 7 times the streamflow found in average events (Ralph et al 2013a). Thus, forecasting extreme precipitation and flooding in the region requires accurate prediction of both the intensity and duration of AR conditions, especially over key topographic obstacles and flood-prone

drainages.

Some ARs extend across the Cascade–Sierra Ranges, or across the mountains of southern California and the Baja Peninsula, and contribute to heavy precipitation and flooding over the interior western U.S. In January 1997, an AR contributed to heavy rain along the snow-covered eastern slopes of the Sierra Nevada, leading to flooding that inundated ~64,000 acres and produced $540 million in damage along the Truckee, Carson, and Walker Rivers (U.S. Dept. Interior 1997; Rigby 1998). During January 2010, an inland-penetrating AR produced heavy precipitation (including numerous 2-day accumulation records for January) and flooding across the southwestern U.S., especially Arizona (Neiman et al. 2013). At upper elevations during this event, snowpack snow-water equivalent (SWE) increased as much as 234 mm, a consequence of snow accumulations and/or the absorption of rain by the snowpack. In November 2006, an AR contributed to heavy rainfall (widespread accumulations of 12+ cm with a maximum of 30 cm) and rapid high-elevation snowmelt that led to numerous road washouts, destroyed bridges, and lowland flooding in and around Glacier National Park (Bernhardt 2006).

Several recent studies have estimated the contribution of ARs to total cool-season (November–April) precipitation over the western U.S. Dettinger et al. (2011) used precipitation observations from National Weather Service Cooperative Observer (COOP) sites in the western U.S. to examine the fraction of cool-season precipitation associated with landfalling ARs (hereafter the AR fraction) during water years 1998–2008. During this period, 20–50% of the precipitation at most COOP sites in California, Oregon, and Washington fell on the day of or day following AR observation along the U.S. west coast, as identified using Special Sensor Microwave/Imager (SSM/I) retrievals of integrated

water vapor (IWV) [ARs defined following Ralph et al. (2004) as contiguous regions ≥ 2000 km long and ≤ 1000 km wide with IWV ≥ 20 mm]. Similarly, Guan et al. (2010) found that 30–40% of the snowpack SWE accumulation in the Sierra Nevada during water years 2004–2010 occurred on the day before, of, or following AR observation (as described above) along the California coast. Further inland, Dettinger et al. (2011) found lower AR fractions, especially over the southwestern U.S., although Rutz and Steenburgh (2012) show that the AR fraction over the southwestern U.S. is larger if ARs crossing the west coast of the Baja Peninsula are considered (Dettinger et al. 2011 did not consider ARs crossing along the Baja Peninsula). However, none of these studies attempt to identify ARs over the interior western U.S. or account for their spatial extent when quantifying AR-related precipitation.

This paper uses gridded atmospheric analyses and daily precipitation datasets (gridded and gauge) to expand our knowledge of cool-season ARs over the western U.S. In particular, we use new methods to identify ARs in reanalysis data and examine their climatological characteristics (frequency, duration, and influence on precipitation) from the coast into the western interior. These methods, which have the potential for broader applications in weather, hydrological, and climate research and forecasting, are described in Section 2, with results related to the frequency, duration, and seasonal precipitation and extreme events presented in sections 3–5. Discussions, conclusions, and future work are summarized in sections 6 and 7.

Data and Methods

Data Sources

We identify ARs using the ERA-Interim reanalysis (Dee et al. 2011), which is based on a version of the European Centre for Medium-Range Weather Forecasts (ECMWF) Integrated Forecast System (IFS) with 60 vertical levels (extending to 0.1 hPa), T255 triangular truncation for dynamical fields, and a reduced Gaussian grid with ~80-km spacing for surface and other grid point fields (Simmons et al. 2007; Uppala et al. 2008; Berrisford et al. 2009). The ~80-km Gaussian grid spacing provides a reasonable estimate of the effective grid spacing of the ERA-Interim in physical space (Kanamitsu 1989). The ERA-Interim data used here cover cool-season months (November–April) from November 1988 through April 2011, a total of 23 seasons, and were obtained from the ECMWF data server on a 1.5° latitude × 1.5° longitude grid with 6-h temporal resolution. Although the ERA-Interim provides sufficient spatial and temporal continuity for AR identification, neither the 1.5° grid nor the native ERA-Interim grid fully resolves the complex topography of the western U.S. (cf. Figs. 3.1a,b). This limited resolution may artificially smooth some sub-synoptic-scale gradients, such as those associated with orographic processes over mountain barriers.

Precipitation observations and analyses come from the gridded NOAA/Climate Prediction Center (CPC) Unified Daily Precipitation Analysis (hereafter the CPC analysis) and the Snowpack Telemetry (SNOTEL) network of stations maintained by the National Resources Conservation Service (NRCS). The CPC analysis provides spatially continuous (0.25° grid spacing) 24-h precipitation analyses valid at 1200 UTC (Higgins et al. 2000). SNOTEL stations, using a large storage gauge and an Alter shield to reduce

the effects of wind, provide automated precipitation observations at upper elevation sites (Hart et al. 2005; Rasmussen et al. 2011; USDA-NRCS 2012a,b).

SNOTEL observations are available both hourly and daily, but the latter are for 0000–0000 PST. To facilitate comparisons between SNOTEL observations and the CPC analysis, we use the hourly SNOTEL accumulated precipitation data to construct a set of 24-h accumulations valid at 1200 UTC. These data are quality controlled following Serreze et al. (1999) except that we allow the daily precipitation to be as large as 20 inches (~51 cm) instead of 10, and more than five standard deviations above the mean. This allows for the inclusion of some extreme events. Only sites that are operational throughout the study period are used.

Objective Identification of Atmospheric Rivers

ARs are objectively identified in the ERA-Interim using two definitions. The first, IVT_{250}, defines an AR as a contiguous region ≥ 2000 km in length with IVT ≥ 250 kg m^{-1} s^{-1}. Here, IVT is defined as

$$IVT = \frac{1}{g}\int_{p_{sfc}}^{100\ hPa} q\boldsymbol{V}\, dp \quad (1)$$

where g is the gravitational acceleration, q is the specific humidity, $\boldsymbol{V}$ is the total vector wind, p is pressure, and p_{sfc} is the surface pressure. The integration is done using data at the surface, 50 hPa intervals from the surface to 500 hPa, and 100 hPa intervals from 500 hPa to 100 hPa. The second, IWV_{20}, defines an AR as a contiguous region ≥ 2000 km in length with IWV ≥ 20 mm. Here, IWV is defined as

$$IWV = \frac{1}{g}\int_{p_{sfc}}^{100\,hPa} q\,dp \quad (2)$$

with the integration done as described above. Both IVT and IWV are then interpolated to the CPC analysis grid to facilitate the attribution of precipitation to ARs, as described in the following section. In both cases, the AR length criterion is evaluated as the greatest distance between two points within each contiguous feature.

Previous work based on SSM/I satellite data uses IWV_{20} as a proxy for AR identification in lieu of the wind observations necessary to calculate IVT (e.g., Ralph et al. 2004; Neiman et al. 2008b; Dettinger et al. 2011). Whereas some results are presented based on IWV_{20}, we focus on IVT_{250} for two reasons. First, IVT is strongly related to precipitation over complex terrain (Neiman et al. 2002, 2013; Junker et al. 2008; Ralph et al. 2013a) and more strongly correlated with cool-season precipitation over most of the western United States than IWV (Fig. 3.2). Second, subjective evaluation of numerous AR events reveals that areas of IVT $\geq$ 250 kg m^{-1} s^{-1} crossing the west coast of North America penetrate further into the interior than coinciding areas of IWV $\geq$ 20 mm and correspond well with the spatial extent of heavy precipitation (e.g., Fig. 3.3). The use of IVT also aids in overcoming the limitations associated with the reduction of overall atmospheric thickness and IWV over elevated terrain.

In contrast to earlier studies (e.g., Ralph et al. 2004; Neiman et al. 2008b; Dettinger et al. 2011; Wick et al. 2013), AR width is not considered in the identification process. ARs identified using the IVT_{250} criteria rarely exceed 1000 km in width, whereas those that do still tend to possess AR characteristics (e.g., large length to width

ratio and intense lower-tropospheric water vapor flux).

Attribution of Precipitation to Atmospheric Rivers

The precipitation from the CPC analysis is defined as AR-related if an AR is identified at a given grid point during any of the five 6-h analysis times during the 24-h accumulation period (1200–1200 UTC). For precipitation at SNOTEL stations, the closest grid point is used to make this determination. We then define the AR fraction as the fraction of total cool-season precipitation that is AR related. To assess the role of ARs in major precipitation events, we also examine the fraction of top-decile 24-h precipitation events exceeding 0.1 inches (2.54 mm, the resolution of the SNOTEL data) that are AR related (hereafter top-decile fraction). By defining precipitation as AR-related only where ARs are observed, this approach is more geographically specific than earlier studies (e.g., Dettinger et al. 2011; Rutz and Steenburgh 2012), but the requirement of an AR to be present at only one analysis time is the most generous possible. Smaller AR fractions and top-decile fractions are obtained if an AR is required to be present at multiple analysis times.

AR Frequency and Duration

AR Frequency

Based on IVT_{250}, the AR frequency (i.e., the fraction of 6-h analysis times meeting the AR identification criteria) over the western U.S. is characterized by a maximum (> 15%) along the Oregon/Washington coast and a broad minimum (<5%) over the deep interior, southwest, and Great Basin east of the high Sierra (Fig. 3.4a, see Fig. 3.1 for geographic references). The coastal AR frequency decreases rapidly from Cape Mendocino south to Point Conception. East of the Cascade–Sierra Ranges, the AR

frequency is greatest over a low-elevation corridor that extends across the Columbia Basin into northern Montana, and within the Snake River Plain and adjoining northern Great Basin.

For comparison, the IWV_{20} AR frequency is greatest along the coast of northern California, with a decrease in frequency along the Oregon/Washington coast to the north and the central California coast to the south (Fig. 3.4b). Locations with an AR frequency > 5% are limited to within ~100 km of the coast, with the greatest values found over the Columbia Basin, Central Valley, and the lower Colorado River Basin. Compared with IVT_{250}, fewer IWV_{20} ARs penetrate into the interior western U.S. except over the lower Colorado River Basin (cf. Fig. 3.4a,b). Given that the IWV_{20} AR frequency over the interior is so low, as well as reasons discussed in the previous section, we focus on IVT_{250} ARs for the remainder of this paper.

The value of IVT chosen as a threshold to identify ARs affects the magnitude of AR frequency over the western U.S., with lower (higher) thresholds yielding higher (lower) frequencies, but does not significantly alter the locations of AR frequency maxima or minima (cf. Figs. 3.4a and 3.5a,b). Changes in the observed pattern and magnitude of AR frequency found by varying the length criterion between 1500 and 2500 km are negligible (not shown).

The seasonality of AR frequency is characterized by a November maximum over the northern half of the western U.S., but a more complex distribution over the southern half (Fig. 3.6). Much of northern and central California, northwestern Nevada, eastern Arizona, and parts of western Colorado feature a December maximum, whereas a January maximum is found over southern California, southern Nevada, extreme southwestern

Utah, and western Arizona. Eastern Colorado features an April maximum, likely reflecting the contribution of low-level water vapor transport from the Gulf of Mexico during the spring. Histograms at selected coastal and interior locations further illustrate the AR seasonality. In the northern half of the western U.S., coastal location A and interior location B observe a primary maximum in November and a secondary maximum in January, after which there is a monotonic decline in AR frequency during the later half of the cool season. The monthly distribution at coastal locations C and E is quasi-normal, and illustrates the increasingly later peak in AR frequency southward along the west coast. Over the southern interior, events at locations D and F are relatively rare and the seasonality is not well defined.

AR Duration

The mean AR duration, which is defined as the average number of hours of AR conditions experienced at a given location during an AR event (Ralph et al. 2013a), is greatest along the Oregon coast (23–24 h) and is co-located with the maximum in AR frequency (Fig. 3.7). Along the coast to the north and south of this maximum, the mean AR duration declines to ~19 h on the northwest tip of the Washington coast and ~17 h near Point Conception. East of the Cascade–Sierra Ranges, the mean AR duration is greatest over the Columbia Basin and northern Montana, within the Snake River Plain and adjoining northern Great Basin, and over southern California, Arizona, and New Mexico. The mean AR duration is smallest (~12 h) along a corridor that extends from the high Sierra eastward across the central Great Basin and into the Rocky Mountains, aligning well with regions of smallest AR frequency. South of this corridor, the low AR frequency and higher AR duration suggests that ARs over the southwestern U.S. tend to

be infrequent, but relatively long-lived (cf. Figs. 3.4a and 3.7).

Because high-impact precipitation events are often the result of long-lived, persistent AR conditions (Ralph et al. 2011, 2013a; Moore et al. 2012), we also present histograms of AR duration at the same coastal and interior locations identified earlier. Both the coastal and interior locations have skewed distributions, but the latter have a greater frequency of short events and fewer long-duration events (Fig. 3.7). The frequency of AR events lasting only 6 h (i.e., one analysis time) nearly doubles from the coastal to the interior locations, whereas the frequency of AR events > 12 h (i.e., 3 or more analysis times) decreases from ~50% at the coastal locations to ~20–40% at the interior locations. Thus, there is a clear decline in duration of AR events from the coast to the interior. At location C, we find a mean AR duration of ~20 h, which agrees remarkably well with the independent and observationally based findings of Ralph et al. (2013a) at nearby Bodega Bay, CA. Furthermore, our top-decile AR duration threshold of ~40 h (not shown) is also in very good agreement with their findings, although we note the difference in temporal resolution (6 h here, 1 h in Ralph et al. 2013a). These results increase confidence in the use of ERA-Interim analyses and the IVT_{250} definition used to identify ARs.

AR Impacts on Cool-season Precipitation and Extreme Daily Precipitation

Fraction of Cool-season Precipitation Associated with AR Events ("AR Fraction")

Based on the CPC analysis, the coastal AR fraction is largest (> 0.60) north of San Francisco Bay, and decreases gradually to the south (Fig. 3.8a). A gradual decrease in AR fraction also extends from the west coast to the lee of the Cascade–Sierra Ranges,

where a more abrupt decrease exists, particularly in the lee of the Sierra Nevada. A weaker gradient is found over southern California where the topography is lower and less continuous than that of the high Sierra. The gradient in AR fraction found along the Cascade–Sierra Ranges likely reflects water vapor depletion during orographic precipitation (e.g., Smith et al. 2005; Smith et al. 2010), resulting in fewer and/or less intense (i.e., smaller IVT) ARs further inland.

Further inland, the AR fraction is largest (~0.25–0.45) over the interior northwestern and southwestern U.S., and smallest (< 0.25) over the intermediate Great Basin. Over the interior northwestern U.S., the strongest gradient occurs over the central Idaho mountains and northwestern Montana, whereas over the interior southwestern U.S., the strongest gradient exists over the Mogollon Rim and higher terrain to the east and northeast. Low AR fraction values over the Great Basin extend eastward across Utah and join the broad minimum (< 0.10) over the mountains and highlands of the deep interior.

There is generally good agreement between the AR fraction obtained using the CPC analysis and SNOTEL observations (cf. Figs. 3.8a,b), but some important differences exist. To highlight these differences, we select five geographic regions, each characterized by an AR frequency of ≥ 3% (see Fig. 3.4a), and compare the AR fraction obtained from the SNOTEL observations to that obtained by interpolating the CPC analysis to the SNOTEL locations. These five regions, identified in Fig. 3.8b, are the Cascades, the Sierra Nevada, the northern Rockies, northeast Oregon, and the southwest central Idaho mountains.

The AR fraction based on the interpolated CPC analysis is generally greater and less regionally varied than that based on the SNOTEL observations (Fig. 3.9). The

median CPC AR fraction is 0.07 greater than the median SNOTEL AR fraction over the Sierra Nevada and 0.01–0.03 greater over the Cascades, northeast Oregon, and the southwest central Idaho mountains, all of which are significant at the 95% confidence level following Student's *t*-test (used here and elsewhere for significance testing). Only over the northern Rockies is the median CPC AR fraction smaller (by 0.01) and this result is not significant at the 95% confidence level. The interquartile range in CPC AR fraction over the Cascades, Sierra Nevada, northeast Oregon, and the southwest central Idaho mountains is also smaller than those from the SNOTEL observations. For example, over the Cascades the interquartile range of the AR fraction based on the CPC analysis is only 0.04, but is 0.07 based on SNOTEL observations. Only over the northern Rockies is the interquartile range based on the CPC analysis greater. Thus, while the CPC AR fraction is characterized by a relatively smooth, monotonic decline from the coast to the interior, the AR fraction at SNOTEL stations indicates smaller-scale spatial variability embedded within this decline. This smaller-scale variability is likely due to the modulation of AR and non-AR precipitation by local and regional orographic effects.

The ratio of AR fraction to AR days [i.e., any 24-h accumulation period (1200–1200 UTC) period with AR-related precipitation] provides a measure of the dependence of total cool-season precipitation on the occurrence of a small number of ARs (Fig. 3.10). This ratio (multiplied by 100 for convenience) is largest (> 3) over the southwestern U.S., with a pronounced maximum over the high Sierra (> 6), and smallest (< 2) over the northwestern U.S. This implies that a large fraction of the cool-season precipitation over the southwestern U.S. is produced by a small number of ARs, which is consistent with previous studies (Dettinger et al. 2011; Neiman et al. 2013). Secondary maxima exist

over the San Juan Mountains, the southwest central Idaho mountains, portions of the adjoining Snake River Plain, and eastern Colorado, with the latter likely related to water vapor transport from the Gulf of Mexico.

Fraction of Top-decile 24-h Precipitation Events Associated with ARs ("Top-decile Fraction")

Based on the CPC analysis, the top-decile fraction follows a pattern similar to that of the AR fraction, but exhibits more spatial variability and stronger gradients (Fig. 3.11a, note that color-fill interval is double that for AR fraction). The top-decile fraction is largest (> 0.75) along the coast north of San Francisco Bay and decreases along the coast to the south. Values decrease gradually inland from the coast before a more abrupt decrease in the lee of the Cascade–Sierra Ranges. South of the Sierra Nevada, the top-decile fraction exhibits a well-defined gradient over the mountains of southern California, which is less evident in the AR fraction.

East of the Cascade–Sierra Ranges, the top-decile fraction is largest (> 0.25) over portions of the interior northwestern and southwestern U.S. Over the interior northwestern U.S., the top-decile fraction is largest (> 0.35) over the western part of the northern Rockies, northeast Oregon, and the southwest central Idaho mountains. These are mountain regions that are exposed to flow from the southwest and west. Transitions to lower fractions also exist as one moves eastward across the northern Rockies and northeastward across the central Idaho mountains. Over the southwestern interior, the top-decile fraction decreases over and northeast of the Mogollon Rim. The smallest top-decile fractions (< 0.15) extend from the lee of the high Sierra eastward across the central Great Basin to the mountains and highlands of the deep interior.

There is generally good agreement between the spatial patterns of top-decile fraction using the CPC analysis and SNOTEL observations, but important differences are found at some locations (cf. Figs. 3.11a,b). To compare further, we examine the SNOTEL and interpolated CPC distributions within the five geographic regions identified earlier.

Similar to the results for the AR fraction, the top-decile fraction from the CPC analysis is generally greater and less regionally varied than that based on the SNOTEL observations (Fig. 3.12). The median CPC top-decile fraction is 0.14 greater than the median SNOTEL top-decile fraction over the Sierra Nevada, 0.03–0.04 greater over the Cascades and the southwest central Idaho mountains, all of which are significant at the 95% confidence level. The median CPC top-decile fraction is 0.01–0.02 smaller over the northern Rockies and northeast Oregon, neither of which is significant at the 95% confidence level. The interquartile range of the CPC top-decile fraction over the Cascades, Sierra Nevada, and northeast Oregon is smaller than those from the SNOTEL observations, but is greater over the northern Rockies and the southwest central Idaho mountains. As for the AR fraction, these results suggest that the regional variability in top-decile precipitation is dependent on local and regional orographic effects. Furthermore, this variability, as measured by the interquartile range, is greater for the top-decile fraction than for AR fraction (cf. Figs. 3.9 and 3.12).

Penetration of ARs into the Interior Western U.S.: Pathways and Synoptic Patterns

To help illustrate preferred pathways for AR penetration into the interior without the need to track individual ARs, we compute the conditional frequency of AR conditions

across the eastern Pacific and western United States in all analyses (i) 24-h prior to (–24 h) and (ii) during (0 h) the existence of AR conditions at five locations along the 111°W meridian. We use composite (i.e., mean) 500-hPa geopotential height analyses to illustrate the accompanying large-scale pattern. The resulting analysis illustrates the contrast in AR pathways and associated synoptic patterns over the northwest and southwest interior.

For the two locations over the northwest interior, the conditional frequency of AR conditions is largest in an elongated band that extends northeastward across the eastern Pacific Ocean and curves anticyclonically into the interior, with the largest values moving from near and upstream of the Oregon and Washington coast to the northwest interior from –24 to 0 h (Figs. 3.13a–d). The accompanying 500-hPa composite features a weakly progressive long-wave pattern with enhanced southwesterly flow between a trough over the north Pacific and a ridge over the western United States. High conditional AR frequencies extend through the ridge axis at 0 h. In contrast, for the two locations over the southwest interior, the conditional frequency of AR conditions is largest off the California coast at –24 h. This maximum moves inland and exhibits weak cyclonic curvature at 0 h (Figs. 3.13g–j). The accompanying 500-hPa composite features a trough off the California coast that moves eastward over the southwest.

For the location over northern Utah, the conditional frequency of AR conditions at –24 h features a quasi-zonally oriented band that extends across the eastern Pacific, with a broad maxima near the Oregon and northern California coast (Figs. 3.13e,f). At 0 h, the pattern is bifurcated with a primary (secondary) band of high values to the north (south) of the high Sierra. These bands merge into a maximum over northern Utah. This

bifurcated pattern reflects two pathways for AR penetration into northern Utah, one to the north of the high Sierra, the other to the south. The 500-hPa composite features predominantly zonal flow, which does not reflect the dominant flow pattern, but rather an averaging of patterns associated with ARs penetrating into the Great Basin to the north or south of the high Sierra.

Similar results are obtained along nearby meridional transects, suggesting that two broad, favored pathways for AR penetration flank the high Sierra, with AR penetration into the interior northwest (southwest) typically occurring within regions of anticyclonic (cyclonic) curvature north (south) of this range. The intermediate eastern Great Basin represents a transition zone in which ARs are rare and short lived, but can be affected by AR pathways to the north or south of the high Sierra.

Discussion

In an Eulerian framework, the local time tendency of IVT is a function of IVT divergence, evaporation, and precipitation. Assuming no evaporation over land, IVT convergence increases IVT, while IVT divergence and precipitation decrease IVT. Hence, ARs defined on the basis of IVT are prone to rapid decay (i.e., the decrease in size and IVT magnitude, possibly to the point of disappearance of an AR) over the same regions where their effects (e.g., heavy precipitation and flooding) are most severe. Additionally, due to the climatological decrease of water vapor with height, IVT is typically sensitive to the surface pressure, which is much lower over higher elevation regions, contributing to smaller IVT values.

With the above in mind, our results indicate that the climatology of ARs and AR-related precipitation over the western U.S. is strongly influenced by three major factors.

The first is the climatological characteristics of ARs along the west coast, which influences the frequency, intensity (i.e., the magnitude of IVT), duration, and orientation of ARs as they begin to penetrate into the interior. The second is the local depletion of water vapor by precipitation, especially as air moves over high mountain barriers, which contributes to AR decay by reducing the IWV and corresponding water vapor transport. The third is the general increase in surface elevation and decrease in pressure that occurs from the U.S. west coast higher elevation locations in the interior.

Over the northwestern U.S., the AR frequency decreases rapidly from the coast to the lee of the Cascades and then more gradually across the interior (Fig. 3.4a). An axis of high AR frequency and mean duration is found along a relatively low-elevation corridor that extends from the Columbia Basin into northern Montana (Figs. 3.4 and 3.7). This leads to higher AR and top-decile fractions across northern Idaho and northwestern Montana, including Glacier National Park, than found over southwest Montana and the northeast central Idaho mountains (Fig. 3.8). A second axis of high AR frequency extends into the Snake River Plain and the adjoining central Idaho mountains. The strong, near monotonic decrease in AR and top-decile fractions from southwest to northeast across the central Idaho mountains (Fig. 3.14) likely reflects vapor depletion and airmass transformation as orographic precipitation is generated in the westerly and southwesterly flow that frequently accompanies ARs over the region (e.g., Fig. 3.13). In contrast, the AR and top-decile fractions feature more spatial variability over northeast Oregon, northern Idaho, and northwestern Montana where the ranges lack a sustained high-mountain mass and feature a variety of orientations, geometries, and exposures to westerly and southwesterly flow.

Over the southwestern U.S., the mountains of southern California and the Baja Peninsula are narrower and less continuous than the Cascades–Sierra Ranges, resulting in less airmass transformation and a more modest decline in AR frequency from the coast to the interior. Although the AR frequency is lower than over the northwestern U.S., the AR and top-decile fractions over southern and central Arizona are greater than those found east of the Oregon and Washington Cascades. This suggests that the occurrence or nonoccurrence of a small number of AR events strongly influences the cool-season hydroclimate of the southwest, a result that is broadly consistent with Dettinger et al. (2011).

Over the central Great Basin, ARs are short-lived and rare, owing to the southward decrease in coastal AR frequency combined with the effects of the high Sierra. Additionally, the AR fraction and top-decile fraction are very low across this region. ARs that penetrate into the interior rarely extend over the high Sierra, which induce AR decay, but more frequently penetrate inland either to the north or south of this range (Fig. 3.13).

The AR fraction found in this study differs from that found by Dettinger et al. (2011) and Rutz and Steenburgh (2012). For example, this study finds a decrease in AR fraction from the west coast to the lee of the Cascade–Sierra Ranges, where a more abrupt decrease exists, particularly in the lee of the Sierra Nevada. In contrast, both Dettinger et al. (2011, see their Fig. 3.6) and Rutz and Steenburgh (2012, see their Fig. 2.3) show little decline in AR fraction from the coast to the lee of the Cascades (Rutz and Steenburgh 2012 even found higher AR fractions east of the Washington Cascades than to the west). Dettinger et al. (2011) do illustrate a decrease in AR fraction across the

Sierra Nevada, but Rutz and Steenburgh (2012) find a maximum over the Sierra Nevada, with the strongest decrease further to the east over central Nevada.

Fundamentally, these differences are likely produced by our geographically specific method of attributing precipitation to ARs, which accounts for the decay of inland-penetrating ARs, whereas Dettinger et al. (2011) and Rutz and Steenburgh (2012) simply attribute all western U.S. precipitation to ARs on the day of or day following AR observation along the coast, rather than at the inland gauge locations. Our method constrains precipitation attributed to ARs to that occurring only at locations where AR conditions are observed, resulting in a decline in inland AR-related precipitation due to AR decay. This approach offers the advantage of geographic specificity (e.g., non-AR precipitation in the northwest is not considered when there is an AR over the southwest), but also neglects precipitation that may be related to water vapor transport downstream from a decayed AR into the interior western U.S. Ultimately, the definition of AR precipitation is somewhat ambiguous using daily totals (although Ralph et al. 2013a found agreement between hourly resolved observations of AR conditions and precipitation at a key coastal observing site and findings by Dettinger et al. 2011 that used daily COOP precipitation observations in the region). The method used here depends on daily data, applies a measure of geographic specificity, and accounts for AR penetration inland from the coast, thus providing a new perspective on the relationship between ARs and precipitation over the interior western U.S.

Our findings also depend on the characteristics of the underlying data sets and the methodology used to identify ARs. First, the ERA-Interim model topography does not accurately represent the complex topography of the western U.S. (cf. Fig. 3.1,b) and the

full range of possible IVT values within each 1.5° x 1.5° grid box. We anticipate that a higher resolution analysis would likely yield more filamentary AR structures (e.g., longer and narrower), possibly with greater inland penetration, but also with more spatial variability and greater fragmentation of the IVT_{250} region due to smaller-scale topographic effects. The current analysis provides a reasonable analysis of the regional characteristics of ARs over the western U.S., but future work may be able to better quantify smaller-scale AR characteristics, such as those influenced by barrier jets that form on the upwind side of major mountains (e.g., Neiman et al. 2010; Hughes et al. 2012; Kingsmill et al. 2013).

Second, the AR characteristics are sensitive to the IVT threshold used. Although it appears that variations in the IVT threshold do not strongly influence the spatial patterns of AR characteristics, they do affect the magnitude (e.g., Fig. 3.5). We also have not used a width criteria, as was done in previous studies (e.g., Ralph et al. 2004; Neiman et al. 2008b; Dettinger et al. 2011; Wick et al. 2013), although our inspection of individual events suggests this has little impact on the results.

Finally, one should consider the method we use to attribute precipitation totals to ARs, which requires that an AR be present at only one analysis time during the 24-h accumulation period. Increasing this threshold reduces the AR and top-decile fractions, but does not strongly affect the resulting geographic patterns (not shown).

Conclusions

This study has examined the climatological characteristics of cool-season (November–April) ARs and their influence on precipitation over the western U.S. AR frequency is largest along the Oregon/Washington coast and decreases southward along

the California coast. Over the interior, AR frequency is strongly influenced by the characteristics (e.g., frequency, intensity, duration, and orientation) of landfalling ARs along the west coast and the subsequent loss of water vapor due to precipitation, especially over higher mountain barriers such as the high Sierra. Hence, AR frequency over the interior is largest over the northwest, particularly over low-elevation corridors that stretch into northwestern Montana and the Snake River Plain. In contrast, the smallest AR frequencies extend from just east of the high Sierra across the central Great Basin into the deep interior. The mean duration of AR conditions follows a spatial pattern similar to that of AR frequency, but is relatively high over the southwest interior.

AR-related cool-season precipitation, as represented by the AR fraction and top-decile fraction, is largest over the northwestern and southwestern U.S. Although ARs are relatively infrequent over the southwest, the fraction of cool-season precipitation and top-decile precipitation events they produce is comparable to that found over the northwest. Thus, the hydroclimate of the southwest is critically dependent on a small number of cool-season AR events. In contrast, the AR-fraction and top-decile fraction are smallest over the Great Basin east of the high Sierra, which act to impede the inland penetration of ARs. The AR fraction and top-decile fraction feature substantial variability within some regions (e.g., northeast Oregon, northern Idaho, northwestern Montana), especially where the topography lacks a sustained high mountain mass and features complex orientations and geometries.

These results improve our understanding of the influence of ARs on the weather and climate of the western U.S. Future work could examine the physical mechanisms that enable or prevent AR penetration into the interior, which could ultimately lead to a

broad conceptual model that differentiates between penetrating and nonpenetrating ARs. An analysis of AR water budgets, particularly as ARs interact with major topographical barriers, could provide additional insight for this model. The results of this work would have a broad range of implications, from short-term forecasting to water management issues in a changing climate.

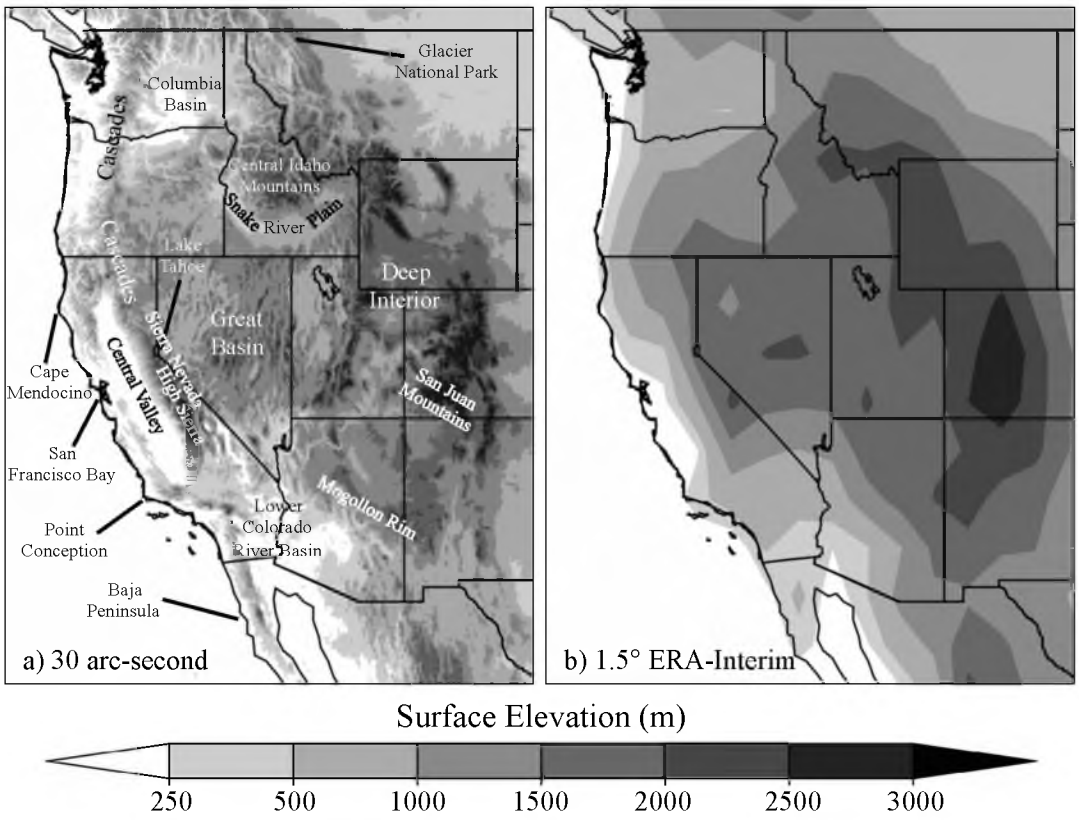

Fig. 3.1: (a) Observed (30 arc second) and (b) ERA-Interim (1.5°) topography (shaded in m) for the western U.S. Geographic terms referenced in text are identified in (a).

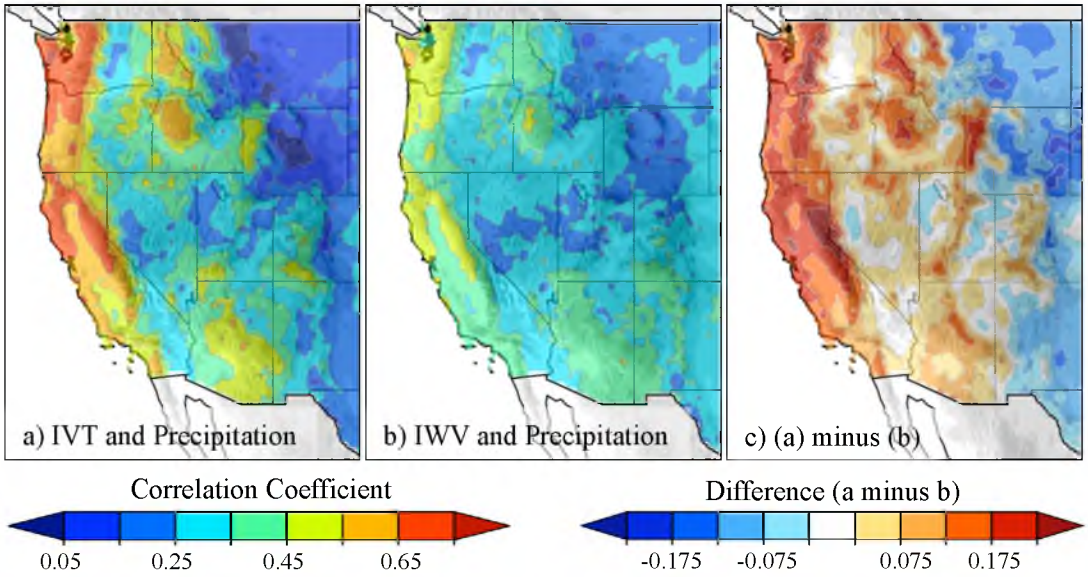

Fig. 3.2: (a) Correlation coefficient between the daily-mean (1200 UTC – 1200 UTC) IVT and 24-h precipitation. (b) Same as (a) except for daily mean IWV. (c) (a) minus (b).

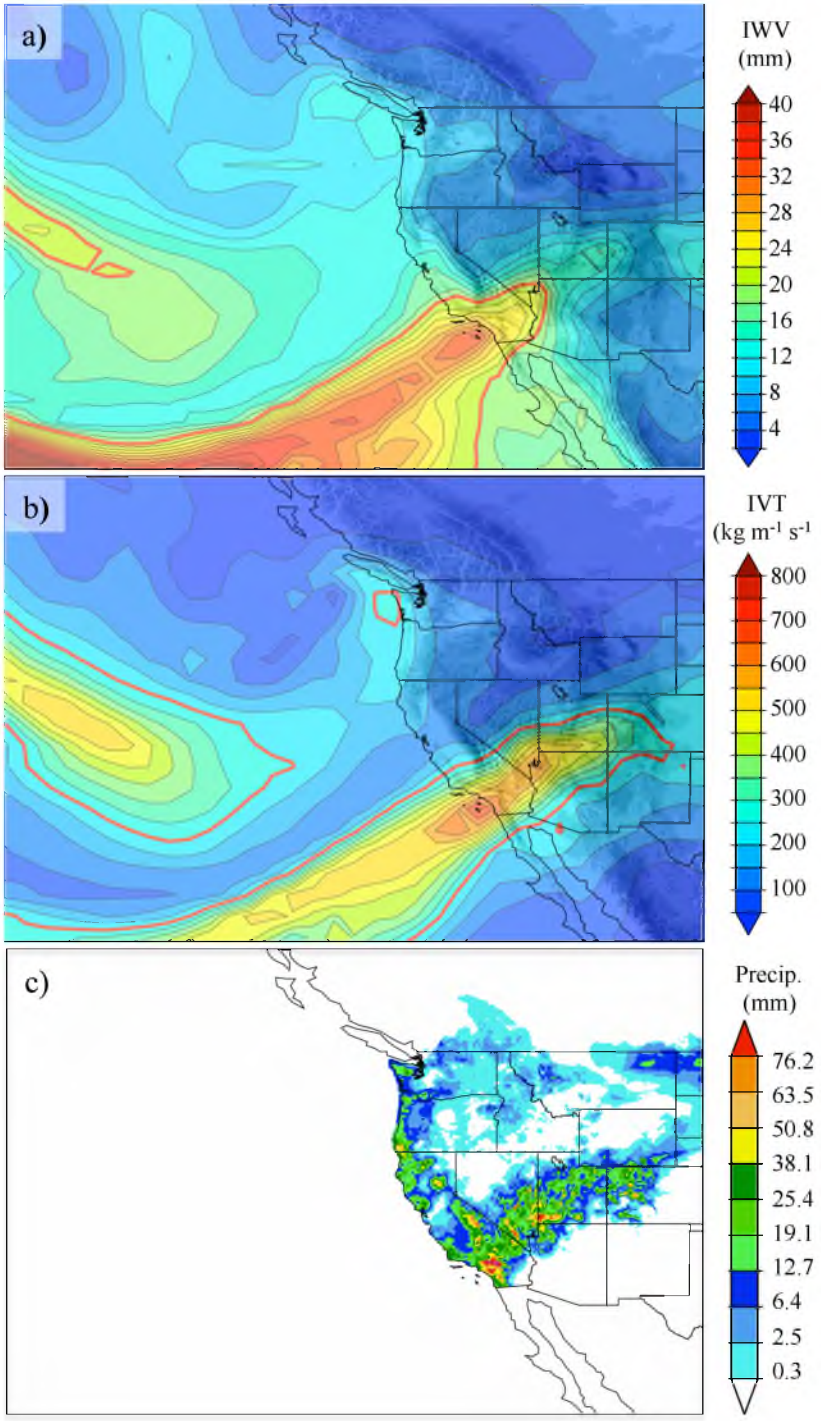

Fig. 3.3: ERA-Interim (a) IWV and (b) IVT at 0000 UTC 21 December 2010. Thick red line in (a) and (b) denote threshold values of 20 mm and 250 kg m^{-1} s^{-1}, respectively. (c) Advanced Hydrological Prediction Services accumulated precipitation analysis for 24-h period ending 1200 UTC 21 December 2010.

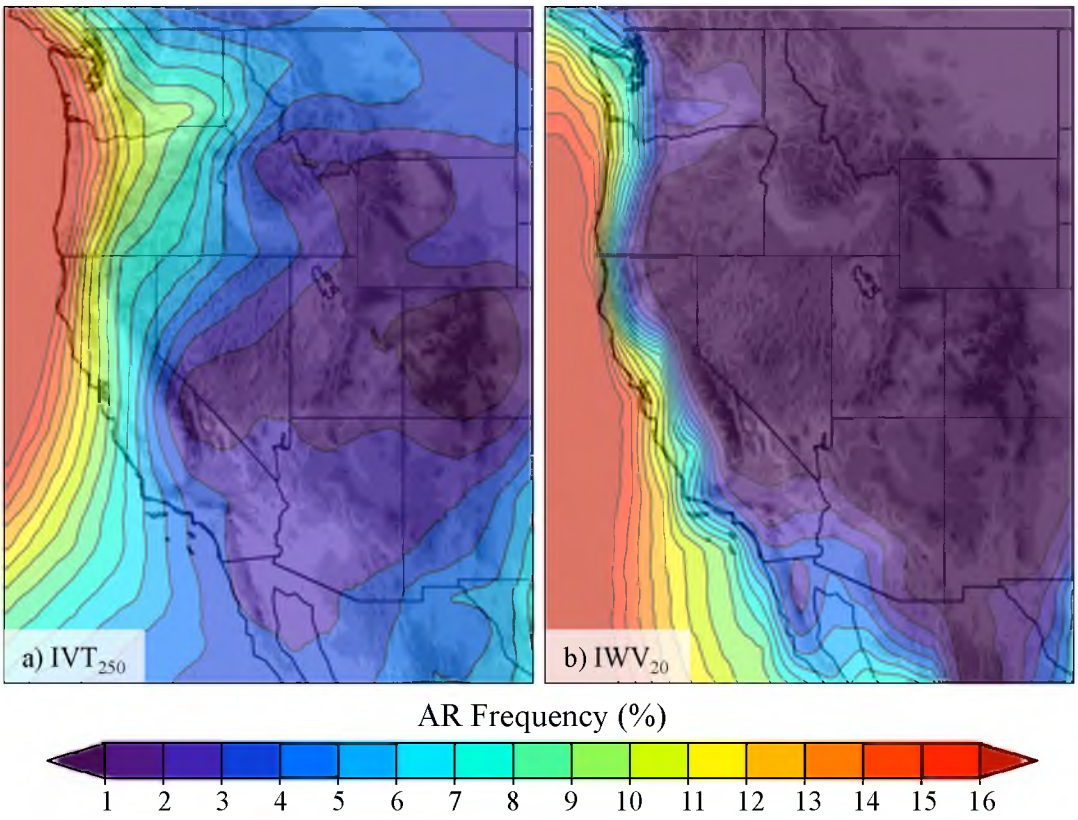

Fig. 3.4: Frequency of ERA-Interim analyses with AR conditions based on (a) IVT_{250} and (b) IWV_{20}.

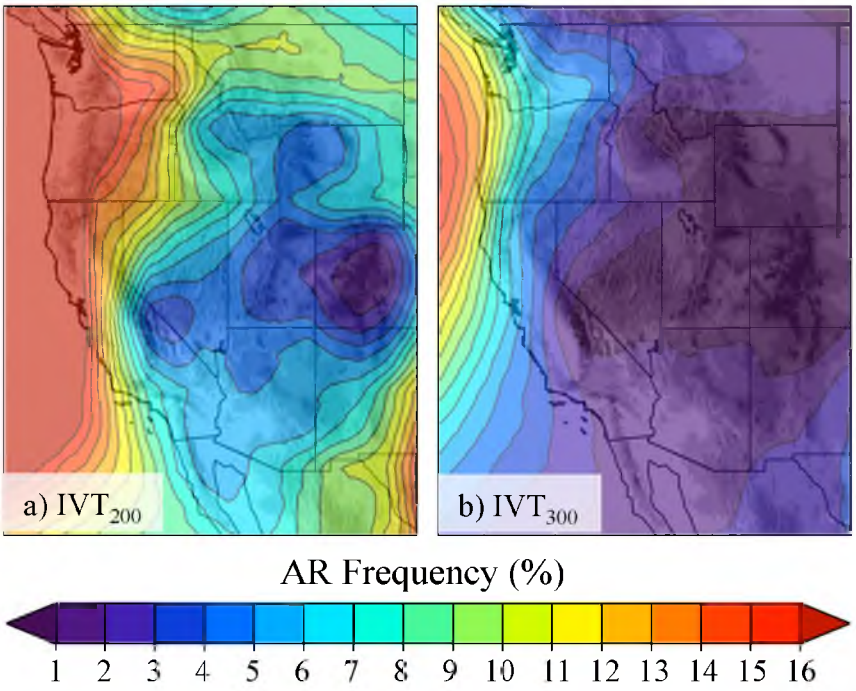

Fig. 3.5: Frequency of ERA-Interim analyses with AR conditions based on (a) IVT_{200} and (b) IVT_{300}.

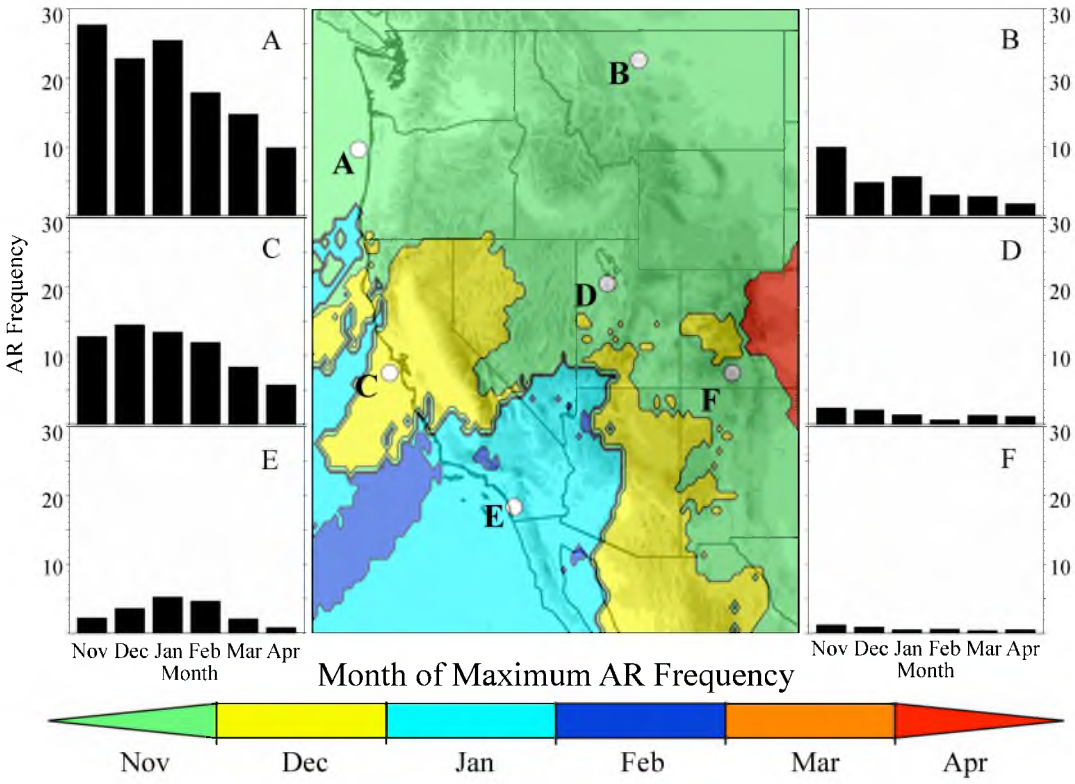

Fig. 3.6: Month of maximum AR frequency based on IVT_{250}. Histograms of IVT_{250} AR frequency by month at selected coastal (left) and interior locations (right).

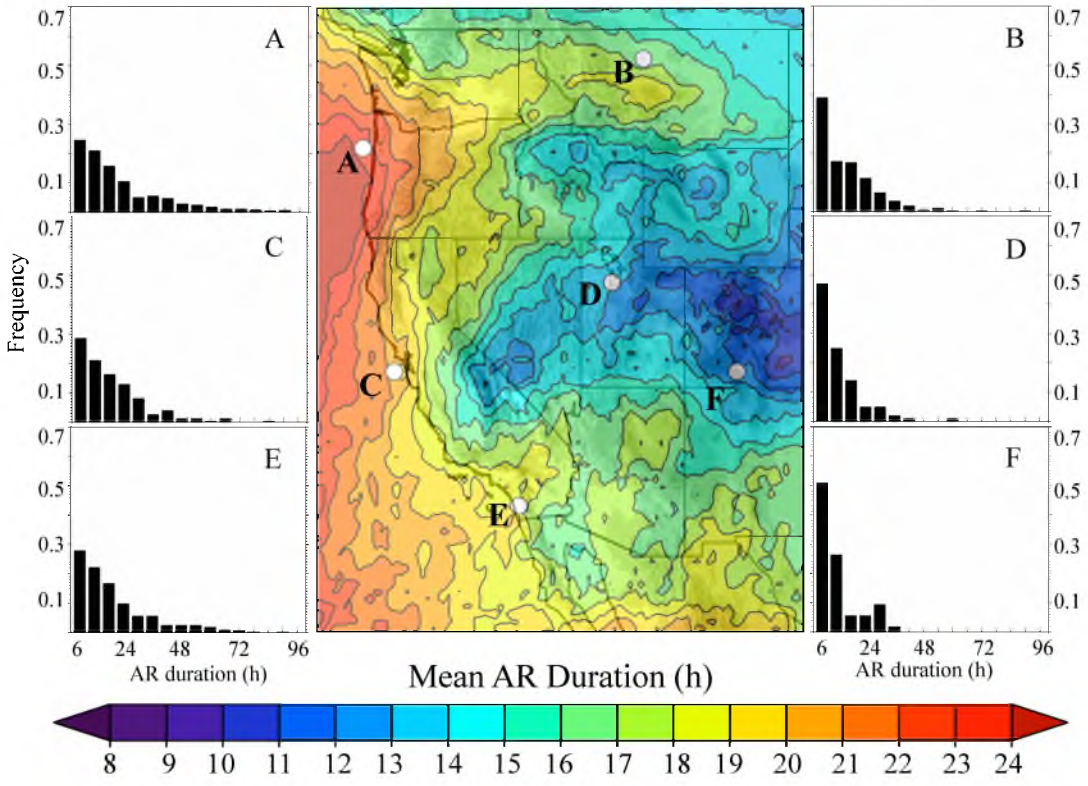

Fig. 3.7: Mean duration (h) of AR conditions based on IVT_{250}. Histograms of IVT_{250} AR duration at selected coastal (left) and interior locations (right).

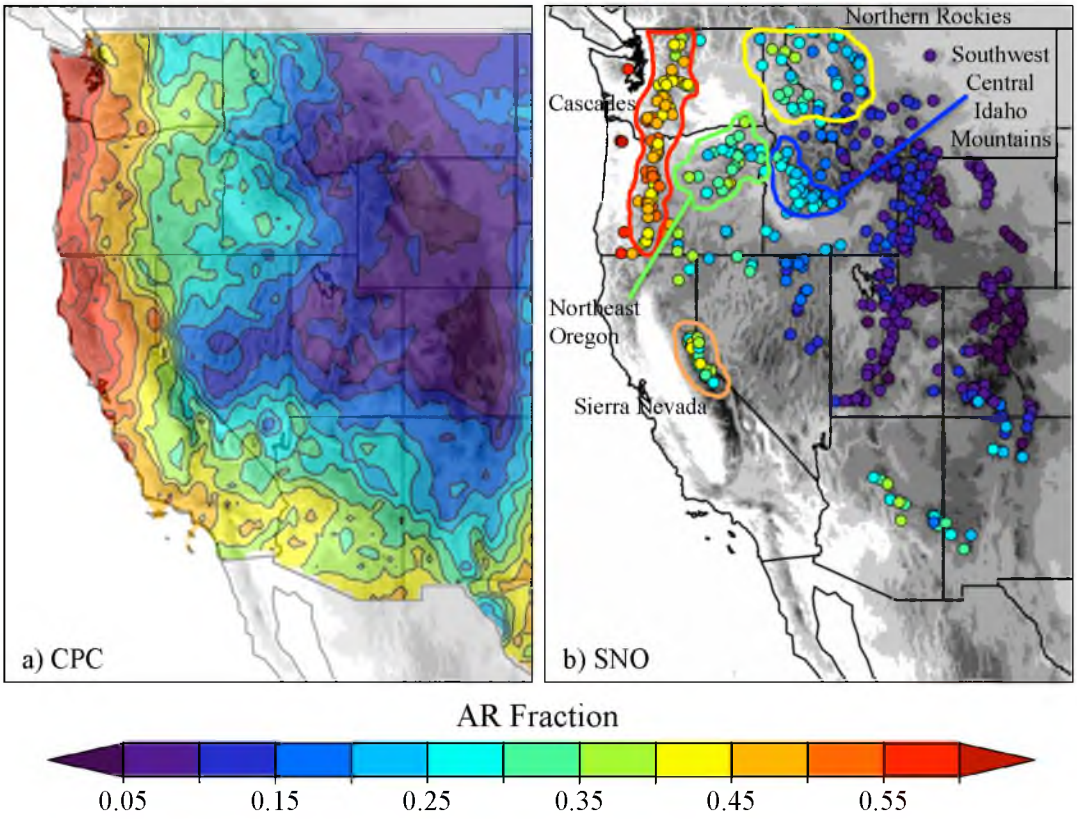

Fig. 3.8: IVT_{250} AR fraction (i.e., the fraction of cool-season precipitation associated with ARs) for (a) the CPC analysis and (b) SNOTEL stations. Selected regions referenced in text highlighted in (b).

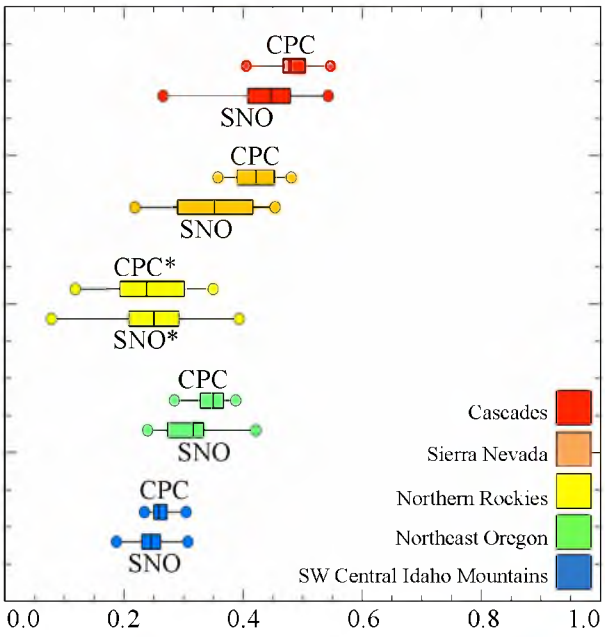

Fig. 3.9: Box and whisker diagram of IVT_{250} AR fraction for each region in Fig. 3.8b based on interpolation of CPC data to SNOTEL locations (CPC) and SNOTEL precipitation observations (SNO). Circles represent the minimum (left) and maximum (right) values. Vertical lines within each box and whisker plot represent the 1st quartile, median, and 3rd quartile. Asterisks denote regions where the difference in median AR fraction between the CPC data and SNOTEL locations is not statistically significant at the 95% confidence level.

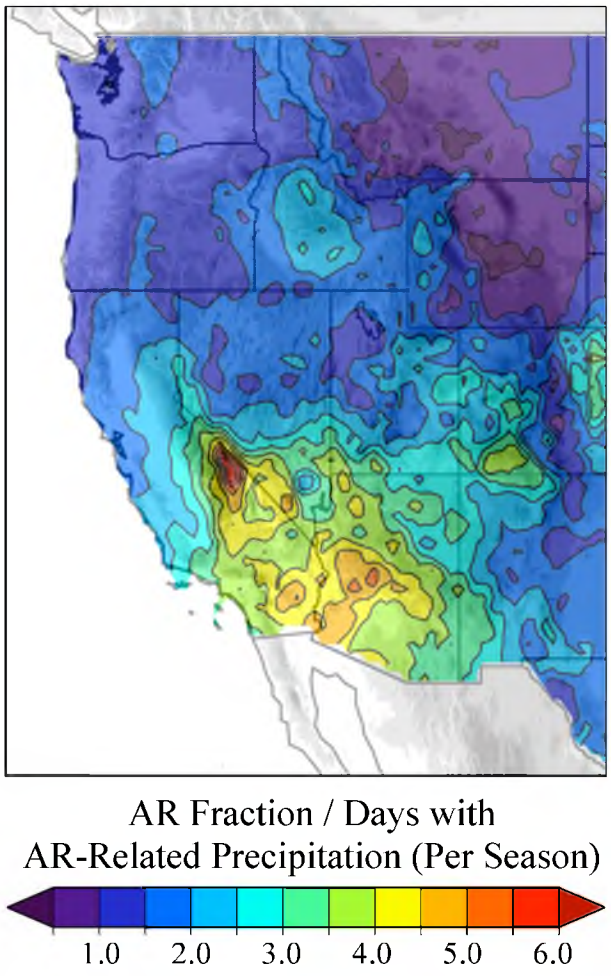

Fig. 3.10: Mean cool-season ratio of IVT_{250} AR fraction (multiplied by 100) to the number of days with AR-related precipitation.

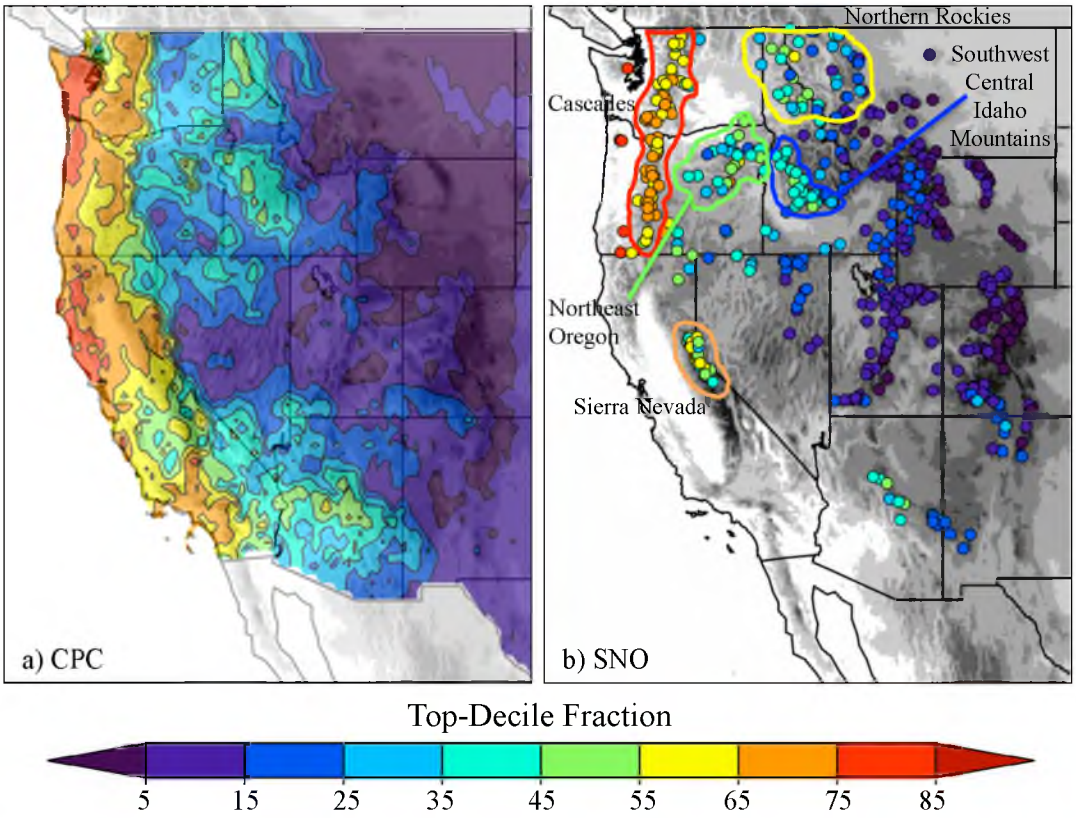

Fig. 3.11: Same as Fig. 3.8 except for top-decile fraction (i.e., the fraction of top-decile 24-h precipitation events associated with ARs).

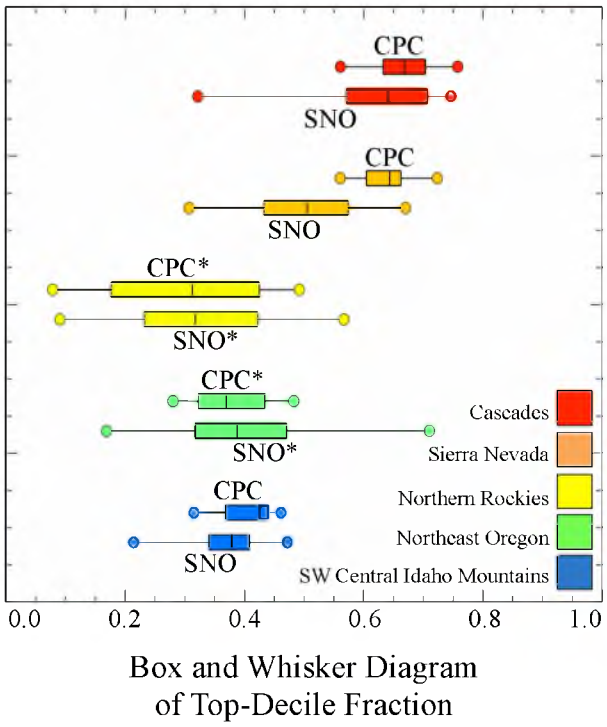

Fig. 3.12: Same as Fig. 3.9 except for top-decile fraction.

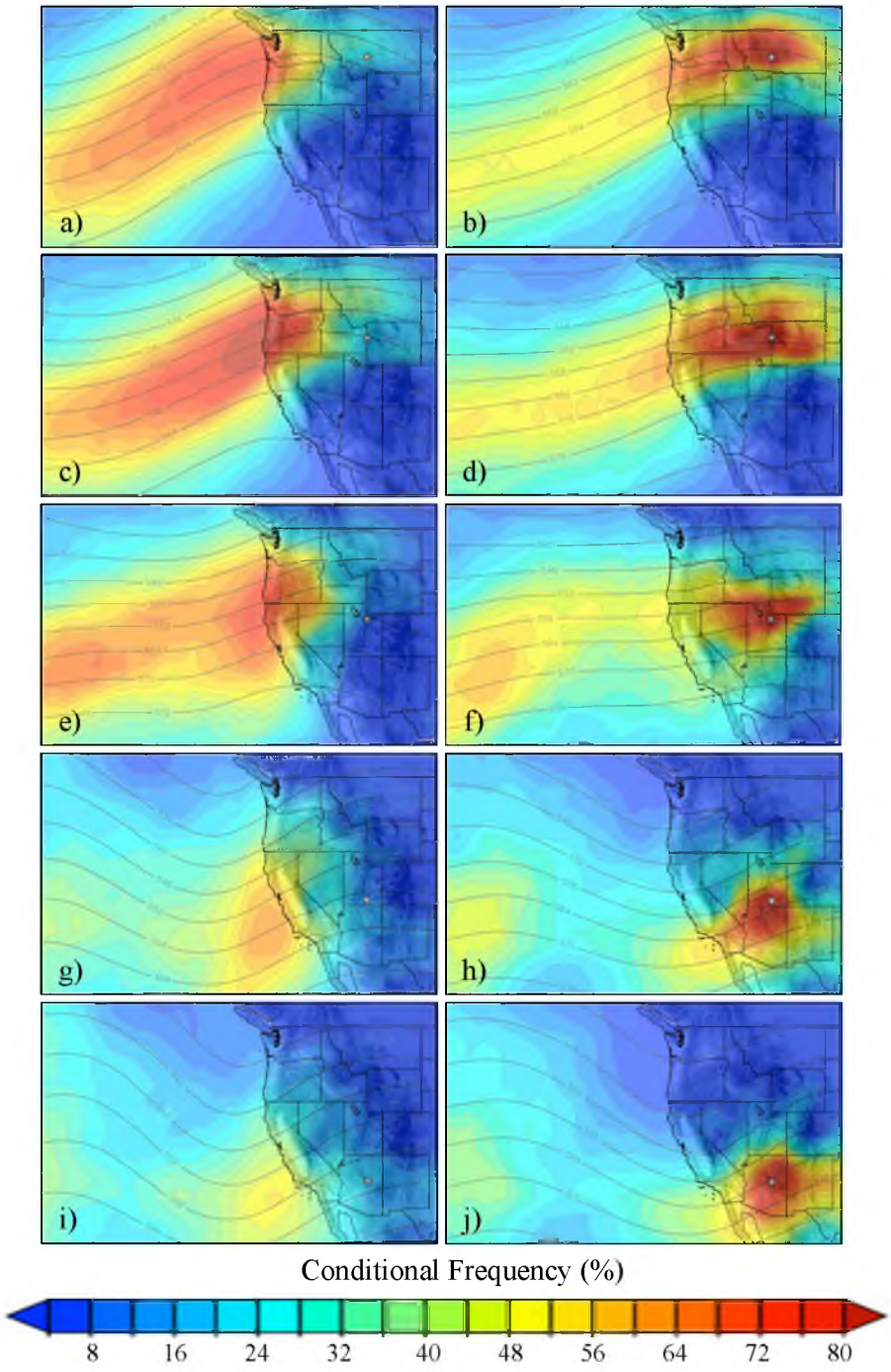

Fig. 3.13: Conditional frequency (shaded) of IVT_{250} AR conditions (left) 24-h prior to and (right) during the existence of AR conditions at selected locations (stars) along the 111° W meridian at (a,b) 46.5° N, (c,d) 43.5° N, (e,f) 40.5° N, (g,h) 37.5° N (i,j) 34.5° N. Contours are composite 500-hPa geopotential height.

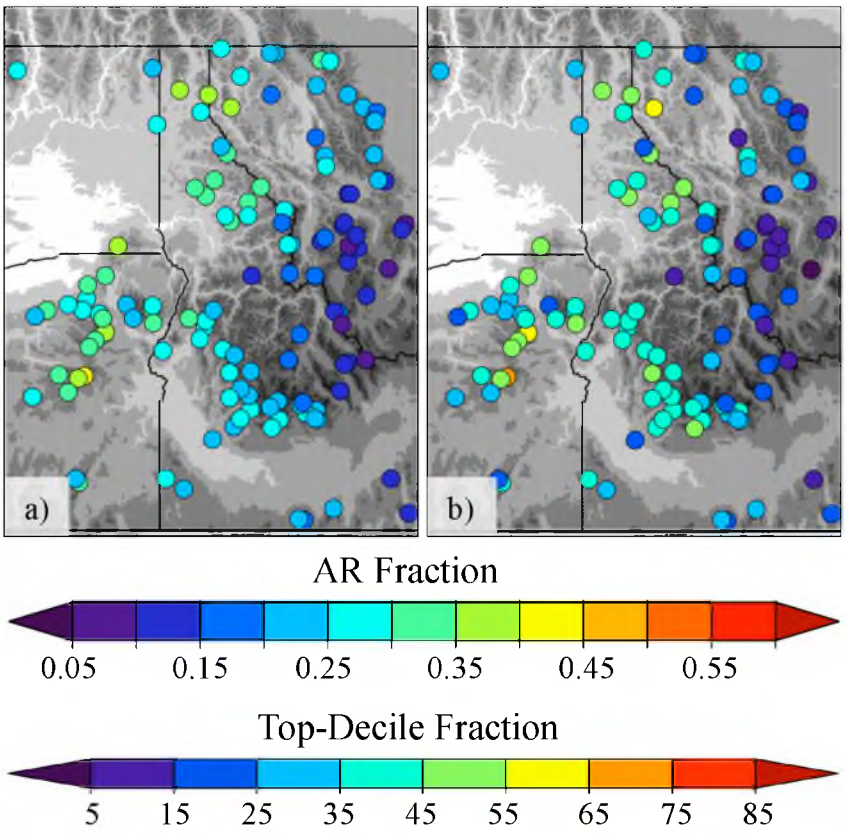

Fig. 3.14: (a) AR fraction and (b) top-decile fraction at SNOTEL stations over the interior northwestern U.S.

CHAPTER 4

MECHANISMS OF ATMOSPHERIC RIVER INLAND PENETRATION OVER THE WESTERN UNITED STATES DEDUCED FROM LAGRANGIAN TRAJECTORY ANALYSIS

Abstract

The interior western U.S. is impacted at times during the cool season (November–April) by high winds, heavy precipitation, and flooding associated with atmospheric rivers (ARs). However, relatively few ARs approaching the U.S. West Coast extend into the interior, and forecasts of high-impact weather over this region would benefit from improved understanding of the mechanisms enabling inland AR penetration.

In this paper, we initiate 72-h forward trajectories at 950 hPa within cool-season ARs as they approach the west coast of North America. These trajectories are then classified as coastal-decaying, inland-penetrating, or interior-penetrating based on whether they remain within an AR upon reaching selected transects over the western U.S. At initiation, interior-penetrating AR trajectories are associated with a more amplified trough-ridge pattern over the northeastern Pacific and western U.S., more southwesterly (vs. westerly) flow, and larger water vapor transport ($\boldsymbol{qu}$), particularly west of the Sierra Nevada. Such interior-penetrating AR trajectories most frequently originate along the Oregon coast, but the greatest fraction of trajectories that eventually penetrate into the interior is found along the Baja Peninsula.

Inland- and interior-penetrating AR trajectories maintain large $q\boldsymbol{u}$ by experiencing increases in wind speed ($\boldsymbol{u}$) that offset decreases in specific humidity (q), particularly in the vicinity of high topographical barriers. Despite experiencing similar decreases in q, coastal-decaying AR trajectories do not experience increases in $\boldsymbol{u}$, and $q\boldsymbol{u}$ decreases more rapidly. Therefore, synoptic conditions favoring larger initial $q\boldsymbol{u}$ and increases in $\boldsymbol{u}$ over the interior are two keys to differentiating between interior-penetrating and coastal-decaying AR trajectories.

Introduction

Atmospheric rivers (AR) are long and narrow regions of intense vertically integrated water vapor transport (IVT; Newell et al. 1992; Newell and Zhu 1994; Zhu and Newell 1998). Hydrometeorological extremes over the western United States (U.S.) often result from persistent AR conditions, especially when ARs intersect topographical barriers and produce strong upslope flow (Neiman et al. 2002; Ralph et al. 2004; Ralph et al. 2013). During the cool season (November–April), these conditions are common along the U.S. west coast, where many cases of heavy AR-related rainfall and flooding have been documented (Ralph et al. 2006; Neiman et al. 2008; Ralph et al. 2011). The penetration of ARs into the interior western U.S. is less frequent, but can likewise produce heavy precipitation (Rigby 1998; Bernhardt 2006; Neiman et al. 2013; Rutz et al. 2014).

Recent studies have attempted to quantify the fraction of precipitation attributable to ARs over the interior western U.S. To facilitate this, some authors have identified ARs following Ralph et al. (2004) as contiguous regions $\geq$ 2000 km in length and $\leq$ 1000 km in width, with integrated water vapor (IWV) $\geq$ 20 mm. Dettinger et al. (2011) used this

method to construct an 11-year climatology of ARs and found that 20–50% of total cool-season precipitation at most sites in California, Oregon, and Washington fell on the day of or day after an AR landfall along the west coast of North America from 32.5°–52.5°N. Further inland, lower fractions of cool-season precipitation were attributed to ARs, particularly over the southwestern U.S. (< 15%), although Rutz and Steenburgh (2012) found higher fractions (15–40%) over the southwest by extending the analysis to include ARs present along the Baja Peninsula (24°–32.5°N).

Rutz et al. (2014) showed that over much of the western U.S., IVT is more useful than IWV for exploring the relationship between cool-season ARs and precipitation, and objectively identified ARs as contiguous regions ≥ 2000 km in length with IVT ≥ 250 kg m^{-1} s^{-1}. Using this approach, the AR frequency (i.e., the percent of ERA-Interim reanalyses with an AR present) is largest (> 16%) along the Oregon and Washington coasts and decreases rapidly southward along the California coast and eastward over the Pacific Ranges. Over the interior, the AR frequency is largest over the northwest, whereas it is smallest (< 3%) from the southwestern U.S. northeastward into Colorado and Wyoming. The mean duration of ARs follows a similar pattern, but with a prominent local maximum (> 18 h) extending along a relatively low-elevation corridor from the Columbia Basin into northwestern Montana, and a prominent local minimum (< 12 h) extending from east of the high Sierra northeastward over the Great Basin. Rutz et al. (2014) also found that the fraction of top-decile 24-h precipitation events (top-decile fraction) attributable to ARs is greatest (> 0.55) along the U.S. west coast, particularly north of San Francisco, and smallest (< 0.15) over the central and eastern Great Basin, and over most of Utah, Colorado, Wyoming, and Montana. Over the northwest and

southwest interior, the top-decile fraction ranges from 0.15–0.55 and exhibits large mesoscale variability.

The relationship between ARs and precipitation can also be examined using atmospheric trajectories. Stohl et al. (2008) showed that heavy precipitation along the Norwegian coast is often associated with trajectories that pass through ARs. The specific humidity of these trajectories typically increases over a broad swath of the Atlantic Ocean. More generally, interactions between the development and decay of (sometimes tropical) cyclones and ARs strongly influences water vapor fluxes into ARs, which can act to offset losses due to precipitation (Sodemann and Stohl, 2013; Cordeira et al., 2013). Knippertz and Wernli (2010) developed a method to identify northern hemispheric trajectories originating in the tropics (south of 20°N) and obtaining water vapor flux $\geq$ 100 g kg^{-1} m s^{-1} somewhere north of 35°N, referring to these as tropical moisture export (TME) trajectories. This method was later generalized to include the southern hemisphere by Knippertz et al. (2013), who also showed that outbreaks of TME trajectories over the northeastern Pacific were strongly related to the ARs identified by Dettinger et al. (2011) along the U.S. west coast.

In this study, we initiate 72-h forward trajectories at 950 hPa within ARs approaching the North American west coast (24°–52.5°N) to explore the processes contributing to AR maintenance or decay over western North America. Of particular interest is identifying the factors that differentiate coastal-decaying ARs from those that penetrate into the western U.S interior. Because ARs can produce heavy precipitation, the results have broad applications in weather, hydrologic, and climate research and forecasting. Section 4.2 describes the data and methods used, with section 4.3 providing

an overview of the trajectory pathways. Section 4.4 presents the initial characteristics of trajectories approaching the coast and is followed in section 4.5 by an analysis of changes in these characteristics as the trajectories move inland. We then use composites to explore contrasts in the synoptic environment of coastal-decaying, inland-, and interior-penetrating trajectories from selected locations. Finally, conclusions and future work are summarized in section 4.7.

Data and Methods

Trajectories are calculated using data from the ERA-Interim reanalysis (Dee et al. 2011), which is based on a version of the European Centre for Medium-Range Weather Forecasts (ECMWF) Integrated Forecast System (IFS) with 60 vertical levels (extending to 0.1 hPa), T255 triangular truncation for dynamical fields, and a reduced Gaussian grid with ~80-km spacing for surface and other grid point fields (Simmons et al. 2007; Uppala et al. 2008; Berrisford et al. 2009). The ~80-km Gaussian grid spacing provides a reasonable estimate of the effective grid spacing of the ERA-Interim in physical space (Kanamitsu 1989). All data are obtained from the ECMWF data server on a 1.5° latitude × 1.5° longitude grid with 6-h temporal resolution and then interpolated to a 1-h resolution prior to trajectory calculations.

At each 6-h ERA-Interim analysis time during the cool-season months (November–April), from November 1988 to April 2011, trajectories are released from 950 hPa whenever an AR is present at a grid point along a transect, T_1, which lies ~100–200 km west of the North American west coast (Fig. 4.1). ARs are identified following Rutz et al. (2014) as contiguous regions with length $\geq$ 2000 km and vertically integrated water vapor transport (IVT) $\geq$ 250 kg m^{-1} s^{-1}. The 950-hPa level is, on average, at or near

the level of maximum mean water vapor flux when ARs are identified at T_1 grid points, except those upstream of the southern Baja Peninsula (Fig. 4.2). The 72-h forward trajectories are calculated at a 1-h temporal resolution using the zonal, meridional, and vertical wind (u, v, and w, respectively), with trilinear interpolation used to obtain values of atmospheric data at the trajectory location.

We then classify these AR trajectories based on their pathways and characteristics if and when they reach two selected transects over the interior western U.S. The first, T_2, lies immediately east of the Pacific Ranges (see Fig. 4.1 for description), which typically represent the first major topographic barriers encountered by landfalling AR trajectories (Fig. 4.1). The second, T_3, lies roughly along the second major topographical barrier potentially encountered by these trajectories.

Trajectories that do not reach T_2 during their 72-h integration period are removed from the analysis. Trajectories that reach T_2 are divided into three subsets. Those not within an AR upon reaching T_2 are classified as *coastal-decaying AR trajectories*. Those that reach T_2 but not T_3 within an AR are classified as *inland-penetrating AR trajectories*. Those that reach T_3 within an AR are classified as *interior-penetrating AR trajectories*.

Spatial analyses of mean trajectory characteristics are created by defining a 1.0° latitude × 1.0° longitude grid over the western U.S. and Canada. At each 1-h time step, we record the characteristics of each trajectory, which is then used to calculate the mean within each grid box. If a trajectory resides within one grid box for more than one time step, an average of its characteristics over all steps within that grid cell is taken and recorded as one value. This prevents overall statistics from being skewed by slow-moving trajectories.

Trajectory Pathways and Displacements

Coastal-decaying AR trajectories are widely distributed over the western U.S. and southwestern Canada, and are characterized by rapidly decreasing water vapor flux ($\boldsymbol{qu}$) upstream and over the Pacific Ranges (Fig. 4.3a). The greatest concentration of such trajectories (i.e., the number passing through a given 1.0° × 1.0° grid cell) extends from the Pacific coast into the interior northwestern U.S. and southwestern Canada (Fig. 4.3d). The trajectory concentration decreases toward the south, and is smallest over the southwestern U.S.

The distribution of inland-penetrating AR trajectories more strongly reflects the topographic influences of the Pacific Ranges, as these must generally maintain large $\boldsymbol{qu}$ until reaching T_2 (Fig. 4.3b,e). The concentration of these trajectories is largest along a corridor extending from Oregon and Washington coast across the Columbia River Basin and along the U.S.–Canada border. A secondary maximum extends from the Baja Peninsula into the southwestern U.S. In contrast, very few inland-penetrating AR trajectories are found over and immediately downstream of the high Sierra, which contribute strongly to AR decay (Rutz et al. 2014). A secondary minimum lies over and downstream of Vancouver Island and the high terrain of the central Coast Mountains of southwestern Canada.

Similar to inland-penetrating AR trajectories, the distribution of interior-penetrating AR trajectories reflects the topographic influences of the Pacific Ranges, but also the rugged interior of the western U.S. and Canada, as these must typically maintain large $\boldsymbol{qu}$ until reaching T_3 (Fig. 4.3c,f).

The distribution of trajectories highlights three distinct pathways along which

inland- and interior-penetrating trajectories remain AR-related (Fig. 4.3e,f). The first pathway extends from the Oregon and Washington coasts, across the Columbia River Basin, over the various mountain ranges near and along the U.S.–Canada border, and into the northern Great Plains. The second pathway lies north of the highest portion of the Coast Mountains of southwestern Canada and extends through the relatively low gap north of the Columbia Mountains and Canadian Rockies. The third pathway extends from the Baja Peninsula into the southwestern U.S. Overall, these results are in good agreement with those of Rutz et al. (2014), who identified two preferred pathways of AR penetration into the interior western U.S., located north and south of the high Sierra (their analysis did not extend into southwestern Canada).

AR trajectories generally move in a broad, anticyclonic pattern over the northwestern U.S., with small northward displacements (2–4°) from their original latitude (ϕ) as they move inland, and a tendency to begin returning south between ~110–120° W (Fig. 4.4). However, over the southwestern U.S., AR trajectories initiated west of southern California and the Baja Peninsula generally move in a more cyclonic pattern, with inland- and interior-penetrating AR trajectories featuring large northward displacements (> 6°) over the Colorado Plateau and adjoining Rocky Mountain region (cf. Figs. 4.3 and 4.4).

Most trajectories experience a decrease in pressure (p, i.e., increases in the altitude) as they move inland, particularly over topographical barriers (Fig. 4.5). For coastal-decaying AR trajectories, these decreases are largest over the Coast Mountains of southwestern Canada and the northwestern U.S., including northern California (Fig. 4.5d). For inland- and interior-penetrating AR trajectories, northern Idaho, central

Arizona, and southwestern Colorado are also characterized by large decreases in p (Fig. 4.5e,f). Most of these regions are located over and upstream, or in the vicinity, of major topographical barriers. Increases in p are found in the lee of the Rocky Mountains, and particularly in the lee of the Canadian Rockies.

Trajectory Characteristics at Initiation

The number of AR-related trajectories initiated along T_1 that reach T_2 features a maximum (~2000) west of Oregon (points 6–8), decreases rapidly to the north and south, and exhibits a long tail to lower values along the Baja Peninsula (Fig. 4.6). The number of these trajectories that can ultimately be classified as inland- or interior-penetrating (the latter represents a subset of the former) is largest (~300) along the coasts of southern Oregon and northern California (points 7–10) and also decreases to the north and south. However, the percentage of AR-related trajectories that remain within an AR at T_2 and T_3 is highest along the coasts of southern California and the Baja Peninsula (points 14–20). Thus, although the number of inland- and interior-penetrating AR trajectories is highest along the coasts of southern Oregon and northern California, trajectories associated with ARs approaching the coasts of southern California and the Baja Peninsula are more likely to maintain AR characteristics as they penetrate inland.

A local minimum in the number and percentage of inland- and interior-penetrating trajectories is found along T_1 near points 10-13. These points are located west and southwest of the high Sierra, which appear to strongly contribute to AR decay (see also Rutz et al. 2014).

An important difference between coastal-decaying and interior-penetrating AR trajectories is found in the initial magnitude of water vapor flux at T_1 grid points (i.e., the

intensity of the AR near landfall). The median (and general distribution of) $q\boldsymbol{u}$ of interior-penetrating trajectories is larger than that of coastal-decaying trajectories at all points except 18–20 (Fig. 4.7a), and this is particularly true west of the high Sierra, at points 11 and 12, where the fraction of interior-penetrating AR trajectories is smallest. Hence, trajectories initiated at these points must typically have large $q\boldsymbol{u}$ if they are to remain AR-related at T_3, and very few trajectories accomplish this. The median $q\boldsymbol{u}$ of inland-penetrating AR trajectories typically lies between those of coastal-decaying and interior-penetrating AR trajectories, and results for this classification are not presented here.

Breaking ($q\boldsymbol{u}$) into its constituent parts, specific humidity (q) and wind ($\boldsymbol{u}$), we find that the larger initial $q\boldsymbol{u}$ of interior-penetrating AR trajectories at points 1–17 is primarily due to larger initial q, whereas their median $\boldsymbol{u}$ is often only slightly larger or even smaller than that of coastal-decaying AR trajectories (cf. Fig. 4.7b,c). Whereas the interquartile range of q is consistently larger for interior-penetrating AR trajectories at all points 1–17, only west of the high Sierra, at points 11 and 12, is the interquartile range of $\boldsymbol{u}$ noticeably larger than that for coastal-decaying AR trajectories. Hence, while most trajectories initiated at these points must typically have large q if they are to remain AR-related at T_3, those initiated at points 11 and 12 must also typically have large $\boldsymbol{u}$.

At points 17–20, differences in the distributions of $q\boldsymbol{u}$, q, and $\boldsymbol{u}$ between coastal-decaying and interior-penetrating AR trajectories are relatively small. This is likely related to the fact that 950 hPa represents a local minimum in cool-season water vapor flux during ARs at these locations (Fig. 4.2). While we have focused here on the fate of 950 hPa trajectories, those initiated closer to the maximum flux (~700 hPa) for these points likely evolve differently.

Changes in Water Vapor Flux, Specific Humidity, and Wind

The water vapor flux ($\boldsymbol{qu}$) of interior-penetrating AR trajectories is larger than that of coastal-decaying AR trajectories not only as they approach the coast (along T_1, as shown in Fig. 4.8a), but also over the interior (Figs. 4.8a–c). The magnitude of $\boldsymbol{qu}$ generally decreases from west to east over the interior, with a tendency for larger values over lower elevations, such as the Gulf of California, the Lower Colorado River Valley, and the corridor extending from the Columbia Basin toward Glacier National Park. In contrast, smaller values of $\boldsymbol{qu}$ are found over and downstream of major topographical barriers such as the high Sierra and Colorado Rocky Mountains.

The specific humidity (q) of AR trajectories is generally largest west of the Pacific Ranges and Mogollon Rim, decreases from west to east over the interior, and is smallest over and east of the Rocky Mountains (Figs. 4.8d–f). Over the interior, the q of interior-penetrating AR trajectories is ~1 g kg^{-1} larger than that of inland-penetrating AR trajectories and ~2 g kg^{-1} larger than that of coastal-decaying AR trajectories, with some regional variation (cf. Figs. 4.8d–f).

We can further analyze changes in q along these trajectories by calculating the drying ratio (DR) defined by Smith et al. (2005) as:

$$DR = \frac{\text{water vapor removed}}{\text{initial water vapor}} \times 100\%. \qquad (3)$$

Specifically, we calculate the 1-h mean drying ratio (DR_{1h}) at a given time step t as:

$$DR_{1h} = \frac{q_{t-1} - q_{t+1}}{2 \times q_{t-1}} \times 100\%, \qquad (4)$$

where q_{t-1} and q_{t+1} are the specific humidity at the previous and next time steps, respectively. Similarly, the total drying ratio (integrated over time from trajectory initiation to time step t, DR_{tot}) is calculated as:

$$DR_{tot} \text{ at } t = \frac{q_0 - q_t}{q_0} \times 100\%, \qquad (5)$$

where q_0 is the specific humidity at trajectory initiation.

For coastal-decaying AR trajectories, the DR_{1h} is largest (> 8% h^{-1}) over southern Vancouver Island and the adjoining Strait of Georgia, northern California, and the Sierra Nevada (Fig. 4.9a). For inland- and interior-penetrating trajectories, the DR_{1h} is largest (> 8% h^{-1}) over these same regions, but also over the Mogollon Rim, the San Juan Mountains, and northwestern Colorado (Figs. 4.9b,c). Differences in DR_{1h} among the three classifications are minimal over and west of the Pacific Ranges. Over the Sierra Nevada, the large DR_{1h} of coastal-decaying AR trajectories highlights the frequent decay of ARs over this range. Not surprisingly, the spatial distribution of the DR_{1h} is very similar to that of changes in q, although the DR_{1h} is relatively higher over northern and interior locations where q is initially more limited.

The DR_{tot} shows the fraction by which q has been reduced since trajectory initiation at T_1 (Fig. 4.9d–f). Similar to changes in q, the DR_{tot} decreases from the coast to the interior, and does so more rapidly more coastal-decaying AR trajectories. *Interior-*

penetrating AR trajectories generally have the smallest DR_{tot}. Previous work by Smith et al. (2005) and Didlake (2007) found drying ratios of 32% and 43% for air masses crossing northern California (including both the Coastal Ranges and Sierra Nevada) and the Oregon Cascades, respectively. We find a slightly higher ratio (~40–45%) east of these ranges for coastal-decaying AR trajectories and a lower ratio (~30–35%) for inland- and interior-penetrating AR trajectories, but considering that the former comprises the majority of events, our findings are in close agreement.

The wind speed ($\boldsymbol{u}$) of AR trajectories is generally largest east of the Pacific Ranges, and over the northern half of the interior, although interior-penetrating AR trajectories also have large $\boldsymbol{u}$ over the Colorado Plateau (Figs. 4.8g–i). The $\boldsymbol{u}$ of interior-penetrating AR trajectories is larger than that of coastal-decaying AR trajectories, with that of inland-penetrating trajectories falling in the middle (cf. Figs. 4.8g–i).

The change in water vapor flux, $D(q\boldsymbol{u})/Dt$, is most negative near the coasts of Washington and British Columbia, with a minimum (< -25 g kg^{-1} m s^{-1} h^{-1} for interior-penetrating AR trajectories) over and west of the Olympic Peninsula and southern Vancouver Island (Figs. 4.10a–c). Inland- and interior-penetrating AR trajectories also feature substantially negative $D(q\boldsymbol{u})/Dt$ (< -10 g kg^{-1} m s^{-1} h^{-1}) over eastern Oregon, southern Arizona, and for the latter, over the Colorado Plateau. Based on the trajectory paths evident in Figs. 4.3a–c, all of these areas typically lie upstream of high topographical barriers. Positive values of $D(q\boldsymbol{u})/Dt > 5$ g kg^{-1} m s^{-1} h^{-1} are found over and downstream of the northern Sierra Nevada in association with interior-penetrating AR trajectories.

The change in specific humidity, $D(q)/Dt$, is substantially negative (< -0.4 g kg^{-1}

h^{-1}) over and west of the Pacific Ranges, with minima (< -1.0 g kg^{-1} h^{-1} for interior-penetrating AR trajectories) over southern Vancouver Island, the adjoining Strait of Georgia, northern California, and the Mogollon Rim (Figs. 4.10d–f). $D(q)/Dt$ is also < -0.4 g kg^{-1} h^{-1} for inland- and interior-penetrating AR trajectories over northern Idaho, and for the latter, over the Colorado Plateau. Most of these areas lie over and upstream of high topographical barriers, although decreases in q over northern California may be more nuanced. A low-level jet often develops quasi-parallel to the Sierra Nevada as ARs approach the coast, and can act to redistribute water vapor and precipitation toward the northern end of California's Central Valley (Reeves et al. 2008; Smith et al. 2010). These studies point to the southern Cascades and northern Sierra as the primary benefactors, but given the 1.5° reanalysis, it is not surprising to find a general minimum located in the center of northern California's complex topography.

The change in wind speed, $D(\boldsymbol{u})/Dt$, is largest over and upstream of the northern Sierra Nevada, exceeding 5 m s^{-1} h^{-1} for interior-penetrating AR trajectories (Fig. 4.10g–i). For these trajectories, $D(\boldsymbol{u})/Dt$ also exceeds 3 m s^{-1} h^{-1} over the Canadian Coast Mountains, northern Idaho, the Mogollon Rim, and along the eastern edge of the Snake River Plain, whereas coastal-decaying AR trajectories do not exceed this value anywhere. $D(\boldsymbol{u})/Dt$ is negative over and west of the Olympic Peninsula, over eastern Oregon, and for inland- and interior-penetrating AR trajectories, downstream of the Canadian Rocky Mountains. $D(\boldsymbol{u})/Dt$ is generally largest over and/or downstream of topographical barriers and decreases in pressure. Hence, increases in $\boldsymbol{u}$ are nearly co-located with, but shifted slightly downstream of, decreases in q (cf. Figs. 4.10d–f, g–i).

Having examined spatial analyses of $q\boldsymbol{u}$, q, $\boldsymbol{u}$, and changes in these variables, we

gain additional insight into the factors contributing to changes in $q\boldsymbol{u}$ by examining both components of the derivative:

$$\frac{D(q\boldsymbol{u})}{Dt} = q\frac{D\boldsymbol{u}}{Dt} + \boldsymbol{u}\frac{Dq}{Dt} \qquad (6)$$

The first and second terms on the right hand side of (6) represent dynamic and thermodynamic contributors, respectively, to changes in $q\boldsymbol{u}$ (Seager et al. 2010).

Large negative thermodynamic contributions to changes in $q\boldsymbol{u}$ are nearly co-located with decreases in both p and q (cf. Figs. 4.5d–f, 4.9d–f, and 4.11a–c). In contrast, large positive dynamic contributions to changes in $q\boldsymbol{u}$ are nearly co-located with increases in $\boldsymbol{u}$, which are often found over and slightly downstream of decreases in p and q (cf. Figs. 4.10g–i and 4.11d–f). This pattern arises because as trajectories approach topographic barriers and begin rising, q is depleted due to precipitation and $\boldsymbol{u}$ increases (typically) with height.

Summarizing this and earlier analyses from this section, regions characterized by decreases in q are often the same as those characterized by increases in $\mathbf{u}$, with the result that $q\boldsymbol{u}$ changes little over these areas. For example, this explains why the magnitude of $D(q\boldsymbol{u})/Dt$ for interior-penetrating AR trajectories over the Mogollon Rim is small (and also insignificant at the 95% confidence level following Student's t-test), despite the magnitudes of $D(q)/Dt$ and $D(\boldsymbol{u})/Dt$ being large and of opposite sign over this region (cf. Figs. 4.10c,f,i). However, those regions where increases in $\boldsymbol{u}$ do not offset decreases in q are typically characterized by decreases in $q\boldsymbol{u}$. Examples can be found over and west of the Olympic Peninsula ($D(q)/Dt < 0$, $D(\boldsymbol{u})/Dt < 0$), over eastern Oregon ($D(q)/Dt \sim 0$,

$D(\boldsymbol{u})/Dt < 0$), and over the Colorado Plateau ($D(q)/Dt < 0$, $D(\boldsymbol{u})/Dt \sim 0$). Hence, for those AR-related trajectories that do penetrate inland and/or into the interior, large water vapor fluxes are increasingly maintained by stronger winds, even as water vapor is rapidly depleted in the vicinity of topographical barriers.

The total change (integrated over time since trajectory initiation) in $q\boldsymbol{u}$, $D(q\boldsymbol{u})$, becomes more negative from the coast to the interior, and generally does so most rapidly for coastal-decaying AR trajectories (Fig. 4.12a–c). An exception is found over the Coast Mountains east of Vancouver Island, where interior-penetrating AR trajectories have already lost, on average, > 60 g kg^{-1} m s^{-1}, and a corridor of very negative (< –80 g kg^{-1} m s^{-1}) $D(q\boldsymbol{u})$ extends east of here across southern British Columbia. Generally, $D(q\boldsymbol{u})$ decreases more rapidly over and downstream regions where $D(q\boldsymbol{u})/Dt$ is more negative, such as the Olympic Peninsula and Vancouver Island, whereas it decreases less rapidly downstream of the central Cascades and the Baja Peninsula, where $D(q\boldsymbol{u})/Dt$ is less negative (or even positive). Interestingly, interior-penetrating AR trajectories see a larger decrease in $q\boldsymbol{u}$ than coastal-decaying AR trajectories over some regions (e.g., southern British Columbia), but a smaller decrease in others (e.g., the southwestern U.S., cf. Figs. 4.12a,c). We find that the spatial pattern of $D(q\boldsymbol{u})$ is not very intuitive viewed in isolation, but becomes more clear after separately considering the total changes in q and $\boldsymbol{u}$, $D(q)$ and $D(\boldsymbol{u})$, respectively.

Similarly to $D(q\boldsymbol{u})$, $D(q)$ becomes more negative from the coast to the interior, but in contrast to $D(q\boldsymbol{u})$, does so only marginally more quickly for coastal-decaying AR-trajectories (Fig. 4.12d–f). In fact, the spatial pattern of $D(q)$ is remarkably similar among the three trajectory classifications, and suggests that on average, AR trajectories ranging

from coastal-decaying to interior-penetrating experience very similar decreases in q by the time they reach a given locale. Some exceptions exist, such as those over the Mogollon Rim and San Juan Mountains, where inland- and interior-penetrating AR trajectories lose q more rapidly. However, the broad similarity in these patterns of D(q) suggests that trajectories retaining large $q\boldsymbol{u}$ and remaining AR-related upon reaching T_2 or T_3 do not necessarily do so because they are experiencing smaller decreases in q, as one might expect. Rather, they are losing a smaller fraction of their initially larger q, as evidenced by a smaller total drying ratio (cf. Figs. 4.9d–f and 4.12d–f).

In contrast to D(q), large differences exist in the spatial patterns of D($\boldsymbol{u}$) among the three trajectory classifications (cf. Figs. 4.12d–f,g–i). Over the western U.S., D($\boldsymbol{u}$) for coastal-decaying AR trajectories is almost nonexistent. For inland-penetrating trajectories, D($\boldsymbol{u}$) is largest (> 6 m s^{-1}) over the southern Cascades and northwestern Great Basin, downstream of the largest D($\boldsymbol{u}$)/Dt. For interior-penetrating trajectories, D($\boldsymbol{u}$) exceeds > 9 m s^{-1} here and over southern portions of the interior, centered on the Colorado Plateau. The differences in these patterns of D($\boldsymbol{u}$) suggest that one of the primary differences between inland- or interior-penetrating and coastal-decaying AR trajectories is that the former experience large increases in $\boldsymbol{u}$, whereas the latter do not.

Recall the paradigm described above, in which trajectories that remain AR-related as they penetrate into the interior experience decreases in q that are offset by increases in $\boldsymbol{u}$, particularly high topographical barriers. Coastal decaying AR trajectories experience decreases in q (Fig. 4.12d) that are not offset by increases in $\boldsymbol{u}$ (Fig. 4.12g), resulting in decreases in $q\boldsymbol{u}$ (Fig 4.12a). In contrast, interior-penetrating AR trajectories experience similar decreases in q (Fig. 4.12f) that *are* offset by increases in $\boldsymbol{u}$ (Fig. 4.12i), resulting

in smaller decreases in ***qu*** (Fig. 4.12c). Hence, AR trajectories that extend into the interior western U.S. are typically associated with increases in wind speed, which may partially result from an increase in AR elevation over this region.

Synoptic Composites Associated with Coastal-Decaying, Inland-, and Interior-Penetrating AR Trajectories

This section presents composites of 500 hPa geopotential heights and integrated water vapor flux (IVT) at the time of initiation for coastal-decaying, inland-, and interior-penetrating AR trajectories at three selected points (7, 12, and 17) along T_1. Point 7 is considered characteristic of many T_1 grid points along the coasts of Washington, Oregon and northern California, and the largest number of trajectories are initiated here (Fig. 4.6). Point 12, lying west of the high Sierra, features the largest difference in the distribution of ***qu*** between coastal-decaying and interior-penetrating AR trajectories, and the smallest fraction of the latter (cf. Figs. 4.6 and 4.7a). Finally, point 17 is considered somewhat characteristic of T_1 grid points along the coast of the Baja Peninsula, although we note the relatively small number of trajectories initiated here.

Trajectories initiated at point 7 are associated with a trough in the Gulf of Alaska, a ridge along or near the U.S. West Coast, and an elongated region of IVT $\geq$ 250 kg m^{-1} s^{-1} extending across the northeastern Pacific (Figs. 4.13a–c). Inland- and interior-penetrating (coastal-decaying) AR trajectories feature larger (smaller) IVT, a more (less) amplified pattern, more southwesterly (westerly) flow, and more anticyclonic (cyclonic) curvature near the coast.

Trajectories initiated at point 12 are associated with a trough extending southward from the Gulf of Alaska and a ridge over the Rocky Mountains (Figs. 4.13d–f). Similar to

those initiated at point 7, interior-penetrating AR trajectories initiated at point 12 also feature more southwesterly and stronger flow, but also a broad swath of high IVT ($\geq$ 750 kg m^{-1} s^{-1}), as expected from Fig. 4.7a. Furthermore, the trough associated with interior-penetrating AR trajectories has a longer wavelength and is located further west than that of coastal-decaying AR trajectories.

Trajectories initiated at point 17 are associated with a trough along or immediately upstream of the U.S. west coast, and a ridge of varying strength upstream of this trough (Figs. 4.13g–i). These features are more (less) amplified for inland- and interior-penetrating (coastal-decaying) AR trajectories. At point 17, the composite IVT for interior-penetrating AR trajectories is less impressive both in magnitude and coverage near landfall than that for points 7 and 12, although many of these trajectories will see an increase in water vapor flux over the Gulf of California (Fig. 4.12c). Many AR trajectories initiated here are associated with closed low-pressure systems, which contribute to the composite 500-hPa geopotential heights.

Composites of 500 hPa geopotential heights and IVT 24 h after initiation reveal that interior-penetrating AR trajectories remain associated with a more amplified atmospheric pattern as they move over the western U.S. (Fig. 4.14). In contrast, the composite pattern associated with coastal-decaying ARs has become largely zonal at 24 h. Both at trajectory initiation and upon reaching T_2 or T_3, the eastern terminus of the composite 250 kg m^{-1} s^{-1} IVT contour is typically found along the transition from an elongated region with a large gradient in geopotential to an area of difluence (cf. Figs 4.13 and 4.14). Hence, ARs appear more likely to be maintained and penetrate into the interior if a more amplified pattern and stronger gradient in 500-hPa geopotential heights

field are maintained over this region as well.

In summary, a more amplified pattern at 500 hPa, along with stronger southwesterly flow and increased IVT, are conditions conducive for inland- or interior-penetrating AR trajectories at most T_1 grid points. Such trajectories initiated west of the high Sierra are associated with very high IVT. At initiation, most AR trajectories lie within ARs that terminate near regions of 500-hPa difluence, which occurs primarily over the western U.S. However, for inland- and interior-penetrating AR trajectories, this difluent region is located further east. Additionally, these trajectories are preferentially initiated within more southern parts of the AR. Hence, as these trajectories are displaced (typically) northward (Figs. 4.4e,f), they are more likely to remain within an AR, as defined by Rutz et al. 2014 (contiguous regions $\geq$ 2000 km in length with IVT $\geq$ 250 kg m^{-1} s^{-1}).

Conclusions

This study has examined processes contributing to AR maintenance and decay over western North America by using trajectories initiated within ARs approaching the coast (24°–52.5°N) to differentiate between the characteristics of coastal-decaying, inland-, and interior-penetrating AR trajectories. The total number of trajectories initiated, for each of these classifications, is largest along the coasts of Washington, Oregon, and northern California, and decreases to the south. However, AR trajectories initiated along the Baja Peninsula are more likely to be inland- or interior-penetrating AR trajectories, whereas those initiated west of the high Sierra are least likely.

Interior-penetrating AR trajectories are characterized by larger water vapor flux at initiation than coastal-decaying AR trajectories, and this is particularly true west of the

high Sierra. Additionally, such trajectories generally feature the smallest drying ratio (i.e., smallest fractional loss of initial water vapor) of the three classifications. Furthermore, inland- and interior-penetrating AR trajectories are typically initiated with a more amplified trough-ridge pattern over the northeastern Pacific and western U.S., more southwesterly (vs. westerly) flow, and higher values of vertically integrated water vapor transport (IVT). Finally, these trajectories are often associated with a strong gradient in 500-hPa geopotential height that extends over the western U.S.

Inland- and interior-penetrating trajectories are able to maintain large water vapor flux over the western U.S. by experiencing increases in wind that offset decreases in specific humidity, particularly in the vicinity of high topographical barriers. Although coastal-decaying AR trajectories experience very similar decreases in specific humidity, they do not experience offsetting increases in wind, resulting in smaller water vapor fluxes. Hence, increasing wind speed, which may occur partially due to increased elevation, is critical to the maintenance of ARs as they extend into the interior western U.S.

These findings are subject to the resolution of the ERA-Interim reanalysis data used, which at 1.5° does not produce completely realistic trajectories. In addition, the choice of grid points used in transects T_1, T_2, and T_3 affects our results, particularly their southern and northern extent, and their placement in relation to topographical barriers. Furthermore, while we examine trajectories initiated at 950 hPa, those from other levels also contribute to the downstream environment over the western U.S.

These results improve our understanding of the processes associated with AR maintenance and decay over the western U.S. Future work focused on model verification

of the most relevant atmospheric fields (i.e., geopotential height and water vapor) could aid in differentiating between coastal-decaying and interior-penetrating ARs, and lead to better forecasts of precipitation over the interior western U.S.

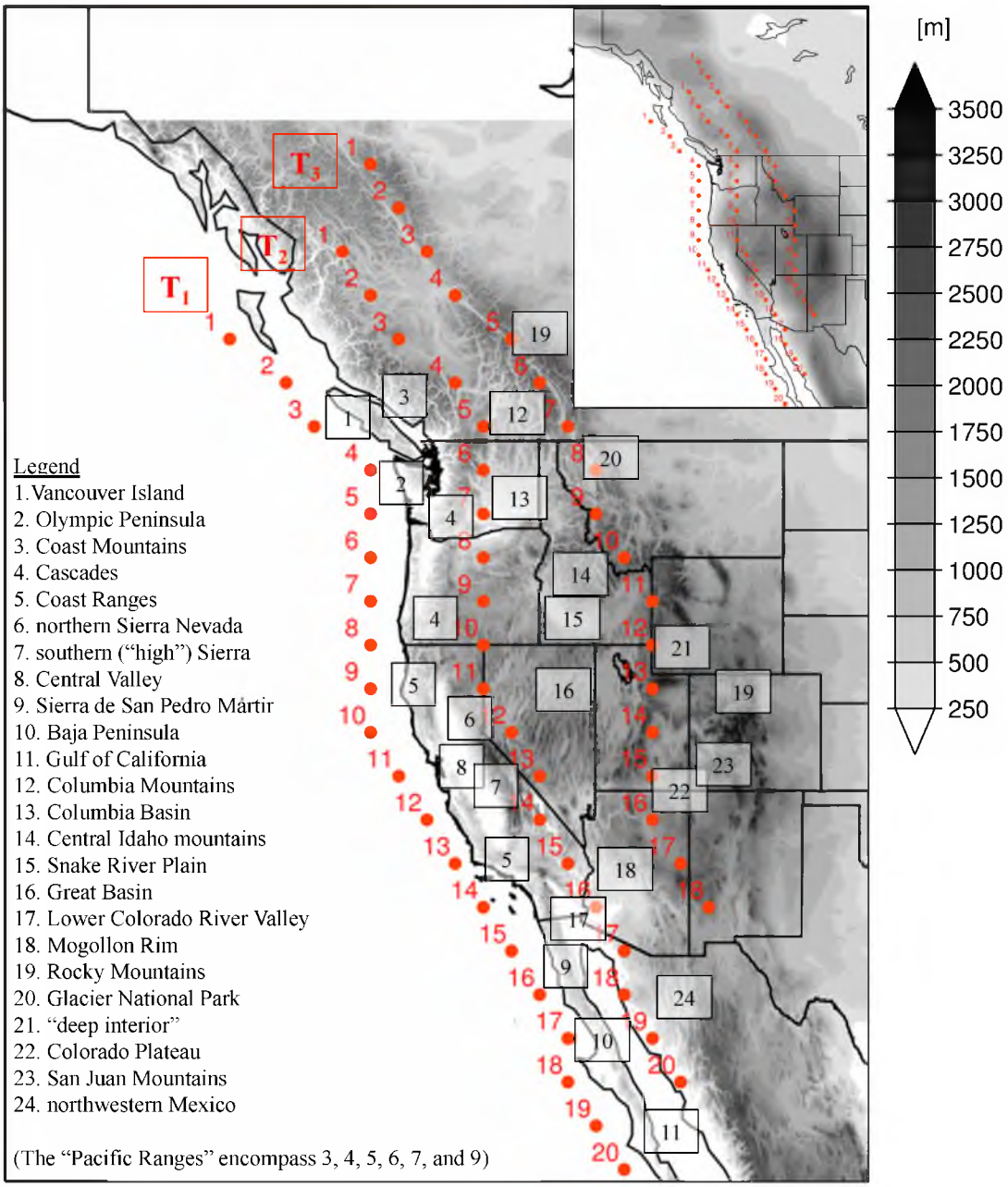

Fig. 4.1: Surface elevation (30 arc second) over the western U.S., in gray scale shading. Points along transects T_1, T_2, and T_3 are numbered in red. Legend indicates geographic terms at numbered locations. Inset figure shows ERA-Interim (1.5°) surface elevation.

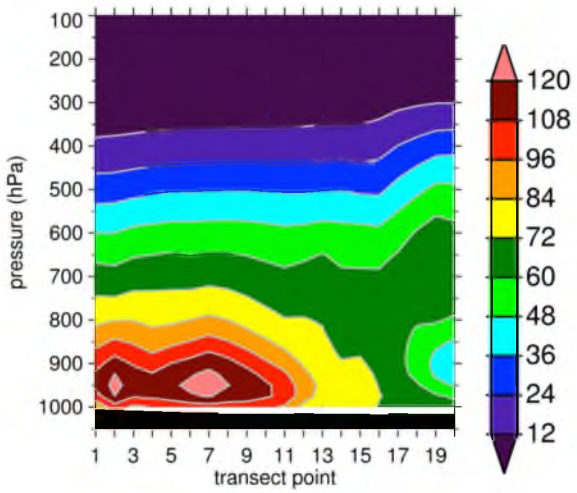

Fig. 4.2: Cross-section of mean cool-season water vapor flux when an AR is identified at T_1 grid points. Mean surface pressure shaded in black.

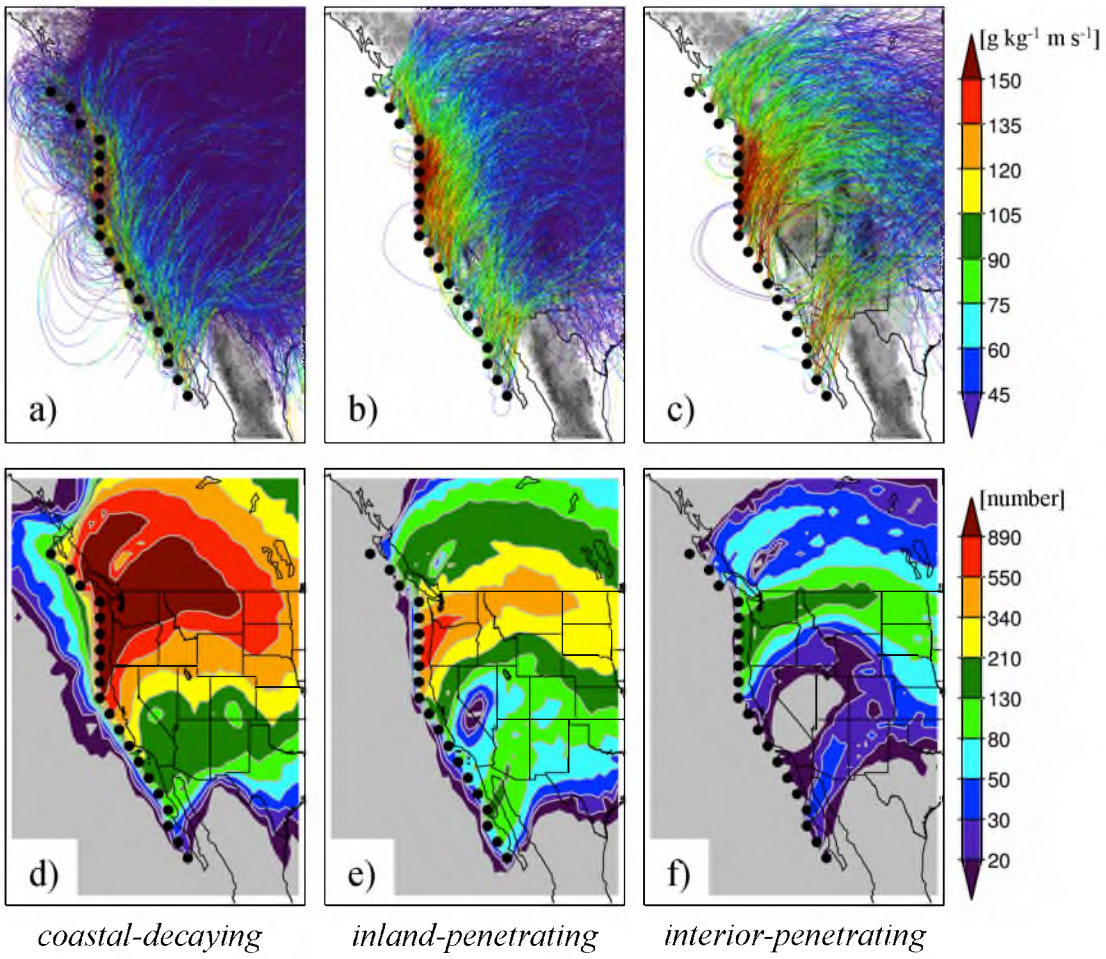

Fig. 4.3: (a–c) All (a) coastal-decaying, (b) inland-penetrating, and (c) interior-penetrating AR trajectories, colored by water vapor flux. (d–f) As in (a–c), but for trajectory count. Black circles indicate T_1 grid points.

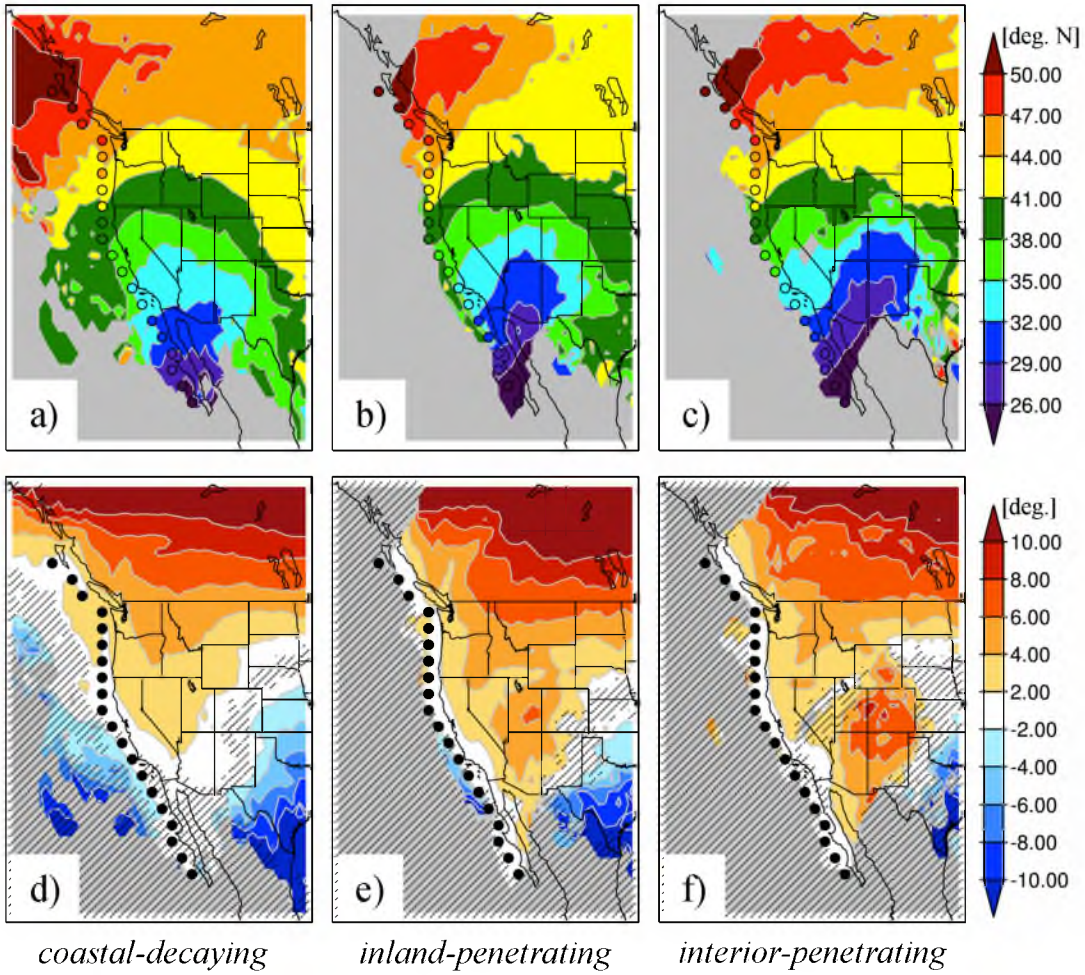

Fig. 4.4: (a–c) Spatial analysis of mean initial trajectory latitude (ϕ) for (a) coastal-decaying, (b) inland-penetrating, and (c) interior-penetrating AR trajectories. (d–f) As in (a–c), but for but for D(ϕ), integrated over time since trajectory initiation. Colored circles in (a–c) indicate latitude of T_1 grid points. Gray shading indicates no data and stippling indicates that results are not significant at the 95% confidence level following Student's *t*-test.

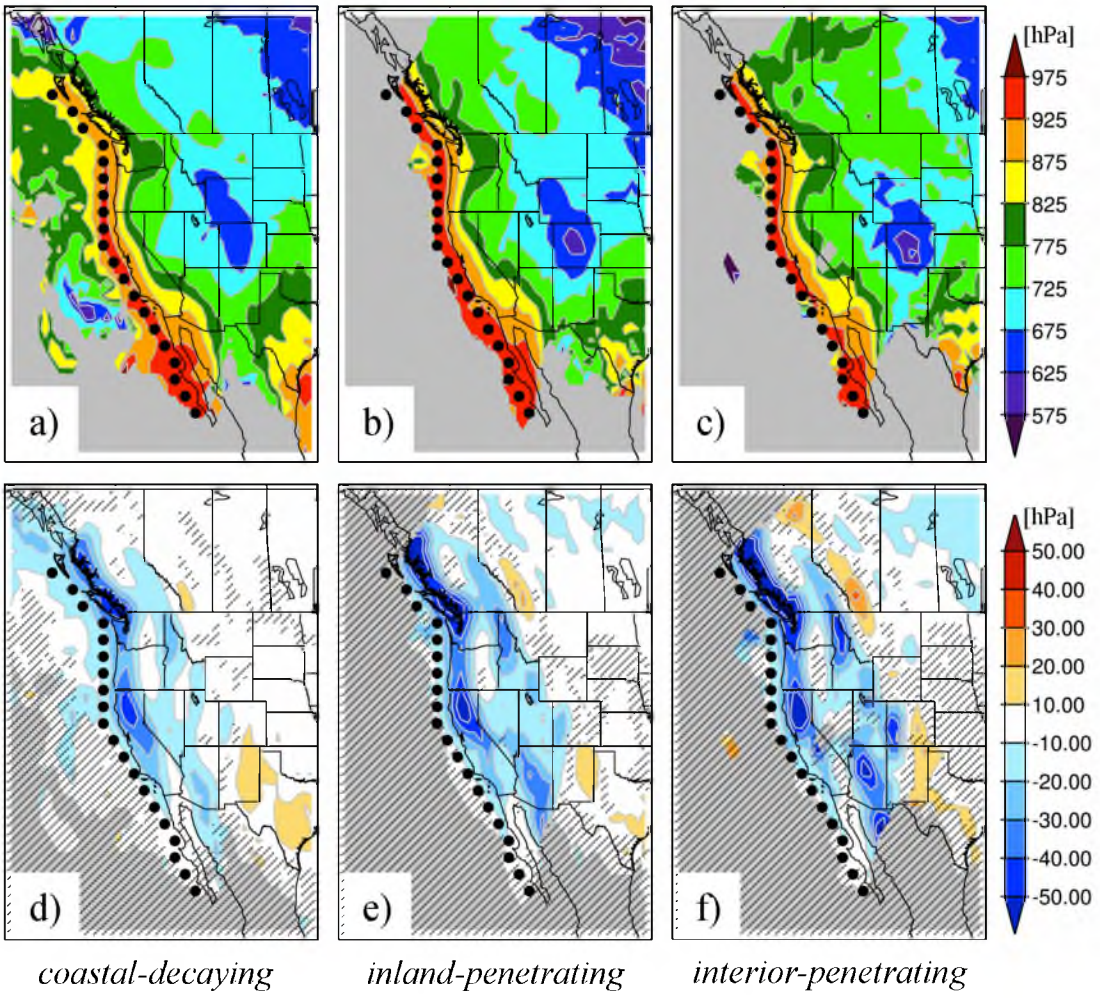

Fig. 4.5: (a–c) Spatial analysis of mean pressure (p) for (a) coastal-decaying, (b) inland-penetrating, and (c) interior-penetrating AR trajectories. (d–f) As in (a–c), but for 1-h D(p)/Dt. Black circles indicate T_1 grid points. Gray shading indicates no data and stippling indicates that results are not significant at the 95% confidence level following Student's t-test.

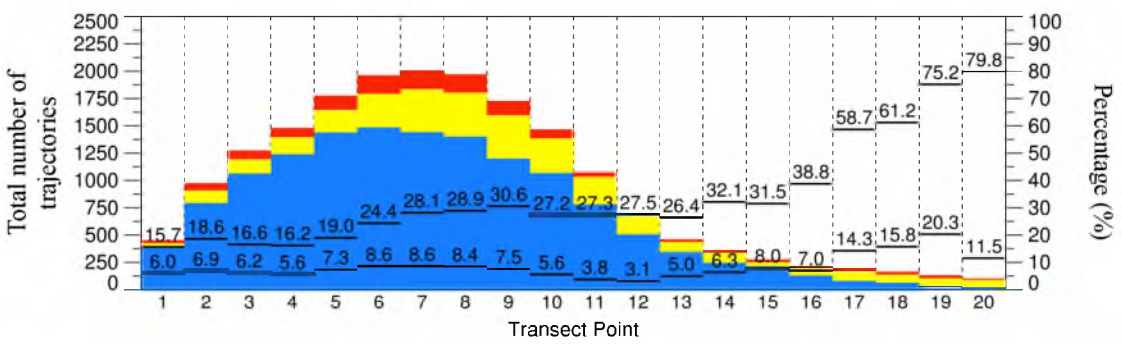

Fig. 4.6: Number of coastal-decaying (blue), inland-penetrating (yellow), and interior-penetrating (red) AR trajectories initiated at T_1 grid points (left axis corresponds to the total of all three). Percentage of trajectories that are inland-penetrating (upper series of black horizontal lines and numbers) and interior-penetrating (lower series of black horizontal lines and numbers), with right axis corresponding to these percentages.

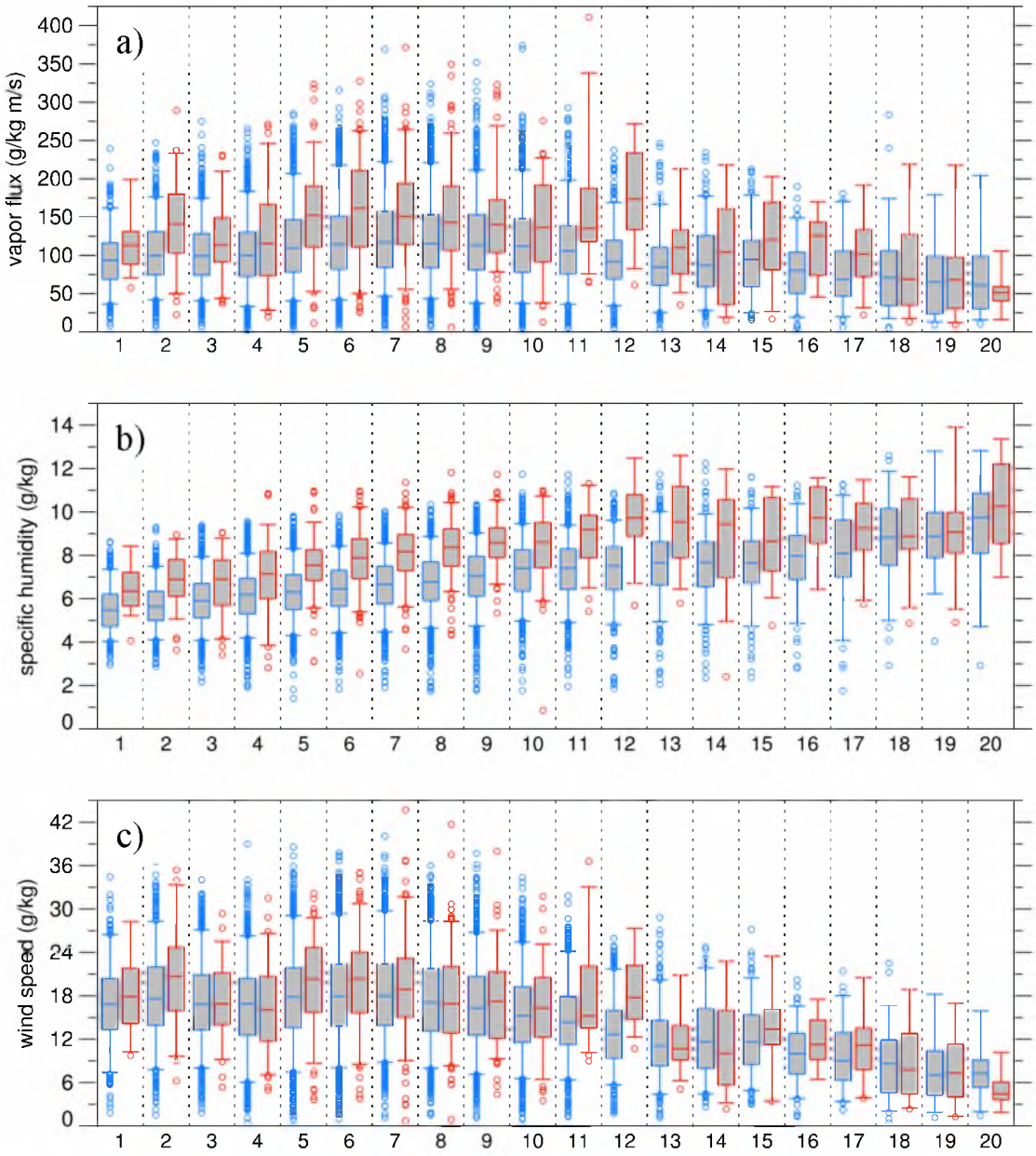

Fig. 4.7: (a) Box and whisker plot of initial water vapor flux ($q\boldsymbol{u}$) at T_1 grid points for (blue) coastal-decaying AR trajectories and (red) interior-penetrating AR trajectories. Grey-shaded boxes indicate the interquartile range. Horizontal line within gray-shaded boxes indicates the median, and horizontal lines outside of boxes indicate the 5th and 95th percentiles. Circles indicate values below the 5th and above the 95th percentiles. (b) As in (a), but for specific humidity (q). (c) As in (a), but for wind ($\boldsymbol{u}$).

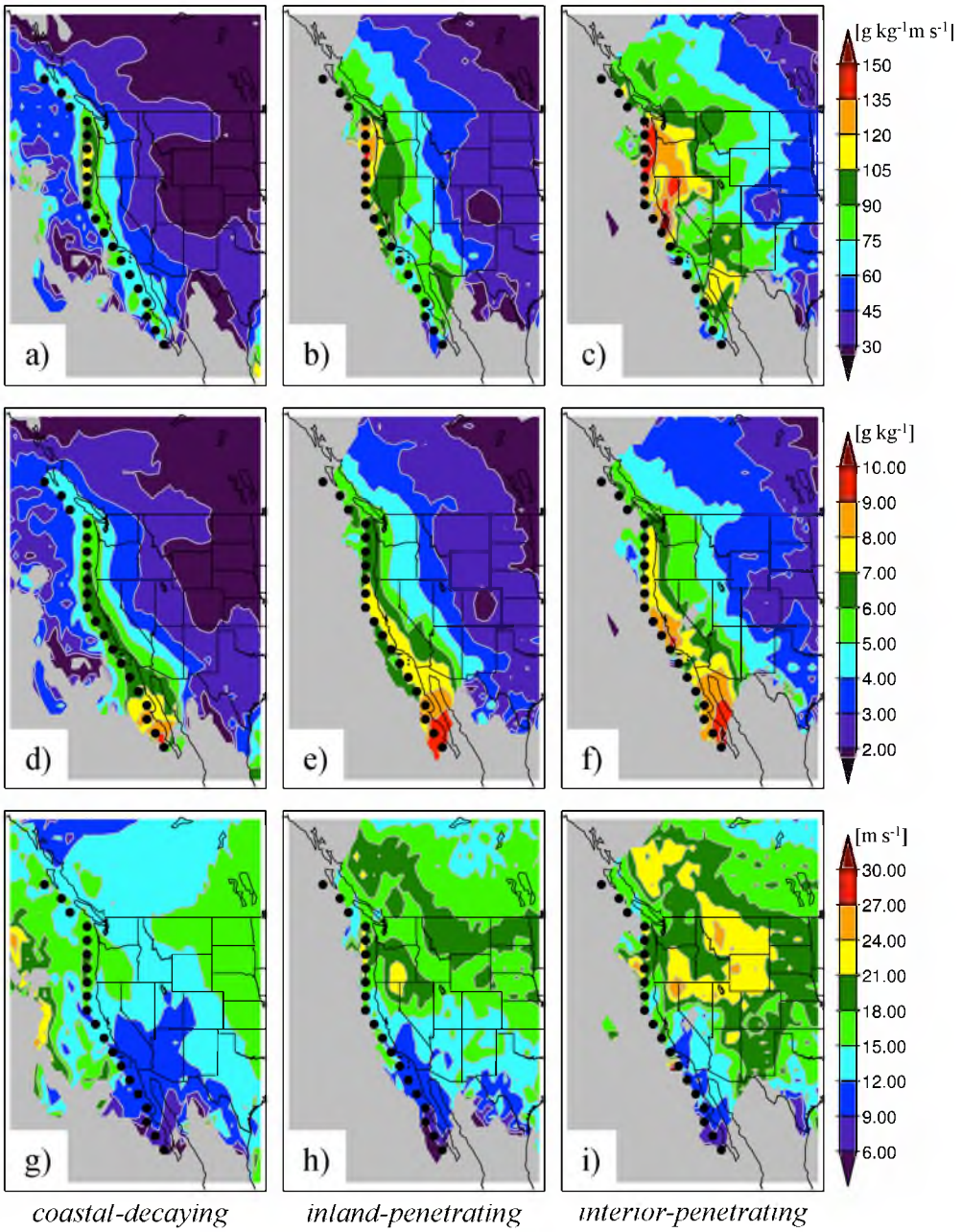

Fig. 4.8: (a–c) Spatial analysis of mean $\boldsymbol{qu}$ for (a) coastal-decaying, (b) inland-penetrating, and (c) interior-penetrating AR trajectories. (d–f) As in (a–c), but for q. (g–i) As in (a–c), but for $\boldsymbol{u}$. Black circles indicate T_1 grid points. Gray shading indicates no data.

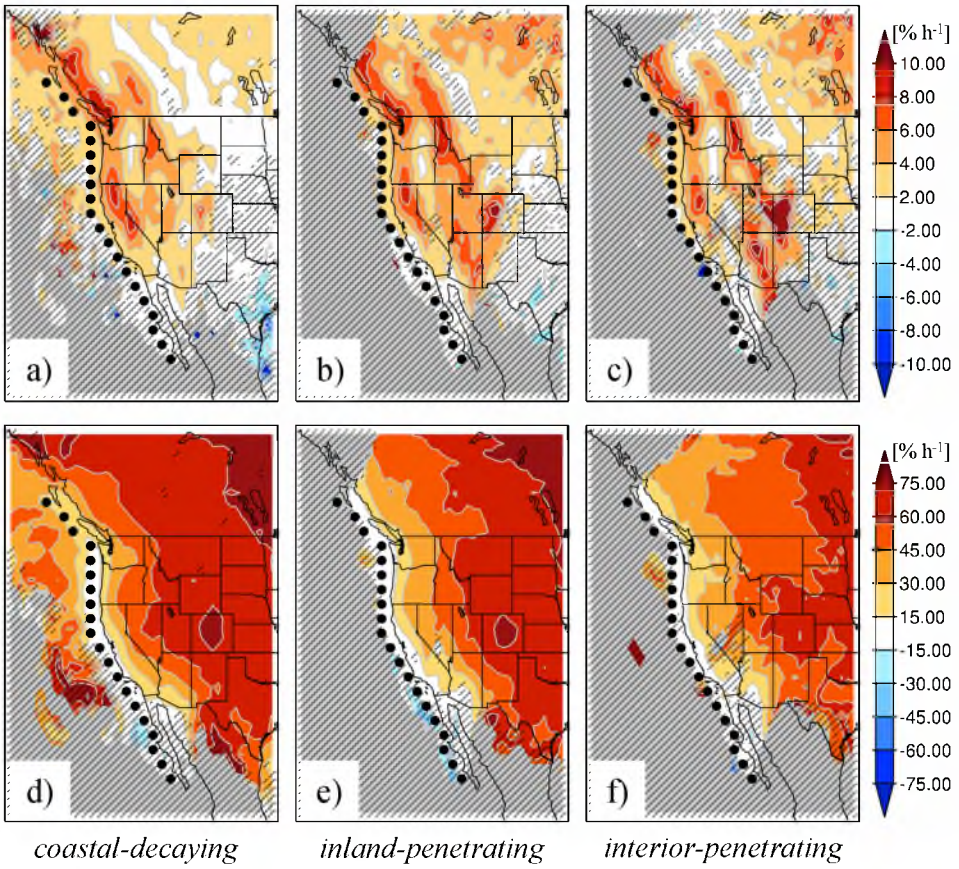

Fig. 4.9: (a–c) Spatial analysis of mean 1-h drying ratio for (a) coastal-decaying, (b) inland-penetrating, and (c) interior-penetrating AR trajectories. (d–f) As in (a–c), but for the drying ratio integrated over time since trajectory initiation. Black circles indicate T_1 grid points. Gray shading indicates no data and stippling indicates that results are not significant at the 95% confidence level following Student's *t*-test.

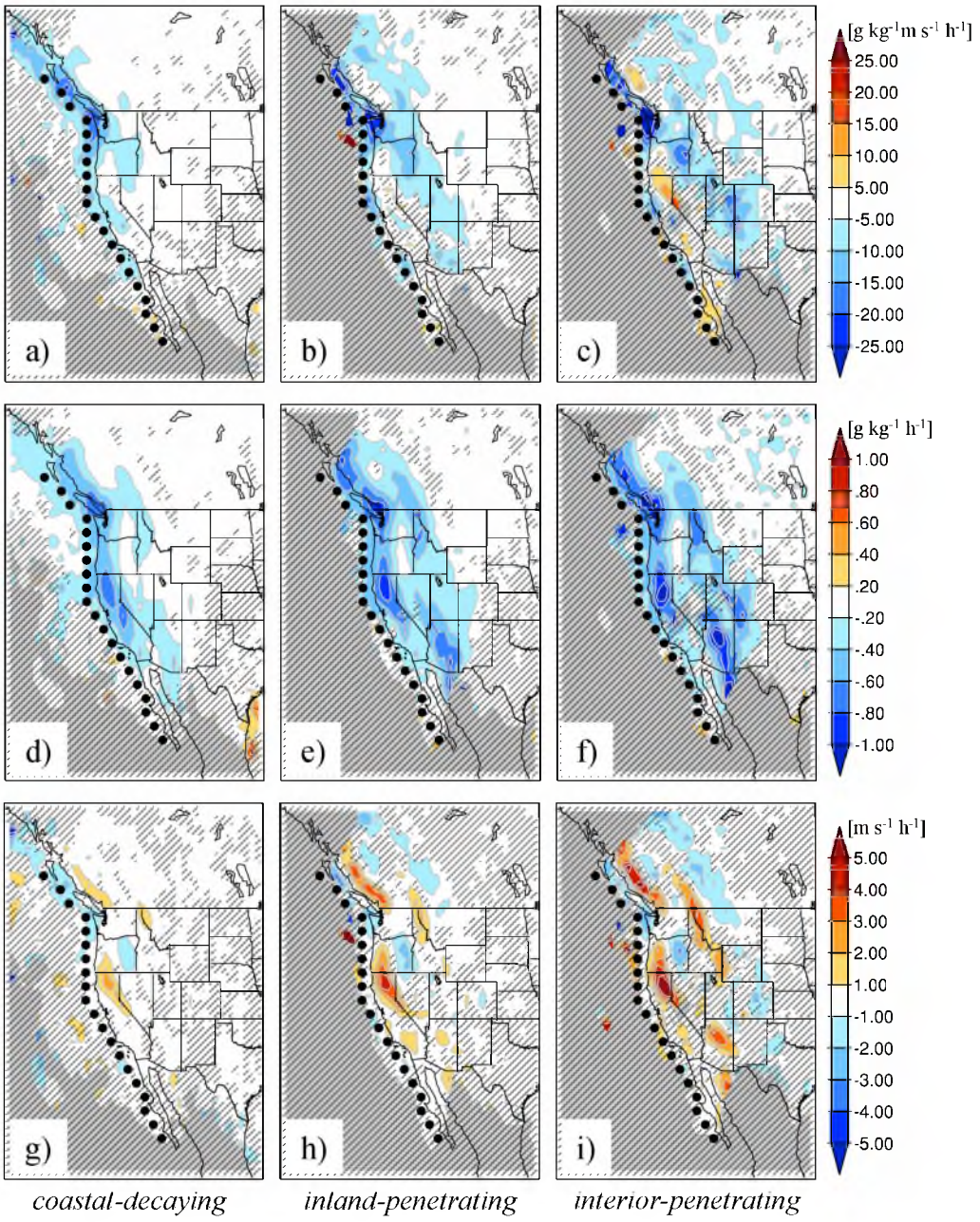

Fig. 4.10: (a–c) Spatial analysis of mean 1-h D(***qu***)/Dt for (a) coastal-decaying, (b) inland-penetrating, and (c) interior-penetrating AR trajectories. (d–f) As in (a–c), but for D(*q*)/Dt. (g–i) As in (a–c), but for D(***u***)/Dt. Black circles indicate T_1 grid points. Gray shading indicates no data and stippling indicates that results are not significant at the 95% confidence level following Student's *t*-test

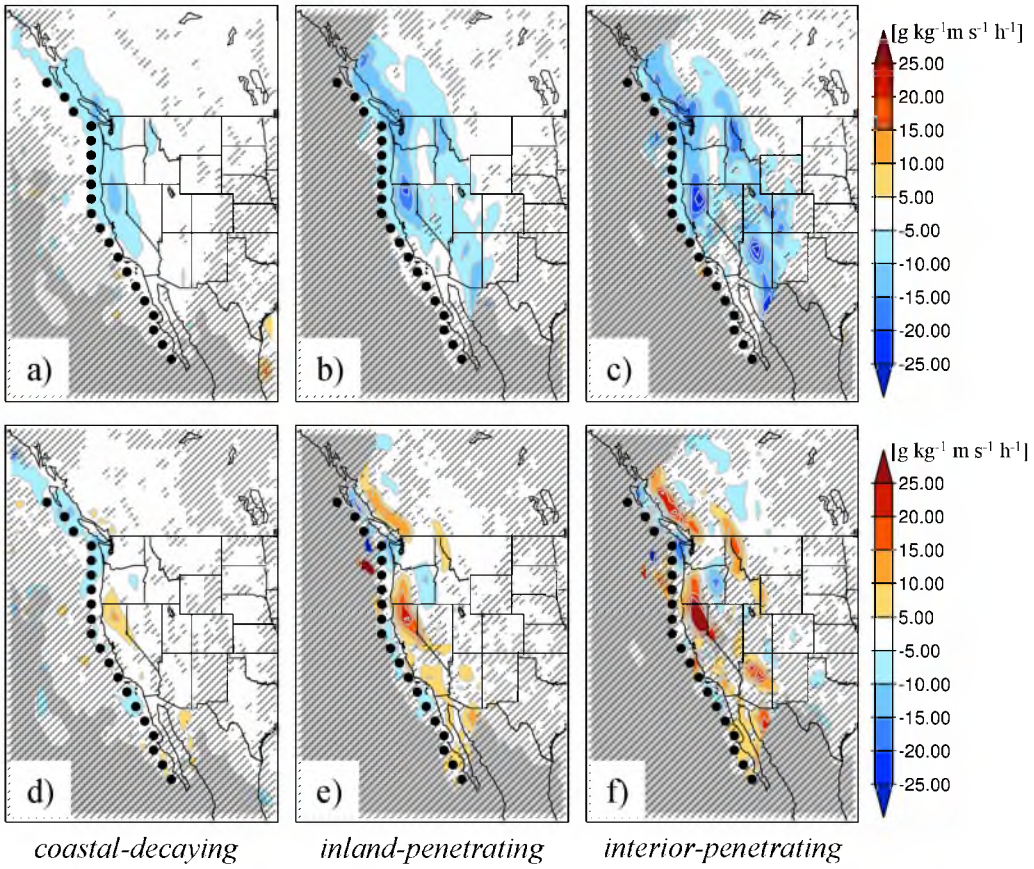

Fig. 4.11: (a–c) Spatial analysis of mean thermodynamic contribution to changes in water vapor flux, $\boldsymbol{u}(Dq/Dt)$, for (a) coastal-decaying, (b) inland-penetrating, and (c) interior-penetrating AR trajectories. (d–f) As in (a–c), but for mean dynamic contribution to changes in water vapor flux, $q(D\boldsymbol{u}/Dt)$. Black circles indicate T_1 grid points. Gray shading indicates no data and stippling indicates that results are not significant at the 95% confidence level following Student's *t*-test.

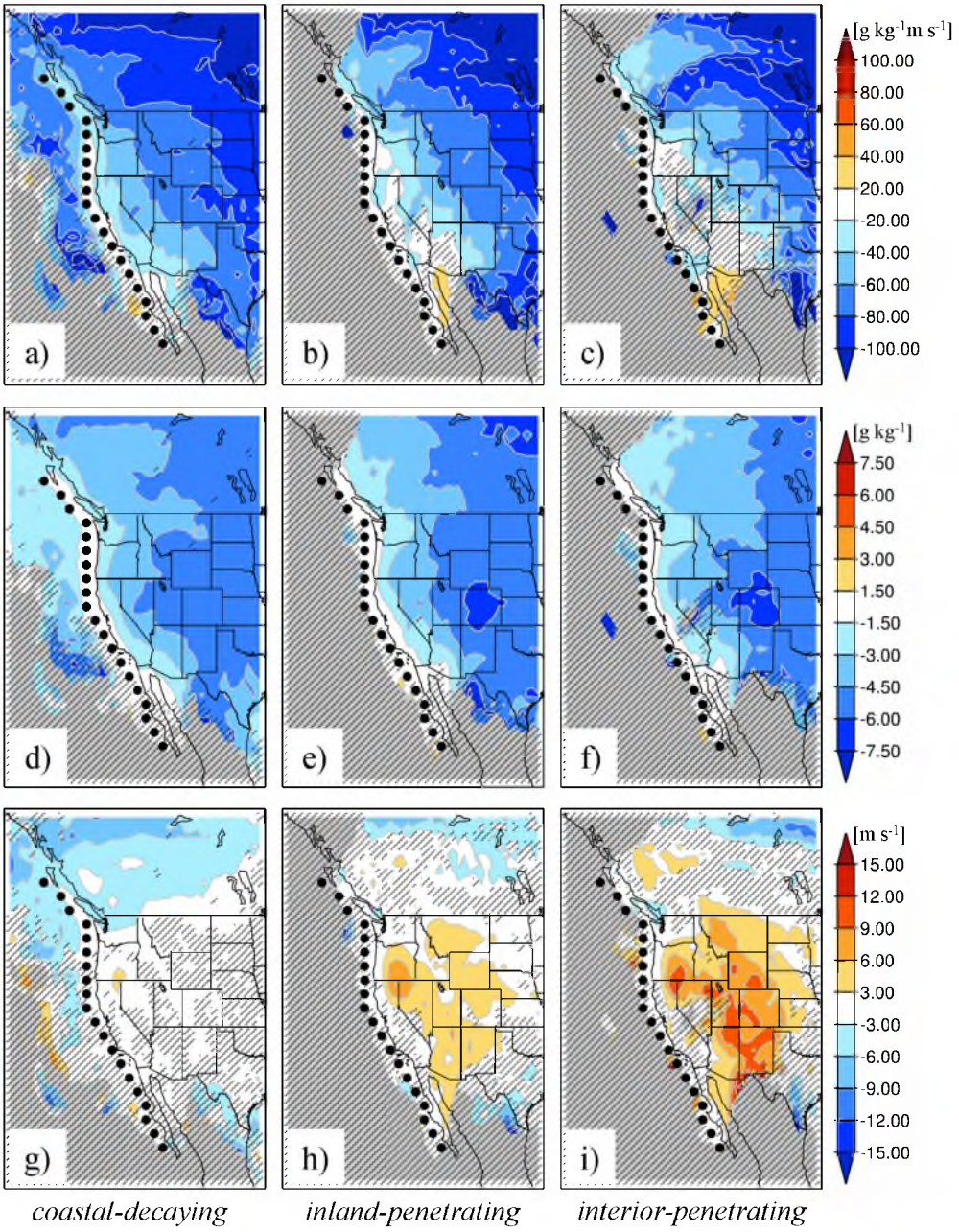

Fig. 4.12: (a–c) Spatial analysis of mean D(***qu***), integrated over time from trajectory initiation, for (a) coastal-decaying, (b) inland-penetrating, and (c) interior-penetrating AR trajectories. (d–f) As in (a–c), but for D(q). (g–i) As in (a–c), but for D(***u***). Black circles indicate T_1 grid points. Gray shading indicates no data and stippling indicates that results are not significant at the 95% confidence level following Student's t-test.

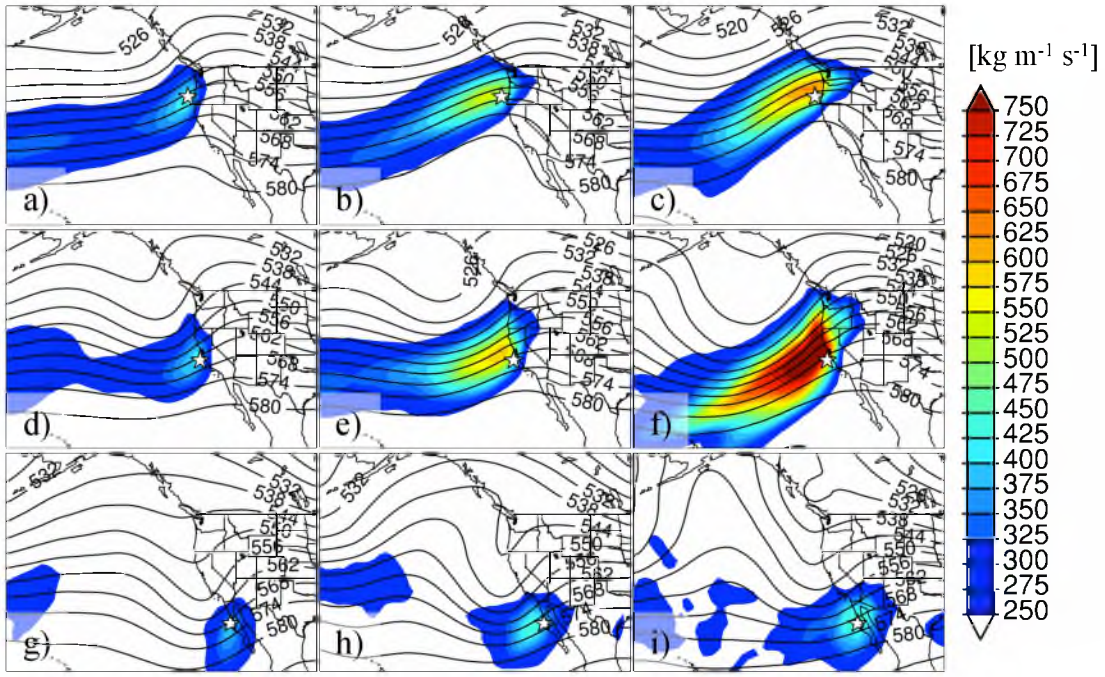

Fig. 4.13: (a–c) Composite of 500 hPa geopotential heights (contours) and integrated water vapor flux (color shading) at the time of initiation for (a) coastal-decaying, (b) inland-penetrating, and (c) interior-penetrating AR trajectories from point 7 (starred location). (d–f) As in (a–c), but for point 12. (g–i) As in (a–c), but for point 17.

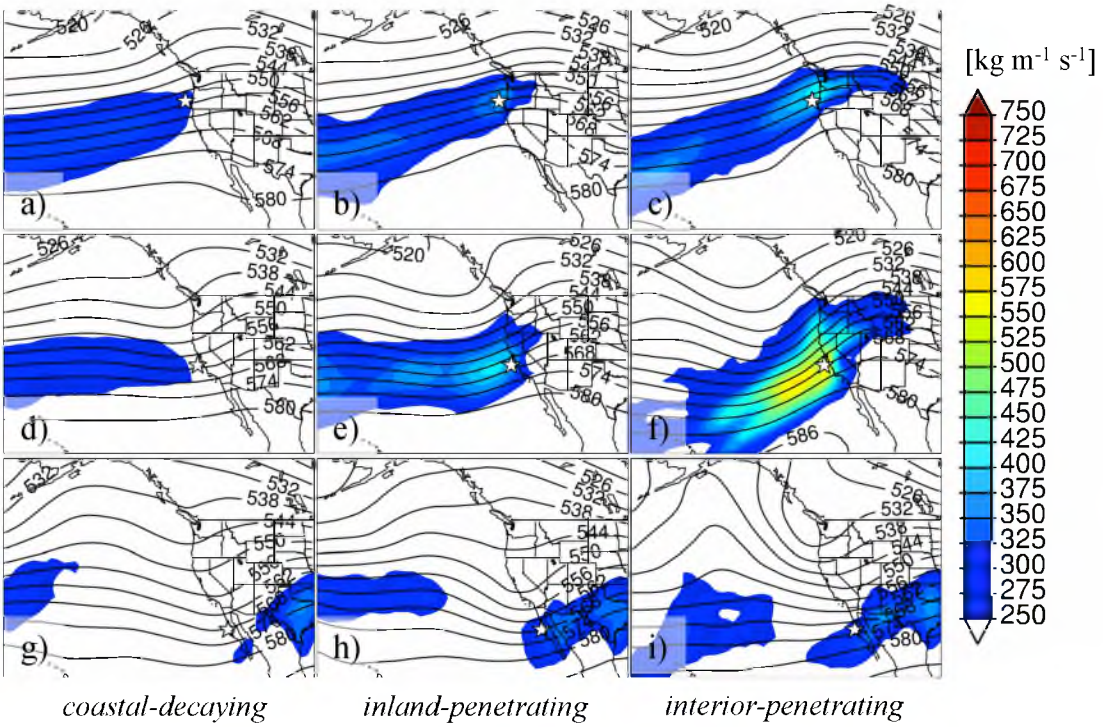

Fig. 4.14: As in Fig. 4.13, but for 24 h after time of initiation.

CHAPTER 5

CONCLUDING REMARKS

Summary of Findings

This study has examined the climatological characteristics and inland penetration of atmospheric rivers (ARs) over the western U.S. Chapter 2 shows that more than 15% of cool-season (November–April) precipitation over parts of the southwestern U.S. is attributable to ARs making landfall along the Baja Peninsula of Mexico, whereas previous analyses had considered only landfalling ARs north of the U.S./Mexico border.

Chapter 3 quantifies the climatological characteristics (i.e., the frequency, duration, and influence on precipitation) of cool-season ARs over the western U.S. To facilitate this, ARs are objectively identified based on vertically integrated water vapor transport (IVT), which is better correlated with cool-season precipitation over the western U.S. than integrated water vapor (IWV). Using this approach, we find that the AR frequency, mean duration, and influence on cool-season precipitation are largest along the Oregon and Washington coasts, decrease southward along the California coast and eastward across the Cascades–Sierra Ranges, and smallest over the eastern Great Basin and the central Rockies. Over the southwest U.S., the mean AR duration and influence of ARs on precipitation are large relative to the AR frequency, indicating that although ARs are less common in this region, they are typically long-lived, generate heavy

precipitation, and contribute significantly to the regional hydroclimate. The geographic distribution of these characteristics appears to be strongly influenced by the climatology of landfalling ARs along the west coast and by water vapor depletion due to precipitation, particularly over high topographic barriers such as the southern or "high" Sierra.

Chapter 4 differentiates between the characteristics and processes of ARs decaying near the U.S. west coast and those that penetrate into the interior. This is done using trajectories released at low-level (i.e., 950 hPa) within ARs approaching the coast. These trajectories are then classified as coastal decaying, inland-penetrating, orinterior-penetrating depending on whether or not they remain within an AR upon reaching selected transects over the western U.S. Interior-penetrating AR trajectories initially feature a more amplified trough-ridge pattern, stronger southwesterly flow, and larger IVT than coastal-decaying AR trajectories. As theinterior-penetrating trajectories move inland, they experience water vapor depletion from precipitation, especially over major mountain barriers, but their larger initial IVT, combined with an increase in wind speed, allows for the maintenance of large IVT values into the interior.

An integrated summary of results found in these chapters can be presented in terms of three geographic regimes (Fig. 5.1).

The first regime consists of ARs making landfall on the U.S. west coast north of Cape Mendocino (~40.5°N), and sometimes penetrating into southwestern Canada and the interior northwestern U.S. The largest cool-season AR frequency (> 15%), featuring a November maximum, and the largest mean AR duration (> 20 h) are observed along this stretch of coast. In addition, the largest fractions of top-decile precipitation events (> 65%) and cool-season precipitation (> 50%) attributable to ARs (top-decile and AR

fractions, respectively) are also observed from here eastward to the Cascades. East of this range, the largest inland values of AR frequency (5–10%) and mean AR duration (> 18 h) are found over the low-elevation corridor that extends from the Columbia River Basin eastward through the northern U.S. Rocky Mountains. The top-decile and AR fractions over this region range from 15–45% and 25–45%, respectively.

AR-related low-level trajectories approaching the coast within this regime typically feature larger water vapor fluxes than trajectories further south, and comprise the majority of all trajectories (68.4%). The majority of these trajectories turn anticyclonically toward the northeast as they ascend over the Cascades, experiencing moderate amounts of water vapor depletion in the process, and upon reaching the lee of this range, 24.9% of the initial trajectories remain AR-related. Although not a large percentage, the number of initial trajectories is largest within this regime, so the addition of many events contributes to large inland AR frequency and fractions across this region. Of the trajectories remaining AR-related in the lee of the Cascades, 31.2% (or 7.8% of those approaching the coast) remain AR-related upon reaching the northern Rockies, indicative of further AR decay across the northwest interior, though not to the extent occurring over the Cascades.

The second regime consists of ARs approaching the west coast south of Cape Mendocino and north of Point Conception (~34.5–40.5°N), and sometimes penetrating into the interior northwest U.S., or more rarely the interior southwest U.S. The AR frequency, featuring a December maximum, decreases rapidly from north (15%) to south (5%) along this stretch of coast, and the mean AR duration is smaller (18–20 h) than found further north. Similarly, the top-decile (AR) fraction decreases from > 65% (60%)

near Cape Mendocino to > 55% (45%) near Point Conception. Many ARs within this regime contribute to a relatively high AR frequency (3–10%) over the northwestern Great Basin, the adjoining Snake River Plain, and the interior northwest, and likely contribute to the top-decile and AR fractions of this region as well. In contrast, very few ARs extend eastward over the high Sierra. Subsequently, the AR frequency (< 16%), mean duration (< 16 h), top-decile fraction (< 25%), and AR fraction (< 25%) downstream of this range, over the central and southern Great Basin, are all very small.

Low-level trajectories within this regime, comprising 23.2% of the total, follow one of three pathways: an anticyclonic path traversing the relatively low crest of the Cascade–Sierra Ranges north of Lake Tahoe, a path directly over the high Sierra, or most rarely, a cyclonic path south of the high Sierra. Those following a pathway north or south of the high Sierra are more commonly able to maintain larger water vapor fluxes and remain AR-related east of the Cascades–Sierra ranges, whereas those passing over the high Sierra experience large decreases in water vapor flux, indicative of AR decay. In total, 27.2% of the trajectories in this regime remain AR-related upon reaching the lee of the Cascades and Sierra, with the vast majority of these following the northernmost path. Of these, only 16.7% (or 4.5% of those approaching the coast) remain AR-related upon reaching the next major topographical barrier, which stretches from Wasatch Mountains northward through western Wyoming and Idaho. These smaller numbers partly reflect the complex topography of the northwestern Great Basin and interior northwest.

Finally, the third regime consists of ARs approaching the west coast south of Point Conception (34.5°N), including those approaching the coast of the Baja Peninsula, and sometimes penetrating into the interior southwest U.S. The AR frequency, featuring a

January maximum, is very low (< 4%) along much of this coastline, but the mean AR duration is similar to that of the central California coast. Over southern California, the AR fraction (40–55%) and top-decile fraction (55–70%) are large relative to the AR frequency, particularly along and upstream of the Transverse and Peninsular Ranges. Further inland, from the lower Colorado River Basin north and east to the higher topography of the central Great Basin and the Mogollon Rim, the climatological characteristics of ARs are quite homogenous. The AR frequency is very low (< 3%), whereas the mean AR duration is relatively high (> 16 h). The top-decile and AR fractions are comparable to, or larger than, those found over the interior northwest, which makes them quite large relative to the limited AR frequency. Larger decreases in these characteristics are found as one moves north and east over the Mogollon Rim and across the Colorado Plateau.

Low-level trajectories within this regime account for only 8.4% of the total, and this is representative of the low AR frequency over this region. Those approaching the coast of southern California often exhibit cyclonic curvature as they pass southward of the high Sierra and into the southwestern U.S., whereas trajectories approaching the Baja Peninsula move north or northeast into this region. Trajectories within this regime typically have smaller water vapor fluxes near the coast than those further north, but most of these trajectories experience very limited amounts of water vapor depletion (some experience increases) over the mountains of southern California and the Baja Peninsula. Upon reaching the lower Colorado River Basin and the northeastern Gulf of California, 44.7% of the initial trajectories still remain AR-related, contributing to the relatively large top-decile and AR fractions of this region. Of these, 23.4% (or 10.5% of those

approaching the coast) remain AR-related upon reaching the lee side of the Mogollon Rim and the mountains of southwestern Utah, as much larger amounts of water vapor depletion take place over these ranges.

In the coming decades, the western U.S. is likely to face increasing water resource challenges, driven by changes in climate and increases in demand. The current scientific consensus, despite uncertainties, anticipates warming temperatures, changing precipitation patterns, and reductions in high-elevation snowpack, which is a crucially important source of regional water supply. Increases in population and agricultural demand, combined with changes in climate, will put pressure on a system that is already stretched. The ability of policymakers to anticipate and act on future changes in water supply will become increasingly necessary. This study has taken a step toward addressing this need by illustrating the contribution of ARs to hydroclimate over the western U.S. Two critical next steps are to understand how this distribution may change in the future if the location and/or intensity of ARs change, and to improve predictive skill with regard to ARs and heavy precipitation in the weeks–months time frame.

Future Work

The last decade has seen rapid advances in our understanding of ARs, our ability to observe and forecast them, and their impacts on weather and climate. However, many questions remain with regard to the ability of numerical weather prediction (NWP) models to forecast ARs and their associated precipitation. Wick et al. (2013) showed that over 3 cool seasons, NWP ensemble systems struggled, particularly with forecasts of AR landfall, with errors of ~800 km at a 10-day lead (ARs were identified using IWV). Furthermore, even highly accurate forecasts of ARs developing and approaching the

North American west coast may produce inaccurate precipitation forecasts over the interior, owing to complex topography, imperfect model resolution, and unresolved microphysical processes. Hence, one topic of future work should be an evaluation of NWP forecasts of AR development and inland penetration, using IVT and a longer data set, documenting the nature of errors (e.g., timing, placement, intensity), and if possible, identifying their sources.

One of the primary challenges in forecasting ARs and resultant precipitation is the low predictability of NWP moisture fields. An assessment of the relationship between ARs and the anomalies of other fields with greater predictability (e.g., geopotential height) could potentially improve our ability to anticipate and forecast AR-related impacts in the short term, bypassing the need for more accurate moisture fields until it is realized. Furthermore, recent studies (e.g., Tang et al. 2007; Riddle et al. 2013; Smith et al. 2013) point toward improved predictability of certain short-term climate indicators, such as the Arctic Oscillation (AO). As the predictability of these indicators increases, an assessment of the relationship between ARs and indicators like the AO could potentially lead to improved short-term climate forecasts, particularly those relating to precipitation.

REFERENCES

Bales, R. C., N. P. Molotch, T. H. Painter, M. Dettinger, R. Rice, and J. Dozier, 2006: Mountain hydrology of the western United States, *Water Resour. Res.,* **42**, W08432. doi: 10.1029/2005WR004387.

Bao, J.-W., S. A. Michelson, P. J. Neiman, F. M. Ralph, and J. M. Wilczak, 2006: Interpretation of enhanced integrated water vapor bands associated with extratropical cyclones: their formation and connection to tropical moisture. *Mon. Wea. Rev.*, **134**, 1063–1080.

Bernhardt, D., 2006: Glacier National Park flooding November 2006. NWS Western Region Technical Attachment 08-23.

Berrisford, P., D. Dee, K. Fielding, M. Fuentes, P. Kallberg, S. Kobayashi, and S. Uppala, 2009: The ERA-Interim archive. ECMWF Tech. Rep. 1, 16 pp. [Available online at http://www.ecmwf.int/publications/library/do/references/show?id=89203].

Browning, K. A., 1971: Radar measurements of air motion near fronts. *Weather*, **26**, 320–340.

Bureau of the Census, cited 2013: Percent change in population for states and Puerto Rico: April 1, 2000 to July 1, 2009.
[Available at http://www.census.gov/popest/data/maps/2009/perchg-2000-2009.html]

Carlson, T. N., 1980: Airflow through midlatitude cyclones and the comma cloud Pattern. *Mon. Wea. Rev.*, **108**, 1498–1509.

Catto, J. L., C. Jakob, G. Berry, and N. Nicholls, 2012: Relating global precipitation to atmospheric fronts, *Geophys. Res. Lett.*, **39**, L10805, doi:10.1029/2012GL051736.

Cordeira, J. M., F. M. Ralph, and B. J. Moore, 2013: The development and evolution of two atmospheric river events in proximity to western north Pacific tropical cyclones in October 2010. *Mon. Wea. Rev.*, **141**, 4234–4255.

Daly, C., W. P. Gibson, G. H.Taylor, M. K. Doggett, and J. I. Smith: Observer bias in daily precipitation measurements at United States cooperative network stations. *Bull. Amer. Meteor. Soc.,* **88**, 899–912.

Dee, D. P., and coauthors, 2011: The Era-Interim reanalysis: configuration and performance of the data assimilation system. *Quart. J. Roy. Met. Soc.*, **137,** 553–597.

Dettinger, M. D., F. M. Ralph, T. Das, P. J. Neiman, and D. R. Cayan, 2011: Atmospheric rivers, floods, and the water resources of California. *Water*, **2011(3),** 445–478.

Didlake, A. C., Jr., 2007: An analysis of water vapor flux and orographic precipitation in northern California. B. S. thesis, Dept. of Geology and Geophysics, Yale University, 47 pp.

Eckhardt, S., A. Stohl, H. Wernli, P. James, C. Forster, and N. Spichtinger, 2004: A 15-year climatology of warm conveyor belts. *J. Climate*, **17**, 218–237.

Guan, B., N. P. Molotch, D. E. Waliser, E. J. Fetzer, and P. J. Neiman, 2010: Extreme snowfall events linked to atmospheric rivers and surface air temperature via satellite measurements, *Geophys. Res. Lett.*, **37**, L20401, doi:10.1029/2010GL044696.

Hart, K. A., W. J. Steenburgh, and D. J. Onton, 2005: Model forecast improvements with decreased horizontal grid spacing over finescale intermountain orography during the 2002 olympic winter games. *Wea. Forecasting,* **20,** 558–576. doi:0.1175/WAF865.1

Hawcroft, M. K., L. C. Shaffrey, K. I. Hodges, and H. F. Dacre, 2012: How much Northern Hemisphere precipitation is associated with extratropical cyclones?, *Geophys. Res. Lett.*, **39**, L24809, doi:10.1029/2012GL053866.

Higgins, R. W., W. Shi, E. Yarosh, and R. Joyce, 2000: *Improved United States precipitation quality control system and analysis*, NCEP/Climate Prediction Center ATLAS No. 7.

Hughes, M., P. J. Neiman, E. Sukovich and F. M. Ralph, 2012: Representation of the Sierra Barrier Jet in 11 years of a high-resolution dynamical reanalysis downscaling compared with long-term wind profiler observations. *J. Geophys. Res.*, **117**, D18116..

Junker, N. W., R. H. Grumm, R. Hart, L. F. Bosart, K. M. Bell, F. J. Pereira, 2008: Use of normalized anomaly fields to anticipate extreme rainfall in the mountains of northern California. *Wea. Forecasting*, **23**, 336–356.

Kanamitsu, M., 1989: Description of the NMC Global Data Assimilation and Forecast System. *Wea. Forecasting*, **4**, 335–442.

Kingsmill, D. K., P. J. Neiman, B. J. Moore, M. Hughes, S. E. Yuter, and F.M. Ralph, 2013: Kinematic and thermodynamic structures of Sierra barrier jets and overrunning atmospheric rivers during a land-falling winter storm in Northern California. *Mon. Wea. Rev.*, **141**, 2015–2036.

Knippertz, P., and H. Wernli, 2010: A Lagrangian climatology of tropical moisture exports to the Northern Hemispheric extratropics. *J. Climate*, **23**, 987–1003.

Knippertz, P., Wernli, H., and G. Gläser, 2013: A global climatology of tropical moisture exports. *J. Climate,* 26, 3031–3045.

Lackmann, G. M., J. R. Gyakum, R. Benoit, 1998: Moisture transport diagnosis of a wintertime precipitation event in the Mackenzie River Basin. *Mon. Wea. Rev.*, **126**, 668–692.

Lareau, Neil P., John D. Horel, 2012: The Climatology of Synoptic-Scale Ascent over Western North America: A Perspective on Storm Tracks. *Mon. Wea. Rev.*, **140**, 1761–1778.

Lavers, D. A., R. P. Allen, E. F. Wood, G. Villarini, D. J. Brayshaw, and A. J. Wade, 2011: Winter floods in Britain are connected to atmospheric rivers, *Geophys. Res. Lett.,* **38,** L23803, doi: 10.1029/2011GL049783.

Lavers, D. A., and G. Villarini, 2013: The nexus between atmospheric rivers and extreme precipitation across Europe, *Geophys. Res. Lett.*, **40**, 1–6.

Lundquist, J. D., P. J. Neiman, B. Martner, A. B. White, D. J. Gottas, F. M. Ralph, 2008: Rain versus snow in the Sierra Nevada, California: comparing doppler profiling radar and surface observations of melting level. *J. Hydrometeor*, **9**, 194–211. doi: 10.1175/2007JHM853.1

Moore, B. J., P. J. Neiman, F. M. Ralph, F. E. Barthold, 2012: Physical processes associated with heavy flooding rainfall in Nashville, Tennessee, and vicinity during 1–2 May 2010: The role of an atmospheric river and mesoscale convective systems. *Mon. Wea. Rev.*,**140**, 358–378.

Neiman, P. J., F. M. Ralph, A. B. White, D. E. Kingsmill, and P. O. G. Persson, 2002: The statistical relationship between upslope flow and rainfall in California's Coastal Mountains: observations during CALJET. *Mon. Wea. Rev.*, **130**, 1468–1492.

Neiman, P. J., F. M. Ralph, G. A. Wick, Y.-H. Kuo, T.-K. Wee, Z. Ma, G. H. Taylor, and M. D. Dettinger, 2008a: Diagnosis of an intense atmospheric river impacting the Pacific Northwest: storm summary and offshore vertical structure observed with COSMIC satellite retrievals. *Mon. Wea. Rev.*, **136**, 4398–4420.

Neiman, P. J., F. M. Ralph, G. A. Wick, J. D. Lundquist, M. D. Dettinger, 2008b: Meteorological characteristics and overland precipitation impacts of atmospheric rivers affecting the west coast of North America based on eight years of SSM/I satellite observations. *J. Hydromet.*, **9**, 22–47. doi: 10.1175/2007JHM855.1

Neiman, P.J., E. M. Sukovich, F. M. Ralph, and M. Hughes, 2010: A seven-year wind profiler-based climatology of the windward barrier jet along California's Sierra Nevada. *Mon. Wea. Rev.* **138**, 1206–1233.

Neiman, P, J., L, J. Schick, F. M. Ralph, M. Hughes, G. A. Wick, 2011: Flooding in western Washington: the connection to atmospheric rivers. *J. Hydromet.*, **12**, 1337–1358.

Neiman, P. J., F. M. Ralph, B. J. Moore, M. Hughes, K. M. Mahoney, J. M. Cordeira, and M. D. Dettinger, 2013: The landfall and inland penetration of a flood-producing atmospheric river in Arizona. Part 1: Observed synoptic-scale, orographic, and hydrometeorological characteristics, *J. Hydromet.*, **14**, 460–464.

Newell, R. E., N. E. Newell, Y. Zhu, and C. Scott, 1992: Tropospheric rivers?—A pilot study. *Geophys. Res. Lett.,* **19,** 2401–2404.

Newell, R. E., and Y. Zhu, 1994: Tropospheric rivers: A one-year record and a possible application to ice core data. *Geophys. Res. Lett.,* **21,** 113–116.

NOAA/NWS Earth Systems Research Laboratory, Physical Sciences Division, cited 2013: Atmospheric River Information Page.
[Available online at http://www.esrl.noaa.gov/psd/atmrivers/]

NOAA/NWS. 1989. *National Weather Service Observing Handbook No. 2: Cooperative Station Observations*. National Oceanic and Atmospheric Administration (NOAA): Silver Spring, MD.

Pfahl, S., and H. Wernli, 2012: Quantifying the relevance of cyclones for precipitation extremes. *J. Climate*, **25**, 6770–6780.

Ralph, F. M., P. J. Neiman, D. E. Kingsmill, P. O. G. Persson, A. B. White, E. T. Strem, E. D. Andrews, and R. C. Antweiler, 2003: The impact of a prominent rain shadow on flooding in California's Santa Cruz mountains: A CALJET case study and sensitivity to the ENSO cycle. *J. Hydrometeor.*, **4**, 1243–1264.

Ralph, F. M., P. J. Neiman, and G. A. Wick, 2004: Satellite and CALJET aircraft observations of atmospheric rivers over the eastern north Pacific Ocean during the winter of 1997/98, *Mon. Wea. Rev.*, **132,** 1721–1745.

Ralph, F. M., P. J. Neiman, G. A. Wick, S. I. Gutman, M. D. Dettinger, D. R. Cayan, and A. B. White, 2006: Flooding on California's Russian River: Role of atmospheric rivers. *Geophys. Res. Lett.,* **33,** doi:10.1029/2006GL026689.

Ralph, F. M., E. Sukovich, D. Reynolds, M. Dettinger, S. Weagle, W. Clark, and P. J. Neiman, 2010: Assessment of extreme quantitative precipitation forecasts and development of regional extreme event thresholds using data from HMT-2006 and

COOP observers. *J. Hydrometeor*, **11**, 1286–1304. doi: 10.1175/2010JHM1232.1

Ralph, F. M., P. J. Neiman, G. N. Kiladis, K. Weickmann, and D. W. Reynolds, 2011: A multiscale observational case study of a Pacific atmospheric river exhibiting tropical–extratropical connections and a mesoscale frontal wave. *Mon. Wea. Rev.*, **139**, 1169–1189.

Ralph, F. M., T. Coleman, P. J. Neiman, R. J. Zamora, and M. D. Dettinger, 2013a: Observed impacts of duration and seasonality of atmospheric-river landfalls on soil moisture and runoff in coastal northern California. *J. Hydromet.*, **14**, 443–459.

Ralph, F. M., and coauthors, 2013b: The emergence of weather-focused testbeds linking research and forecasting operations. *Bull. Amer. Meteor. Soc.*, **94**, 1187–1211.

Rasmussen, R., C. Liu, I. Ikeda, D. Gochis, D. Yates, F. Chen, M. Tewari, M. Barlage, J. Dudhia, W. Yu, K. Miller, K. Arsenault, V. Grubišić, G. Thompson, and E. Gutmann, 2011: High-resolution coupled climate runoff simulations of seasonal snowfall over Colorado: A process study of current and warmer climate. *J.Clim.*, **24,** 3015–3048.

Reeves, H. D., Y.-L. Lin, and R. Rotunno, 2008: Dynamic forcing and mesoscale variability of heavy precipitation events over the Sierra Nevada Mountains. *Mon. Wea. Rev.*, **136**, 62–77.

Riddle, E. E., A. H. Butler, J. C. Furtado, J. L. Cohen, and A. Kumar, 2013: CFSv2 ensemble prediction of the wintertime Arctic Oscillation. *Clim. Dynam.*, **41**, 1099–1116.

Rigby, J. G., 1998: The 1997 New Year's floods in western Nevada, special publication 23, Nevada Bureau of Mines and Geology, University of Nevada, Reno, NV, 111 pp.

Rutz, J. J., and W. J. Steenburgh, 2012: Quantifying the role of atmospheric rivers in the interior western United States. *Atmos. Sci. Lett.*, **13,** 257–261.

Rutz, J. J., W. J. Steenburgh, and F. M. Ralph, 2014: Climatological characteristics of atmospheric rivers and their inland penetration over the western United States. *Mon. Wea. Rev.*, in press.

Seager, R., N. Naik, and G. A. Vecchi, 2010: Thermodynamic and Dynamic Mechanisms for Large-Scale Changes in the Hydrological Cycle in Response to Global Warming*. *J. Climate*, **23**, 4651–4668.

Serreze, M. C., M. P. Clark, R. L. Armstrong, D. A. McGinnis, and R. S. Pulwarty, 1999: Characteristics of the western United States snowpack telemetry (SNOTEL) data. *Water Resources Research,* **35(7),** 2145–2160.

Serreze, M. C., M. P. Clark, and A. Frei, 2001: Characteristics of large snowfall events in

the montane western United States as examined using snowpack telemetry (SNOTEL) data, *Water Resour. Res.*, 37(3), 675–688, doi: 10.1029/2000WR900307.

Simmons, A., S. Uppala, D. Dee, and S. Kobayashi, 2007: ERA-Interim: New ECMWF reanalysis products from 1989 onwards. *ECMWF Newsletter,* **110,** 25–35.

Smith, B. L., S. E. Yuter, P. J. Neiman, and D. E. Kingsmill, 2010: Water vapor fluxes and orographic precipitation over northern California associated with a landfalling atmospheric river. *Mon. Wea. Rev.*, **138**, 74–100.

Smith, D., and coauthors, 2013: Seasonal to decadal prediction of the Arctic Oscillation. *ECMWF-WWRP/THORPEX Workshop on polar prediction, June 24–27, 2013.* [Available online at http://www.ecmwf.int/newsevents/meetings/workshops/2013/Polar_prediction/Presentations/Smith_Doug.pdf].

Smith, R. B., Q. Jiang, M. G. Fearon, P. Tabary, M. Dorninger, J. D. Doyle, and R. Benoit, 2003: Orographic precipitation and air mass transformation: An Alpine example. *Quart. J. Roy. Met. Soc.,* **129,** 433–454.

Smith, R. B., I. Barstad, and L. Bonneau, 2005: Orographic precipitation and Oregon's climate transition. *J. Atmos. Sci.*, **62**, 177–191.

Sodemann, H., and A. Stohl, 2013: Moisture origin and meridional transport in atmospheric rivers and their association with multiple cyclones. *Mon. Wea. Rev.*, **141**, 2850–2868.

Stohl, A., and P. James, 2004: A Lagrangian analysis of the atmospheric branch of the global water cycle. Part I: method description, validation, and demonstration for the August 2002 flooding in central Europe. *J. Hydrometeor*, **5**, 656–678.

Stohl, A., C. Forster, and H. Sodemann, 2008: Remote sources of water vapor forming precipitation on the Norwegian west coast at 60°N - a tale of hurricanes and an atmospheric river, *J. Geophys. Res.*, **113**, D05102.

Tang, Y., H. Lin, J. Derome, and M. K. Tippett, 2007: A predictability measure applied to seasonal predictions of the Arctic Oscillation. *J. Climate*, **20**, 4733–4750.

Uppala, S., D. Dee, S. Kobayashi, P. Berrisford, and A. Simmons, 2008: Towards a climate data assimilation system: Status update of ERA-Interim, *ECMWF Newsletter,* **115,** 12–18. [Available at http://www.ecmwf.int/publications/newsletters/pdf/115.pdf.]

USDA-NRCS, cited 2012a: SNOTEL and Snow Survey & Water Supply Forecasting. [Available at http://www.wcc.nrcs.usda.gov/snotel/SNOTEL-brochure.pdf.]

USDA-NRCS, cited 2012b: SNOTEL Data Collection Network Fact Sheet. [Available at http://www.wcc.nrcs.usda.gov/factpub/sntlfct1.html.]

U.S. Department of the Interior, cited 2012: Flood of January 1997 in the Truckee River Basin, Western Nevada. [Available at http://pubs.usgs.gov/fs/1997/0123/report.pdf.]

Viale, M. and M. N. Nuñez, 2011: Climatology of winter orographic precipitation over the subtropical central Andes and associated synoptic and regional characteristics. *J. Hydromet.,* **12,** 481–507.

Warner, M. D., C. F. Mass, E. P. Salathé, 2012: Wintertime extreme precipitation events along the Pacific Northwest coast: climatology and synoptic evolution. *Mon. Wea. Rev.*, **140**, 2021–2043.

Wick, G. A., P. J. Neiman, and F. M. Ralph, 2013: Description and validation of an automated objective technique for identification and characterization of the integrated water vapor signature of atmospheric rivers. *IEEE Transactions on Geoscience and Remote Sensing,* **51(4),** 2166–2176.

Wick, G. A., P. J. Neiman, F. M. Ralph, and T. M. Hamill, 2013: Evaluation of forecasts of the water vapor signature of atmospheric rivers in operational numerical weather prediction models. *Wea. Forecasting*, **28**, 1337–1352.

Zhu, Y. and R. E. Newell, 1998: A proposed algorithm for moisture fluxes from atmospheric rivers, *Mon. Wea. Rev.,* **126 (3),** 725–735.